OPTOFLUIDIC TUNABLE LENSES FOR IN-PLANE LIGHT MANIPULATION

CHEN QINGMING

PhD

The Hong Kong Polytechnic University

2018

The Hong Kong Polytechnic University

Department of Applied Physics

OPTOFLUIDIC TUNABLE LENSES FOR IN-PLANE LIGHT MANIPULATION

CHEN QINGMING

A thesis submitted in partial fulfillment of the requirements for the degree of Doctor of Philosophy

September 2017

Certificate of Originality

I hereby declare that this thesis is my own work and that, to the best of my knowledge and belief, it reproduces no material previously published or written, nor material that has been accepted for the award of any other degree or diploma, except where due acknowledgement has been made in the text.

_____ (Signed)

CHEN Qingming

_____ (Name of the student)

Abstract

Optofluidics seamlessly integrates optics and microfluidics in a single chip to make full use of the advantages of both. This doctoral study focuses on developing optofluidic lenses for in-plane focusing and diverging of light and presents three new designs of tunable liquid lenses: the laser-induced thermal gradient lenses, the dielectrophoresis (DEP) actuated lenses using single liquid-air interface, and the DEP-actuated lens using two liquid-air interfaces.

The first design is a tunable lens using laser-induced thermal gradient effect. Two metal strips are used to absorb the pump laser and to heat up the flowing solution, creating a 2D refractive index (RI) gradient for beam reshaping. Raytracing simulation and experiments are conducted to demonstrate the continuous tuning of focal length from initially infinite to the minimum 1.3 mm, as well as the off-axis focusing by offsetting the pump laser spot. Compared with previous designs, this thermal lens enjoys unique merits such as fast response (200 ms), using only one liquid, remote control, freely relocation of the lens, etc.

In the second design, the DEP effect is used to deform one liquid-air interface that is sandwiched between two parallel plates. The initially concave liquid-air interface can be continuously deformed into a convex one, tuning the lens from the divergent state (f = -1 mm) to the convergent state (f = +1 mm). Due to the capacitor-type driving, it consumes only 81 nJ per switching circle. In addition, the longitudinal spherical aberration (LSA) is effectively suppressed using the edge pinning effect.

The third design is an in-plane tunable lens using two DEP-actuated liquid-

air interfaces. By increasing the applied voltage, the focal length can be tuned from -0.5 mm (0 V) to infinite (175 V) and then to +0.5 mm (250 V). It achieves an *f* number of 0.91 while consumes only 6.7 nJ per switching circle. In the last two DEP-actuated lenses, large RI difference at liquid-air interface results in small focal length, and the uses of static flow (do not require continuous liquid supply) and electrical actuation make them easy to operate and simple to integrate with other lab-on-a-chip devices/systems.

In summary, three new designs of optofluidic tunable lenses have been presented for in-plane manipulation of light. Theoretical simulations and experiments have been conducted to examine the performance of the optofluidic devices. The thermal lens is new in term of working principle and facilitates the noncontact tuning of focusing state, while the DEP liquid lenses enable continuous tuning from sharp divergence to tight focusing without the requirement of continuous flow. As compared to the reported hydrodynamic-pressure or diffusion based liquid lenses that require continuous supply of two or more types of liquids and are tuned by adjusting the flow rates, our three types of lenses are unique and superior since they all allow the use of a single type of liquid and the two DEP-actuated lenses work at static flow and can be easily tuned by electrical voltage. These optofluidic lenses may find potential applications in lab-on-a-chip systems that require the functions such as optical switching, particle trapping, beam reshaping, optical in/out coupling, and so on.

List of Publications

Journal papers

[1] **Qingming Chen**, Aoqun Jian, Zhaohui Li* and Xuming Zhang*, Optofluidic tunable lenses using laser-induced thermal gradient, *Lab on a Chip*, vol. 16, no. 1, pp. 104-111, 07 Jan 2016. (Inside back cover). DOI: 10.1039/C5LC01163A

[2] **Qingming Chen**, Tenghao Li, Zhaohui Li, Z., Jinlin Long and Xuming Zhang*, Optofluidic Tunable Lenses for In-Plane Light Manipulation, *Micromachines*, vol. 9, no. 3, 26 Feb 2018. DOI: 10.3390/mi9030097

[3] **Qingming Chen**, Tenghao Li, Yujiao Zhu, Weixing Yu, and Xuming Zhang*, Dielectrophoresis-actuated in-plane optofluidic lens with tunability of focal length from negative to positive, *Optics Express*, Vol. 26, no. 6, pp. 6532-6541, 19 Mar 2018. DOI: org/10.1364/OE.26.006532

[4] **Qingming Chen**, Tenghao Li and Xuming Zhang*, Electrically reconfigurable in-plane optofluidic lens with tunability from biconcave to biconvex, (to be submitted)

[5] Yuan Bao, Xin Wen Yi, Zhaohui Li*, **Qingming Chen**, Jianping Li, Xudong Fan and Xuming Zhang*, A digitally generated ultrafine optical frequency comb for spectral measurements with 0.01-pm resolution and 0.7-μs response time, *Light: Science& Applications*, vol. 4, paper no. e300, 19 Jun 2015. DOI:10.1038/lsa.2015.73

[6] Tenghao Li, **Qingming Chen**, Yunfeng Xiao and Xuming Zhang*, Variable

optical delay line using discrete harmonic oscillation in waveguide lattices, *Journal of Lightwave Technology*, vol. 33, no. 24, pp. 5095 – 5102, 15 Dec 2015. DOI: 10.1109/JLT.2015.2480542

[7] Tenghao Li, **Qingming Chen**, Weixing Yu, Xuming Zhang*, Planar polarization-routing optical cross-connects using nematic liquid crystal waveguides, *Optics Express*, Vol. 26, no. 1, pp. 402-418, 18 Jan 2018, DOI: org/10.1364/OE.26.000402

[8] Tenghao Li, **Qingming Chen**, and Xuming Zhang*, "Planar optical cross-connect switch based on porlarization-dependent routing in nematic liquid crystal core waveguides," (submitted).

Conference papers

[1] **Qingming Chen** and Xuming Zhang*, Optofluidic tunable lens using laser-induced thermal gradient, The 4th International Conference on Optofluidics (Optofluidics 2014), paper P07, 28 – 30 August 2014, Guangzhou, China.

[2] **Qingming Chen** and Xuming Zhang*, Optofluidic tunable lens using laser-induced thermal gradient, Conference on Lasers and Electro-Optics (CLEO2016), 7 – 9 Jun 2016, San Jose, CA, USA.

[3] **Qingming Chen** and Xuming Zhang*, Optofluidic tunable lens using laser-induced thermal gradient, The 8th International Symposium on Microchemistry and Microsystems (ISMM2016), 30 May –1 June 2016, Hong Kong.

[4] Tenghao Li, **Qingming Chen** and Xuming Zhang*, Tunable optical delay line

using quadratic-coupled waveguide lattices, International Conference on Optical MEMS and Nanophotonics (OMN2016), paper Po2.3, 31 Jul – 04 Aug 2016, Singapore.

Patents

[1] Xuming Zhang, Tenghao Li, and Qingming Chen, An optical switch and optical cross-connect device, China Patents for Utility Models, Patent No. 201721204407.1, 23 February 2018. (张需明, 李腾浩, 陈庆明, 一种光开关及光交叉互连器件, 中国实用新型专利, 专利号 201721204407.1, 授权时间 2018/02/23)

[2] Xuming Zhang, Tenghao Li, and Qingming Chen, An optical cross-connect device based on liquid crystal electro-optic waveguide, China Patents of Invention, Application No. 201710855251.1, filed on 20 September 2017. (张需明, 李腾浩, 陈庆明, 一种基于液晶电光波导的光学交叉互连器件, 中国发明专利, 申请号 201710855251.1, 申请时间 2017 年 9 月 20 日.)

Acknowledgements

Here I would like to express my gratitude to many people who have provided support and assistance during my doctoral research.

Firstly, I would like to express my sincerest appreciation to my chief supervisor **Dr. Xuming Zhang** and **Prof. Zhaohui Li (**from Sun Yat-sen University) for their help and constant guidance in the last three years. Their advice and encouragement help me improve myself in many aspects of my daily work and will benefit me in my whole life.

I would also want to thank all the past and current group members for their great help and friendship, including Prof. Zhiqing Feng, Dr. Aoqun Jian, Prof. Ning Wang, Ms. Yuki Lam, Dr. Youling Chen, Dr. Furui Tan, Dr. Xiaowen Huang, Dr. Yang Liu, Dr. Tenghao Li, Ms. Yujiao Zhu, Dr. Yan Zhang, Mr. ChiChung Tsoi and Steven. Special thanks to my friends Dr. Gongxun Bai, Dr. Shenghuang Lin, Dr. Yongliang Zhang, Dr. Yanyong Li, Dr. Hui Long and Dr. Huiyu Yuan, etc.

Finally, I would like to express great gratitude to my family. I want to thank my parents for supporting me in my life and work. And thank my wife and my son for encouraging me when I was in a loss. It is they who make me proud of being a husband and a father.

Table of Contents

List of Figures

List of Tables

Chapter 1 Introduction

1.1 Background

In the last decades, miniaturization and integration of system in a single chip has been a permanent goal for research and industries. The breakthroughs in a number of disciplines, such as nanotechnologies, material science and advanced instruments, turn this goal into realization. The emergence of the microelectromechanical systems (MEMS) is a good example [1]. MEMS incorporates micro actuators, microsensors and microelectronics into a microchip, which includes electrical and mechanical elements. Numerous applicable microsensors have been demonstrated, including chemical sensors [2], temperature sensors [3], pressure sensors [4], magnetic fields sensors [5], inertial forces sensors [6], etc. Remarkably, most of these microsensors have better performance than their macroscale counterparts. For example, a micro pressure sensor, easily outperforms a pressure sensor made of the most precise macroscale level machining techniques in many aspects, such as dimensions, response speed, etc. Except from the great performance, high integration is another intrinsic merit of MEMS. By using the micro fabrication and packing techniques from integrated electronics, low cost and highly scalable systems can be achieved. Several micro actuators have also been demonstrated for optical switches. For instance, many mechanically actuated micro mirrors are fabricated in a small chip to redirect the beam [7]. In addition, there are some MEMS devices have been commercialized.

Microfluidics is a new type of micro system rooted from MEMS. It combines engineering, materials, physics, chemistry and biochemistry in a microchip using

micro and nano techniques [8]. As its name indicates, it deals with the behavior, the precise control and the manipulation of liquids in micro scale to achieve certain specific functions. Some other related techniques have also been developed along with microfluidics, such as polymer science, micro/nano fabrication, on-chip sensing and biological analysis, material synthesis and optofluidics. For example, soft lithography and polydimethylsiloxane (PDMS) play important roles in the development of microfluidics. Soft lithography is a technique for replicating micro structures using conformable photomask or molds. It provides an easy and low-cost way to fabricate micro devices. And PDMS is a widely used silicon-based organic polymer, which is particularly known for its unusual rheological (or flow) properties. Its unique properties make it the most common material in microfluidics. For instance, it is optically transparent, chemical inert, non-toxic, non-flammable , insulating, flexible and bio-compatible. Most importantly, it is easy to be molded into different structures by thermal curing.

Most of the microfluidic devices can be fabricated using the above techniques. By incorporating multi-functional elements into a small chip, microfluidics has many traits. It reduces the sample volume dramatically and enhances the manipulation precision at the same time. It is portable, economic, safe, easy fabrication and multi-functional. Many operations can be executed at the same time, shortening the time of experiment and providing better performance. It has the capacity to both process and analyze samples with minor sample handling. Thanks to the high integration, many functions like mixing, separation, reactions, sensing and analysis can be finished in a small chip [9]. It is also possible to achieve automation by incorporating actuators to control the fluid behavior. So

that multi-step reactions can be actuated by an inexperienced user.

As a sub-area of microfluidics, optofluidics is a relatively new technology that seamlessly integrates optics and microfluidics in a single chip to make full use of the advantages of both, creating a novel field for scientific research and industrial applications [10]. Benefiting from the unique properties of fluids, the optofluidics enables many novel functions, which have been regarded as impossible in solids. The merits include: (1) the ability to modulate the optical property of the fluid by simply replacing one with another; (2) optically smooth interface between two immiscible fluids; (3) the wide tunability of refractive index (RI) (usually the variation can be over 0.1, which is impossible in other methods) by diffusion between miscible fluids. Currently, most of the optical systems are made of solid materials, such as metals, glasses and semiconductors. In conventional optical devices, it is difficult to change the optical properties once it is manufactured. And modulations are usually achieved by mechanical movement (for solid lenses), which is complexed and poorly compatible. Replacing them with fluids has many advantages. For instance, different functions can be incorporated into a small chip; the cost is very low as no expensive materials are used and optical modulation can be achieved easily via the manipulation of fluids.

Portable and multi-functional chips have resulted in many practical applications. For example, reconfigurable electro-wetting lens has been used to replace the solid lens in some imaging systems, optofluidic display has found wide use in electronic books and optofluidic optical sensors have been applied for biomedical diagnosis. Two prominent advantages of optofluidics are integration and reconfigurability. Different functional components can be incorporated in a

single chip, such as light sources [11], optical waveguides [12], lenses [13] and sensors [14]. .

As the most important optical element, optical lens has also been demonstrated by optofluidics. By tuning the fluidic interfaces (by hydrodynamic flow or electrowetting etc.) or changing the RI (via solution diffusion or thermal gradient) of liquid, numerous optofluidic lenses have been demonstrated. The out-of-plane liquid lens (which manipulates the beam perpendicular to the substrate) has been used to replace the conventional solid lens in the imaging system, where the tunable focal length is preferred. While the in-plane (the light propagates in the liquid layer) lens is utilized to manipulate the light in a microfluidic network, improving the compatibility and scalability.

Although a number of optofluidic actuated methods have been demonstrated over the years, more practical designs are still in need. Most of the previous reported in-plane liquid lenses are sustained by continuous streams, which limits the compatibility with other microfluidic networks. In addition, the power dissipation should be taken into account while constructing a microfluidic network.

1.2 Objectives of research

The general goal of this thesis is to exploit new actuation methods and novel designs for optofluidic integration, especially for light focusing and diverging in a microfluidic chip. Gradient RI and step RI lenses will be exploited for in-plane light manipulation. More specifically, three major objectives will be pursued.

(1) New designs of in-plane tunable lens. A CW laser is used to illuminate the metal patterns to heat up the flowing solution, creating a 2D RI profile for beam

shaping. In the step RI lenses, dielectrophoresis (DEP) is utilized to manipulate the in-plane liquid-air interface, where the DEP drives the liquid into the air, resulting in a tunable liquid-air interface.

(2) Theoretical analysis is used to predict the performance of the designs. The 2D RI profile induced by thermal gradient is simulated by computed fluidic dynamic. And the DEP-actuated liquid-air interface is calculated by Laplace law. In addition, the lensing effect of the lenses is analyzed by raytracing simulation.

(3) Experiments are conducted to demonstrate the performance of the lenses. The experimental analysis includes focal length tunability, spherical aberration and response speed, etc.

1.3 Outline of thesis

Chapter 1 introduces the background of the microfluidics and optofluidics. The motivations and objectives of this doctoral research are also included in chapter 1.

Chapter 2 is the literature review, which describes the developments of optofluidics and reviews the optofluidic lenses. The optofluidic lenses are categorized as: out-of-plane and in-plane lenses. For comparison, these two types of the liquid lenses are discussed by their working principles and applications. However, it focuses more on the in-plane liquid lenses for light manipulation and applications in microfluidic networks. So as to build up the technical bases for this doctoral research.

Chapter 3 describes the device fabrication techniques used in this doctoral project, covering two types of microfabrication methods: lift-off technique and capillary flow assisted microchip bonding method.

Chapter 4 presents the first work: a new design of optofluidic tunable lenses using laser-induced thermal gradient. At first, computed fluidic dynamic (CFD) simulation and raytracing are conducted to theoretically analyze the performance of the design. Then a microfluidic chip is fabricated to experimentally demonstrate the tunable optofluidic thermal lens. A comparison between the simulated and experimental results reveals that they well match each other. Empirical formulas are deduced to describe the dependences of focal length on the pump laser power intensity and the flow velocity, respectively.

Chapter 5 reports the design of dielectrophoresis (DEP) actuated in-plane liquid lens using single liquid-air interface. By using the DEP force to deform the liquid-air interface, the lens can be tuned from divergence to convergence. Both simulated and experimental raytracing results demonstrate the great performance of the DEP liquid lens. The longitudinal spherical aberration of the DEP lens is also analyzed.

Chapter 6 presents another design of DEP-actuated liquid lens using two liquid-air interfaces. It is also tuned from biconcave to biconvex by the DEP force. A thick lens model is used to describe the optical properties of the lens. Since the liquid-air interface has a large RI difference, it has a short focal length. It has been demonstrated by the theoretical calculation and experiments.

Chapter 7 is the conclusion and future work. At first, a brief conclusion of this doctoral project is presented, including the merits and limitations of the optofluidic lenses developed in this thesis. Then, some suggestions of the future work are presented.

Chapter 2 Literature review

This work is reproduced in part from "Optofluidic Tunable Lenses for In-Plane Light Manipulation" Micromachines, 9(3), 97 (2018) by Q.M Chen, T.H Li, Z.H Li, J.L Long and X.M Zhang with the permission of Multidisciplinary Digital Publishing Institute (MDPI).

In this chapter, the evolution of optofluidics and the development of tunable liquid lenses will be reviewed. Firstly, some optofluidic components will be presented. Secondly, optofluidic lenses will be reviewed and discussed in terms of out-of-plane lenses and in-plane lenses. It focuses more on the in-plane lenses, which serves the technical basis for the study of this doctoral study. The last part is a discussion of the advantages and disadvantages of current tunable liquid lenses.

2.1 Optofluidics

Optofluidics is the fusion of microfluidics and optics [10]. It realizes optical functions through the manipulation of liquids in micro scale. By replacing solid material with liquid, some novel functions have been achieved. There are several potential applications for optofluidics, such as sensing [15], electronic paper display [16], adaptive liquid lens [13], particle manipulation [17], lab on a chip, etc. Reconfigurability is an important merit of optofluidics. The optical properties of the optofluidic elements can be tuned by the manipulation of liquid, thereby modulating their optical performance. Adaptive optics is a good example, which includes a variety of applications such as tunable lasers [11], optofluidic prisms [15], variable optical apertures [18], optical waveguides [12] and optofluidic lenses [13]. Integration is another merit of optofluidics. By using the soft photolithographic techniques, many optical elements can be fabricated in a small chip.

A variety of optofluidic sensors have been successfully demonstrated, providing a platform for various applications [20]. The integrated optofluidic system has greatly improved the detecting performance and has simplified the operation procedure, especially for biological and chemical analysis in small volume. Typically, there are three analytical mechanisms for optical sensing: refractive index (RI) sensing [21], fluorescence detection [22,23] and surface-enhanced Raman spectroscopy (SERS) detection [24]. .

Optofluidic trapping is also a powerful tool for particle manipulation in micro and nano scale. For example, Weihua Zhang et al. demonstrated the trapping and detecting of metal nanoparticle as small as 10 nm using plasmonic dipole antennas [25]. Mohammad Soltani et al demonstrated high throughput three-dimensional trapping with precise manipulation on a chip using a standing-wave interferometer [26]. As shown in Fig. 2.1, The evanescent field at the antinodes of the standing wave resulted from the interference of two waveguide outputs is exposed in the liquid for three-dimensional optical trapping. The trapping arrays can be precise relocated through the phase control of the propagating waves. Particle sorting is also demonstrated using a Mach–Zehnder interferometer (MZI) switch. They successfully demonstrated sorting and manipulation of individual DNA molecules with a repositioned speed of about 30 kHZ.

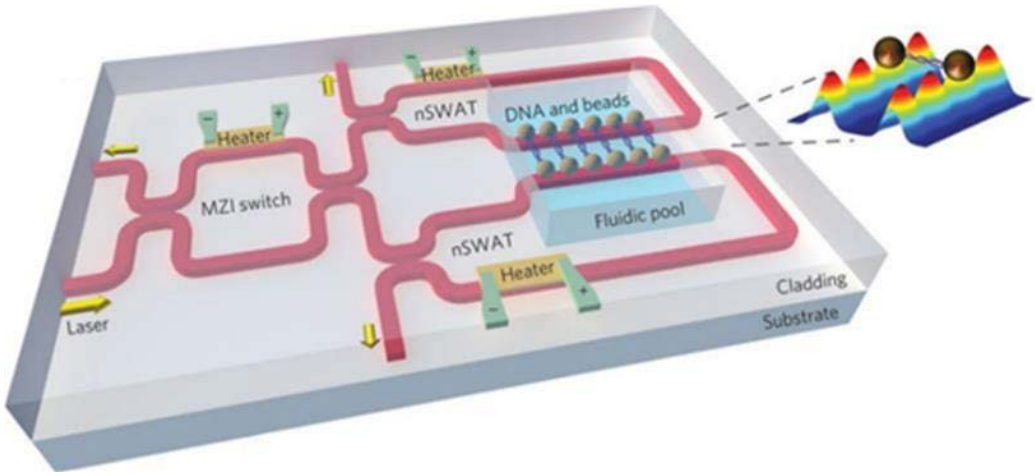

Fig. 2.1 Nanophotonic trapping for precise manipulation of biomolecular arrays. The nanophotonic standing-wave array was implemented with silicon waveguides on a silicon-on insulator (SOI) platform [26].

As a fundamental element in optics, optical lens has also been investigated intensively in optofluidics. More detail of the optofluidic lenses will be presented in the following part.

2.2 Optofluidic lenses

Optical lens is a crucial and fundamental element in optical systems. It is used to change the propagation of light and reshape the beam. The conventional optical lens is made of solid material, which has constant RI and fixed focal length. Therefore, the optical property is fixed after the manufacture. In the conventional optical systems, the modulation is achieved by mechanical movement, which is complicated and poorly compatible. Nowadays, the miniature systems have gradually replaced their macro counterparts in many fields and have better performance. For example, mobile phone has become a necessity in modern life. It is not only a phone for communication but also as a camera, in which micro lens is a key element. But the applications of such a solid lens is constrained by its intrinsic limitations, such as fixed focal length, poor tunability and low

compatibility. One solution to this problem is adaptive lens, in which the variable focal length can be achieved without complex actuation. Optofluidic lens has been investigated intensively in the last decade. Replacing the solid lens with liquid lens has many advantages, such as flexible tunability, good compatibility, small size and easy fabrication, etc. The unique properties of liquid make optofluidic lens a promising candidate for miniaturization and on-chip applications. The optical smoothness makes the fluidic interfaces suitable for optical lens. In addition, liquid can be adapted to any shape and configuration through microfluidic manipulations. For example, the liquid-liquid interface can be modified by numerous methods, such as electro-wetting [27], dielectrophoresis [28], pressure control [29], flow streams [30], etc. Another way to form a lens is to form a graded RI profile, which has been used for graded index fiber and gradient index lens (GRIN lens) in conventional optics. Unlike solid material, the RI of liquid can be modified through a variety of mechanisms. For instance, the RI of liquid depends on other physical parameters, such as temperature [19] and solution concentration [31]. Reconfigurability of the lens becomes an easy and effective way to manipulate the light by simple microfluidic modulation.

In term of the relationship between the microfluidic substrate and light propagation direction, the optofluidic lenses can be classified as: out-of-plane lens and in-plane lens [13]. Similar to the conventional lens, the out-of-plane lens manipulates beams in the direction perpendicular to the substrates. While the in-plane liquid lens deals with beams propagating within the liquid layer (on the substrate of the chip). The distinct characteristics make them suitable for different applications. The compatibility with the conventional system makes it possible for

the out-of-plane lenses to replace their solid counterparts. For example, some liquid lenses find applications in digital cameras or cell phones. Attaching an adaptive liquid lens to a microscope system would increase the depth of field. Electronically modulation of the liquid lens allows to refocus over a large range of distance. The ability to refocus quickly and precisely leads to many applications such as scanning, package sorting and security. There are also numerous commercialized out-of-plane liquid lenses available in the market. While the in-plane liquid lens can be incorporated into a microfluidic network. An integrated chip avoids the manual alignment in the conventional optical systems and makes it smaller and cheaper. In addition, we can not only use the fluidic manipulation to modulate the optofluidic lens but also in turn taking advantage of the adaptive lens for other microfluidic applications. For example, Yang's group demonstrated the optical trapping of single cell through an optofluidic lens based on the thermal convection [17].

Due to its wide applications, considerable attention has been dedicated to the optofluidic lenses. A number of reconfigurable lenses have been proposed and demonstrated in optofluidic platforms. The mechanisms for the out-of-plane and the in-plane lenses will be reviewed and discussed in the following section. In addition, some examples will be given to describe their working principles and potential applications.

2.3 Out-of-plane optofluidic tunable lenses

In the conventional lenses, the solid material is shaped and polished to form a specific curved interface, at which the rays bend suddenly because of RI difference

between air and the lens. Most of the out-of-plane lens designs follow the idea from solid lens. Usually, they have a circular chamber made of transparent materials. Therefore, they can replace the solid lens in conventional imaging system and provide flexible ways to realize reconfigurable focusing. The liquid-solid or liquid-liquid (air) interfaces can be formed and tuned by microfluidic techniques. For example, the shape of transparent elastic material polydimethysiloxane (PDMS) can be modified through pressure control [13]. In addition, the liquid-liquid interface can be tuned by a number of methods, such as electrowetting, dielectrophoresis, hydrodynamics or some other physical effects [13]. There are two common actuation methods for out-of-plane liquid lens: mechanical and electrical ones. A simple way to form a mechanically driven liquid lens is using an elastic transparent membrane, such as PDMS. The shape of the lens is controlled by driving liquid into the chamber using external pump. This mechanical method can be used for most of liquids regardless of their electrical properties. While the electrical actuation concerns about the permittivity or conductivity of the liquids. Electrowetting and dielectrophoresis (DEP) are the two most popular electrical actuations in liquid lens. The electrowetting effect is utilized to modify the contact angle between solid-electrolyte due to an electrical potential difference between the solid and the electrolyte. While the DEP drives the liquids with higher permittivity to stronger intensity filed. In this subsection, the driven mechanisms, designs and working performance of the out-of-plane lenses will be reviewed.

2.3.1 Mechanically actuated out-of-plane lenses

In a mechanically driven liquid lens, an elastic and transparent membrane is used

to predefine the shape of the lens. Then an external pump is applied to control the pressure inside the liquid container, thereby changing its geometry and focal length. There are two ways to modify the pressure inside the elastic chamber: controlling the volume of the liquid or squeezing the liquid inside the chamber.

The most straightforward way to change the shape of the elastic membrane is to modify the fluidic pressure by controlling the volume of the liquid. Agarwal et al. proposed a mechanical actuated liquid lens through the fluidic pressure applied by an external syringe pump [32]. They demonstrated both double convex (DCX) and double concave (DCV) lens using the same structure. And the tunable focal lengths of DCX and DCV are over the range of 75.9 to 3.1 mm and -75.9 to -3.3 mm, respectively. As shown in Fig. 2.2, the liquid lens consists of a silicon lens chamber and two PDMS membranes. The dimensions of the liquid lens system are 10 mm × 10 mm ×1.5 mm (L×W × H) with a diameter of 4 mm. A syringe pump is connected to the inlet of the lens chamber to precisely control the liquid volume. By pumping liquid (DI water) in or out of the lens structure, it can be tuned from the DCX state to the DCV state. The imaging characteristics of the adaptive liquid lens were analyzed for both the DCX and DCV states.

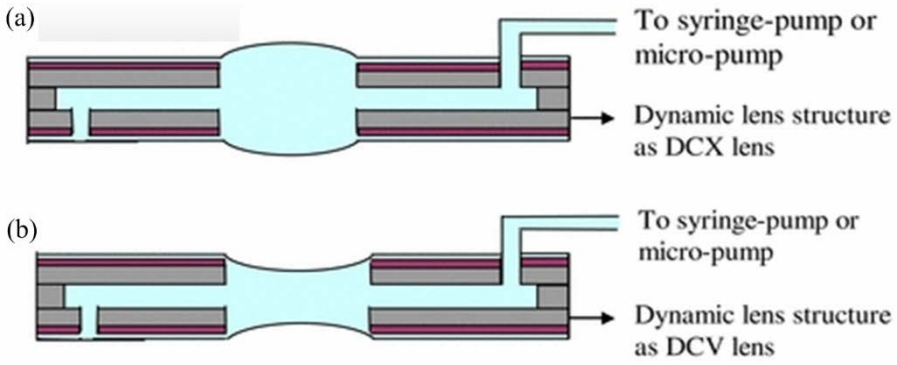

Fig. 2.2 Polymer-based variable focal lens microlens system [32], (a) Double convex (DCX) lens and (b) Double concave (DCV) lens.

Another way to mechanically actuate the out-of-plane liquid lens is to change the geometry of the lens by squeezing the liquid inside the chamber. Hongwen Ren et al. demonstrated such a liquid lens using a servo motor [33]. The schematic design of the liquid lens is shown in Fig. 2.3. It consists of an annual sealing ring, an elastic membrane (PDMS), a glass plate, an exterior rubber membrane and liquid with a fixed volume. Here a servo motor is attached to the exterior rubber membrane to deform its shape, thereby compressing the liquid in the reservoir. In the initial state, the transparent membrane is flat and has no focusing effect, see Fig. 2.3a. When the servo motor deforms the rubber membrane, the excess liquid in the reservoir pushs the lens membrane outward, resulting in a convex lens like Fig. 2.3b.

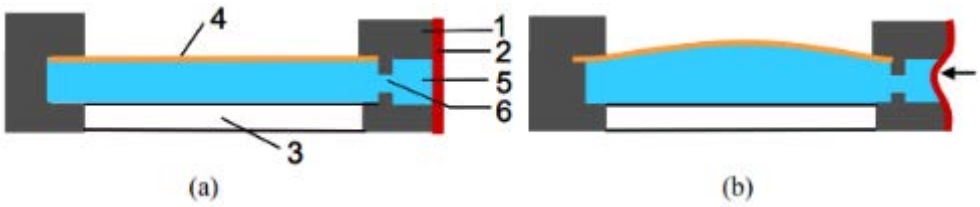

Fig. 2.3 Side view of the liquid lens cell [33]: (a) without and (b) with convex lens profile. 1-annular sealing ring, 2-rubber membrane, 3-glass plate, 4-elastic membrane, 5-liquid, and 6-a hole

The shapes of the above-mentioned lenses are modified by mechanical actuations, changing the liquid volume or squeezing the liquid. Continuously modulation of the lens has been successfully demonstrated. They can also be used for imaging in a conventional optical system with a CCD camera. But the requirement for external pump or electrical motor may limit their applications because of the complex setup and the large size.

2.3.2 Electrically actuated out-of-plane lenses

The modulation of the focal length without mechanical movement has significantly importance in some specific applications, such as mobile phones and digital camera. The electrical actuation can be a promising solution. It can be used to precisely manipulate the small volume of liquid in microscale without any moving part. The small size and stable operation regardless of gravitation and temperature perturbation make electrical actuated liquid lens more suitable for device packing and practical applications. For example, the liquid lens can be used to replace solid lens in a conventional camera. By doing so, the focal length of the imaging system can be tuned over a large range without mechanical movements. According to their working mechanisms, the electric actuations can be classified into two types: electrowetting lens and dielectrophoretic lens.

(1) Electrowetting out-of-plane liquid lens

Initially, the contact angle between a liquid and solid surface is determined by interfacial tension at the contact point. By changing the contact angle, one can modulate the curvature of the liquid droplet, resulting in tunable focal length. One option is electrowetting, where the interfacial tension is changed by applying an external electric field. S. Kuiper et al. proposed a variable-focus liquid lens for miniature cameras using electrowetting [27]. Fig. 2.4 depicts the cross section of the electrowetting liquid lens. Two immiscible liquids with different RIs are filled into a cylindrical container. If the densities of the two liquids are equal, the initial shape of the meniscus is a perfect sphere, which is insensitive to the perturbations and gravitation. To apply an electric field on the side, the cylindrical glass is coated with a transparent electrode (indium tin oxide: ITO), which is then covered by an

insulating film. When a voltage is applied between the conductive liquid and the side electrode, there will be an electric field across the insulating layer, see Fig. 2.4b. The reduction of the interfacial tension between the conductive fluid and the insulating layer leads to the change of the contact angle between them. The relationship between the contact angle and the applied voltage can be described by [27]:

$$\cos\theta = \frac{\gamma_{wi} - \gamma_{wc}}{\gamma_{ci}} + \frac{\varepsilon}{2\gamma_{ci} d_f} V^2 \tag{2.1}$$

where γ_{wi}, γ_{wc}, and γ_{ci} are the interfacial tensions of wall/insulating liquid, wall/conductive liquid and liquid/liquid, respectively. And ε is the dielectric constant of the insulating film, d_f is the thickness. V is the applied voltage. Fig. 2.4c shows fluidic interfaces under 0 V, 100 V and 120 V.

To demonstrate its imaging property, a miniature camera based on the above-mensioned electrowetting lens was developed, as shown in Fig. 2.5. The liquid lens is inserted into two plastic modeled lenses. Fig. 2.5d-e show the pictures taken using the liquid lens focused at 50 cm and 2 cm, respectively. For comparison, a similar image was also captured by a fixed-focus lens, see Fig. 2.5c. It is noticed that the camera maintains the good resolution with the liquid lens focusing at 50 cm and 2 cm. And no decrease in performance appeared after over one million switches and experiencing 10^3 times the Earth's gravitational constant. This kind of miniature liquid lens camera may find potential applications in some fields where size, scalability, power consumption and durability are critical.

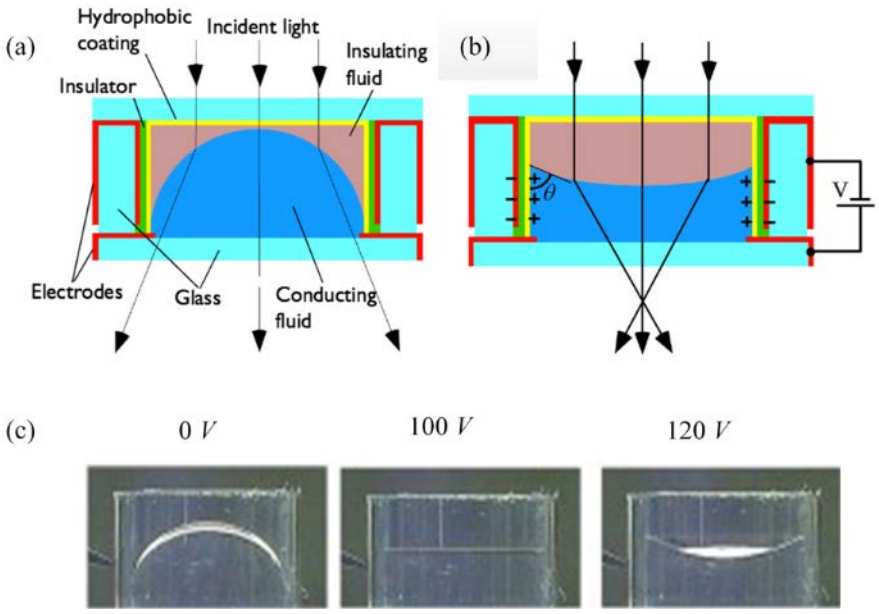

Fig. 2.4 Variable liquid lens actuated by electrowetting [27]. (a) Schematic cross section view. (b) When an external voltage is applied between the conductive liquid and the wall, an electric field is exerted on the insulating layer. The contact cangle θ changes according to the electrowetting effect. (c) Experimental results under 0 *V*, 100 *V* and 120 *V*, respectively.

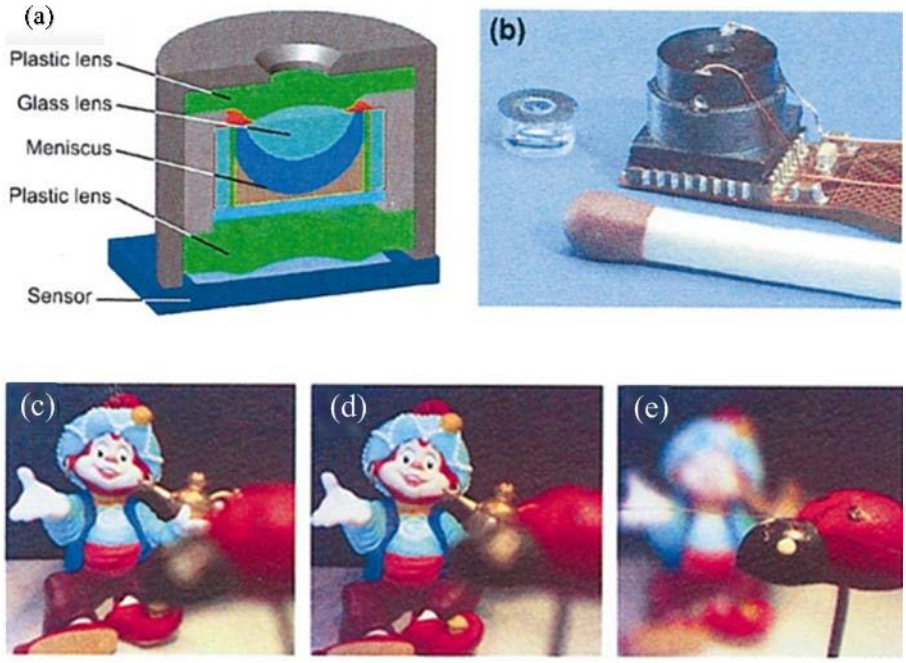

Fig. 2.5 Optical camera module and imaging performance [27]. (a) Optical camera using liquid lens. (b) Assemble camera module. (c) Image using a fixed-focus lens. (d) Image with liquid lens focused at 50 cm and (e) Image with liquid lens focused at 2 cm.

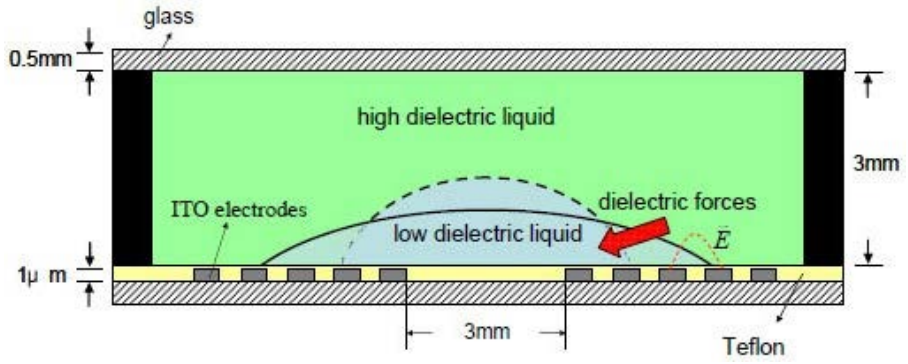

Fig. 2.6 Schematic of dielectric actuated liquid lens [34]. Under the DEP force, the liquid with higher permittivity shrinks and forces the droplet to a new curvature indicated by the dashed line.

(2) Dielectrophoresis-actuated out-of-plane liquid lens

The DEP is another way to modify the liquid/liquid interface in microscale. It has been explored for many microfluidic applications, such as particle manipulation, transportation, separation and sorting. Unlike the electrowetting, the DEP exerts a net force on the fluidic interface. Under the DEP force, the liquid with higher permittivity is drawn to intense electric field collectively. It can be used to deform the interface of liquids and to change the focal length in an adaptive liquid lens. Cheng et al demonstrated a dielectrically actuated liquid lens using the DEP [34]. Two immiscible liquids with equal density and different permittivities were filled into a PMMA (polymethyl methacrylate) container (Fig. 2.6). Specific concentric electrodes were coated on the bottom glass to apply an nonuniform electric filed on the liquids. As the voltage was turned on, the DEP force drove the liquid with higher permittivity to the strong electric field, thereby deforming the liquid interface and its focal length. While the applied voltage was varied from 0 V to 200 V, the focal length was changed from 34 mm to 12 mm. They also demonstrated the focal length tunability by using it to capture an object placed 50 mm away. Similar DEP driven liquid lenses have also been demonstrated using

liquid crystal [35].

2.3.3 Mechanical actuation versus electrical actuation

The above section has reviewed some out-of-plane liquid lenses and their applications for imaging. The mechanical methods can effectively deform the curvature of the lens and demonstrate good performance. But the requirements of external pump or motor limit its packing and scalability. In addition, lifetime of the device is also affected by the fatigue of the membrane. Compared to the mechanical ones, the electrical actuations have many advantages, such as smaller size, quiet, easy packing and better durability. Although the out-of-plane liquid lens has replaced solid lens in some applications, adaptive liquid lenses in some specific fields are still urgent. For instance, the out-of-plane lens can not be integrated into a microfluidic network, where high intensity elements are incorporated together to achieved multi-functional systems.

2.4 In-plane optofluidic tunable lenses

Different from the out-of-plane liquid lens, the in-plane one manipulates the light in the plane of the substrate, upon which the liquid sample is held. Benefiting from its compatibility, the in-plane optofluidic lens can be incorporated into a single chip without complicated manual alignment and promises high integration density. In term of the tunability, the in-plane liquid lenses can be either tuned by adjusting the fluidic interface using numerous microfluidic techniques, or by modulating the RI of the liquid using temperature, electric field and concentration. In this subsection, the in-plane liquid lenses will be reviewed in aspect of operation mechanisms and recent development. In addition, their applications in lab-on-a-

chip systems are also discussed.

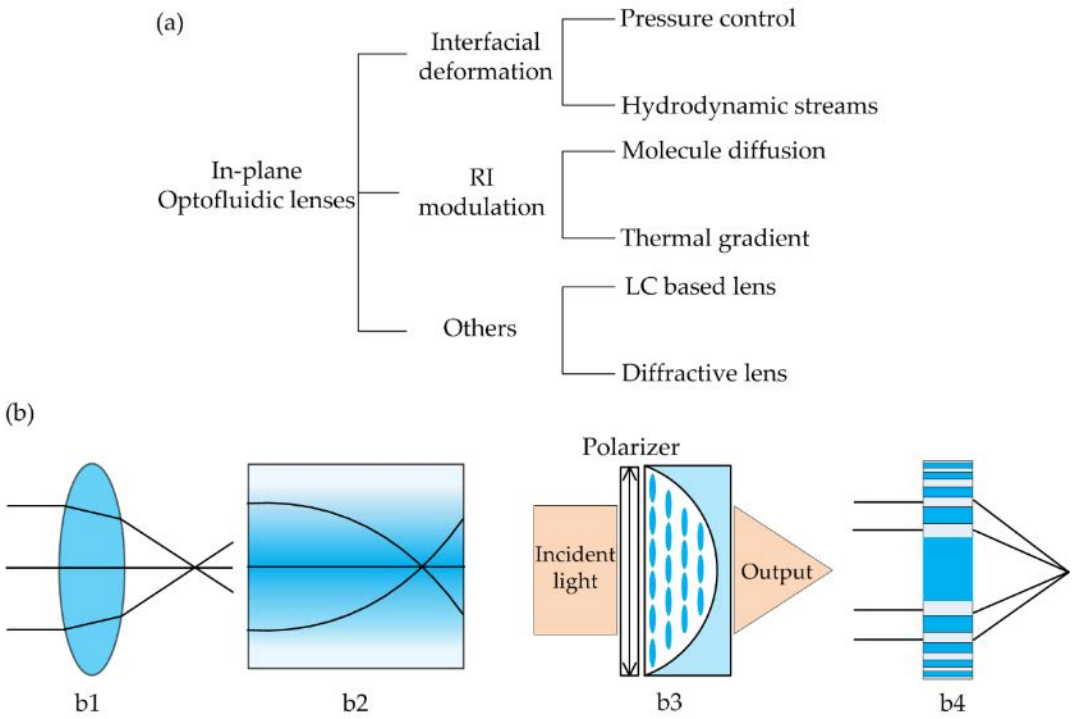

Fig. 2.7 In-plane optofluidic lenses categories and the working principles: (a) The in-plane liquid lenses are classified into three types of lenses according to their working principles; (b) Schematic diagrams of the in-plane liquid lens: b1 is the interfacial deformation lens; b2 is RI modulation (gradient index) lens; b3 is the liquid-crystal based lens (LC: the blue ellipses) and b4 is the diffractive lens (i.e., the Fresnel zone plate).

2.4.1 Classification of in-plane optofluidic lenses

Figure 2.7a summarizes the categories of the in-plane lenses and Fig. 2.7b explains the corresponding working principles. Most of the reported designs of in-plane optofluidic lenses can classified into two types: refractive lens and gradient index (GRIN) lens. The former often makes use of interfacial deformation and the latter of RI modulation. The rest of reported designs can be generally grouped into the others. In the refractive lens, the beam is refracted at the smooth fluidic interface of immiscible liquids (see Fig. 2.7(b1)). The focal length is usually tuned by changing the lens geometry. In a microfluidic chip, there are numerous ways to

modify the curvature of the fluidic interface, for example, pressure control [29], hydrodynamic modulation [30], electrowetting [27] and dielectrophoresis [36]. Among them, the pressure control and the hydrodynamic modulation are more popular in regulating in-plane lenses. In the GRIN lens, solution diffusion [31] or thermal diffusion [17] can be used to establish a RI gradient profile, in which the rays are bent gradually and then focused to a point (Fig. 2.7(b2)). A large RI gradient (usually over 0.1) is achievable in a microscale region, resulting in tight focusing and wide tunable range. The refractive lens and the GRIN lens are often independent of the polarization and the wavelength of the incident light due to the use of isotropic and low-dispersion liquids (e.g., water, ethanol, ethylene glycol). In addition, there are some other lenses that aim at polarization separation or wavelength selection, such as birefringent liquid lens [37] and diffractive optofluidic lens [38]. For example, liquid crystal (LC) has been used to construct a polarization-dependent liquid lens [37]. Fig. 2.7(b3) displays the schematic of the LC liquid lens, in which the LC molecules can be realigned by applying a sufficiently strong electrical field. As a result, incident beams of different polarization directions would experience different RIs and have different focal lengths. Another kind of lens is Fresnel zone plate (FZP), which is based on the diffraction rather than refraction. As shown in Fig. 2.7(b4), an optofluidic FZP can be achieved for light manipulation by filling liquid into the periodic microstructure. Different parts of the diffracted lights interference constructively with each other to form a focal point. The FZP depends on the incident wavelength, providing another freedom of tunability.

This subsection has five parts. The first gives an introduction of in-plane

optofluidic lenses. In the second, the in-plane optofluidic lenses will be discussed according to their operation mechanisms. Then, some applications of the in-plane liquid lenses will be presented in the third section. There is a brief discussion in section four. The last part is the summary.

In the following section, the in-plane optofluidic lenses will be reported based on their operation mechanisms. Firstly, some example of the refractive lenses based on the fluidic interfaces will be presented. Then the GRIN lenses are discussed. In addition, the in-plane liquid lenses based on other methods are also discussed at the end of this section.

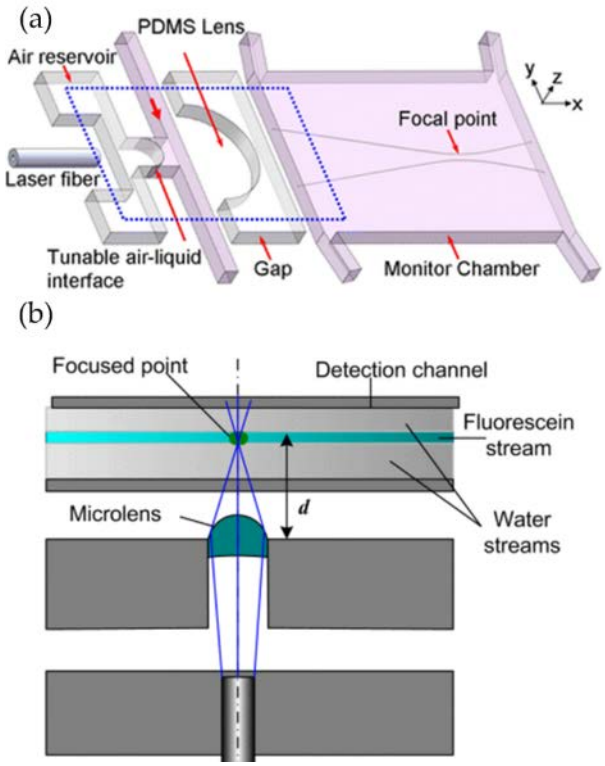

Fig. 2.8 Pressure-control liquid lenses: (a) Liquid-air interface tuned by flow rate control [29]; (b) Pneumatically droplet tunable lens [40].

2.4.2 Interface deformation lenses

The most straightforward method to construct an in-plane optofluidic tunable lens is to use the interfaces between immiscible streams (or liquid-air interface), where the interfacial curvature can be modified by numerous microfluidic techniques [29,30,39]. The general working principle is depicted in Fig. 2.7(b1). In the case of in-plane lens, the geometry modulation can be achieved either by the pressure control or by the hydrodynamic streams. In the pressure-control liquid lens, the curvature of the liquid-air interface is modified by external pumping [29,40]. Tony Huang's group proposed a reconfigurable in-plane liquid lens using fluidic pressure to tune the liquid/air interface in a microfluidic chip [29]. As shown in Fig. 2.8a, this microlens consists of a reconfigurable divergent liquid-air interface and a static polydimethylsiloxane (PDMS) lens. The liquid flows through a straight channel and traps the air in the chamber, forming a liquid-air interface. By adjusting the flow rate, it changes the pressure inside the channel as well as the interfacial radius. It demonstrated the continuous modulation of the focal length by tuning the flow velocity. Behind the lens, there is a chamber for experimental raytracing. Another pressure-controllable liquid-air in-plane lens is demonstrated by Dong et al. [40]. By precisely locating a liquid droplet at the T-shape junction, a tunable in-plane liquid lens is formed in the microchannel (see Fig. 2.8b). This microlens has a tunable focal length from a few hundreds of micrometers to infinite. It can be pneumatically repositioned and removed inside the predefined microchannel. The geometry of the chamber can also be used as a tunable lens by modifying the shape using the pressure control [41]. The pressure-control liquid-air interface is governed by the Laplace law:

$$\Delta P = 2\gamma\kappa = \gamma\left(\frac{1}{R_1}+\frac{1}{R_2}\right) \tag{2.2}$$

where γ is the surface tension coefficient between the liquid and air, κ is the mean curvature of the liquid-air interface. R_1 (in horizontal) and R_2 (in vertical) are the principal curvature radii of the interface. The ideal liquid-air interface is spherical in both horizontal and vertical directions. The external pump is used to balance at the pressure drop at the interface [29,40].

Another way to change the geometry of the in-plane liquid lens is to use the hydrodynamic modulation [39], in which the fluidic curve is formed and controlled by hydrodynamic force. In this case, two or more immiscible streams (the liquid core and the liquid cladding) are pumped into a specific microchannel to form reconfigurable interfaces. Tuning the ratio of the flow streams enables to continuously modulate the fluidic interfaces. It should be noted that the optical properties of the hydrodynamic stream liquid lens are dependent on the shape of the fluidic chamber. Seow et al. demonstrated a tunable liquid lens by injecting three flow streams into a rectangle-shaped expansion chamber [42], where the liquid with a higher RI acts as the core and the other two streams with a lower RI act as the cladding. Fig. 2.9 shows the schematic designs of the liquid lenses, V_{co} is the flow rate of the core, V_{cll} and V_{clr} are the flow rates of the left and right claddings, respectively. A biconvex lens is formed when $V_{co} > V_{clr} = V_{cll}$, see Fig. 2.9a. And the curvature radius becomes smaller with a higher cladding flow rate. By increasing the value of V_{clr}, the microlens becomes plano-convex (Fig. 2.9b) and then concave-convex (Fig. 2.9c), respectively. Both collimation and focusing have been demonstrated in this type of microlens by tuning the flow rates.

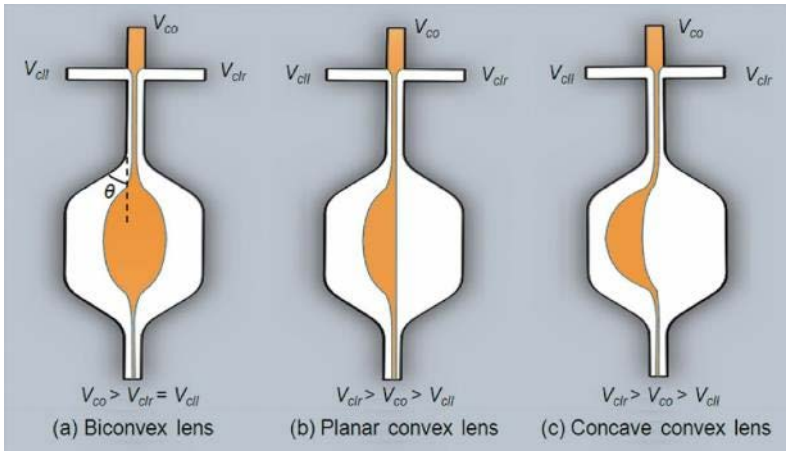

Fig. 2.9 Different curvatures of tunable liquid microlenses via the control of laminar flow rate [42]: (a) Biconvex lens; (b) Plano-convex lens; (c) Concave-convex lens.

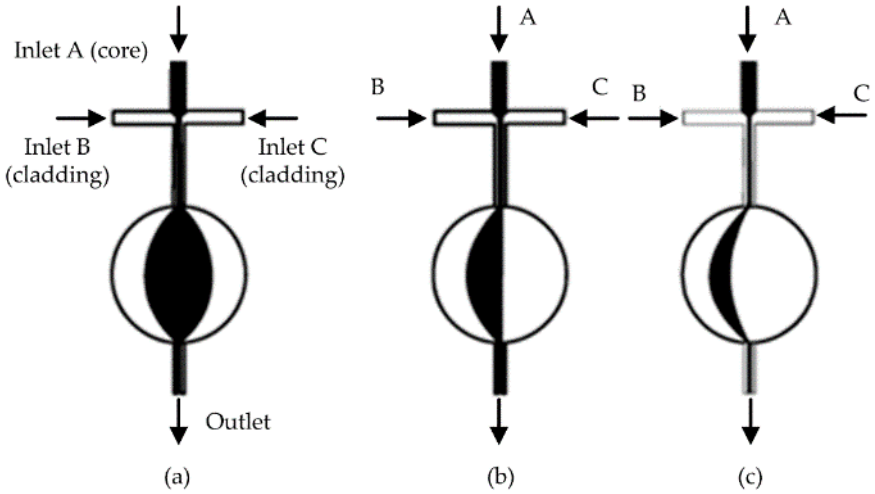

Fig. 2.10 Reconfigurable optofluidic lenses with a circular lens chamber [43]: the lens shape is modified by adjusting the flow rates of the core and cladding streams. (a) Biconvex lens; (b) Plano-convex lens; (c) Concave-convex lens.

Another design of liquid lens uses the circular chamber as shown in Fig. 2.10. Song et al. reported the modeling and experimental results of a tunable lens by injecting three laminar streams into a circular chamber [43]. The liquid-core liquid-cladding lens with perfect curvatures was formed by the circular design. Figure 4 describes the schematic design of the circular liquid lens. In the symmetric state, the lens has a biconvex shape as shown in Fig. 2.10a. By further increasing the flow rate of inlet C, it can tune the lens into the plano-convex shape

(Fig. 2.10b) and then the concave-convex shape (Fig. 2.10c). The curvature radius can be tuned from that of the chamber to infinity. As the width of the channel is much smaller than that of the expansion chamber, the model can be approximately described as a source-sink pair model [43]. A reconfigurable biconcave lens was demonstrated by Li et al. [44]. They used the combination of pressure driven flow and electro-osmosis to realize both focusing and diverging in a rectangle chip. Fang et al. proposed a hydrodynamically reconfigurable optofluidic lens, which can be tuned from biconcave to biconvex [39]. Fig. 2.11 depicts the operation principle of the liquid lens. The chamber with two convex ends is used to realize the modulation from biconcave to biconvex. Two immiscible liquids with different RIs are injected into the expansion chamber, where the liquid core (with higher RI) is sandwiched by the liquid claddings (with lower RI). The curvature of the interface is modified by tuning the flow ratio of the core and cladding streams. When the cladding flow is low, the liquid core expands outside into the cladding area, resulting in a biconvex lens (see Fig. 2.11a, b). By increasing the rate of the cladding flow, the curvature of the liquid lens decreases. With the further increase of the cladding flow, the liquid core is compressed into a biconcave shape and the lens becomes negative, as shown in Fig. 2.11c, d. The modulation from biconvex (positive) to biconcave (negative) lens has been demonstrated by adjusting the flow rate. They proposed a two-dimensional quadrupolar flow model to analyze the operation of the liquid lens [39]. As shown in Fig. 2.12, the model has two sources at the left side and two sinks at the right side. The sources and sinks were regarded as dimensionless points. By combining the flow model and the theory of thick lens together, an equation was derived to describe the focal length:

$$f = \frac{-n_1 r^2}{2(n_1 - n_0)\left[(n_1 - n_0)(s+b) - n_1 r\right]} \tag{2.3}$$

where n_0 and n_1 are the RIs of the liquid cladding and liquid core, respectively. And b is half of the distance between the two sources, r is the curvature radius of the liquid interface. The parameter s equals to d or -d when the interface is positive or negative, respectively. By using the combination of a tunable biconvex lens and a reconfigurable liquid prism. Chao et al. demonstrated the controlling of the focal length and the deviation angle of the beam [45].

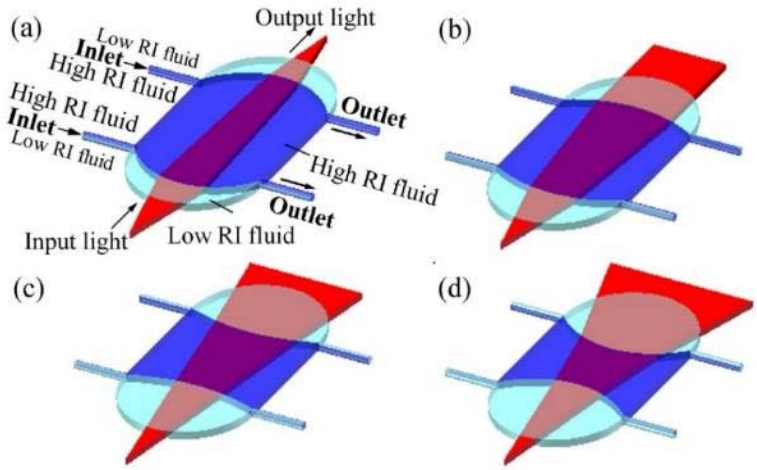

Fig. 2.11 Hydrodynamically reconfigurable optofluidic lens, in which the liquid core (in blue) is sandwiched by the liquid claddings [39]. (a) The liquids form a biconvex lens and the beam is focused. (b) The beam is collimated when the interface curvature becomes smaller. (c, d) A biconcave lens is obtained and the beam becomes divergent.

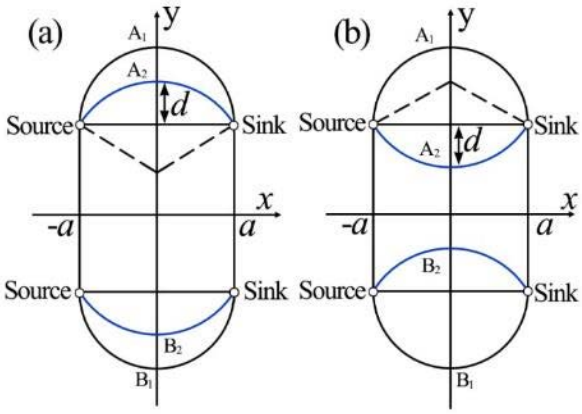

Fig. 2.12 The coordinate of microlens model [39].

2.4.3 Refractive index (RI) modulation lenses

As mentioned above, the RI modulation is another way to alter the optical properties of fluidic components. A simple method to change the RI of the liquid medium is to replace one with another. Seow et al. proposed a tunable planar optofluidic lens using a PDMS lens chamber [46]. By filling the chamber with the mixer of two miscible liquids, the RI was tuned from 1.33 to 1.63. The RI of medium is dependent on several physical properties such as concentration [47] and temperature [17]. It can be also changed by external electric field, acoustic field and mechanical strain. The optical propertis of the optofluidic device can be tuned through the modulation of the RI profile, which is also very popular in solid optics. For instance, in a graded index optical fiber, rays follow sinusoidal paths and cross each other periodically. Similarly, rays bend gradually and focus to a focal point, forming the GRIN lens. Compared with the solid materials, the RI modulation of liquid is much easier. By simply changing the concentration of the solutions, the RI change over 0.1 can be achieved [48]. A variety of optofluidic waveguides [49,50] and lenses [31,51] base on the diffusion of two miscible solutions have been demonstrated. Temperature gradient is another effective way to form a RI gradient in fluid [17].

A simple method to form a RI gradient within liquid medium is the solute diffusion. In a laminar flow inside the microchannel, the concentration gradient is determined by the solution diffusion [52], which can be modulated by the flow rate control. Therefore, a graded RI profile can be achieved using the solution diffusion. Yang et al. proposed an optofluidic RI gradient for lightwave bending and manipulation through the diffusion between ethylene glycol and deionized

water [12], in which the RI can be tuned from 1.34 to 1.42. Mao et al. demonstrated a reconfigurable liquid gradient index (L-GRIN) lens with two degrees of freedom using $CaCl_2$ solution as the core and deionized water as the cladding [31]. As shown Fig. 2.13A, the two liquids (the $CaCl_2$ solution and DI water) are injected into the microfluidic chip to establish the gradient profile by diffusion of laminar flows. The rays bend gradually when they meet the RI gradient. Tuning the flow rates of the liquids enables not only to change the focal length, but also to shift the focused beam away from the optical axis, providing another freedom for adaptive optics. Fig. 2.13B depicts the RI distribution along lines 1–5. The RI profile inside the channel follows a hyperbolic secant (HS) function as

$$n^2(x) = n_s^2 + \left(n_0^2 - n_s^2\right)\mathrm{sech}^2(\alpha x) \tag{2.4}$$

where $n(x)$ is the RI at the given position, n_0 is the RI at the center, n_s is the lowest RI in the liquid medium and α is the gradient parameter. Changing the flow rate enables the modulation of the RI profile as well as the focal length of the lens. Fig. 2.13C shows the RI along line 3 at different flow rates. The ray tracing simulated results in different flow conditions are shown in Fig. 2.13D. It can also shift the focus away from the center using an asymmetric RI profile.

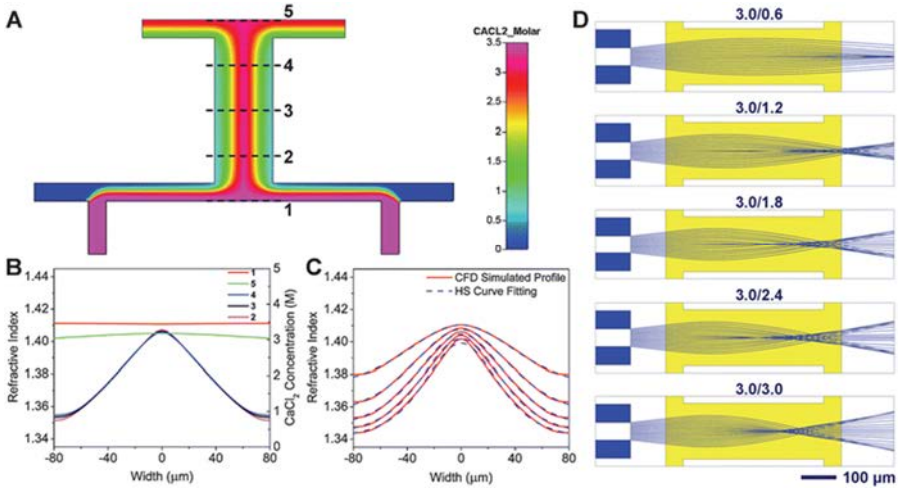

Fig. 2.13 L-GRTN lens with two degrees of freedom [31]. (A) Simulated refractive index profile and ray tracing. (B) Cross-sectional refractive index distribution at different locations along the flow direction (1, 2, 3, 4 and 5 as indicated in a). (C) Refractive index distribution along line 3 (defined in a) at different flow rates. (D) Ray tracing results in different flow conditions (3.0/0.6 represents $CaCl_2$ flow rates = 3.0 μL m^{-1} and H2O flow rate = 0.6 μL m^{-1}, respectively).

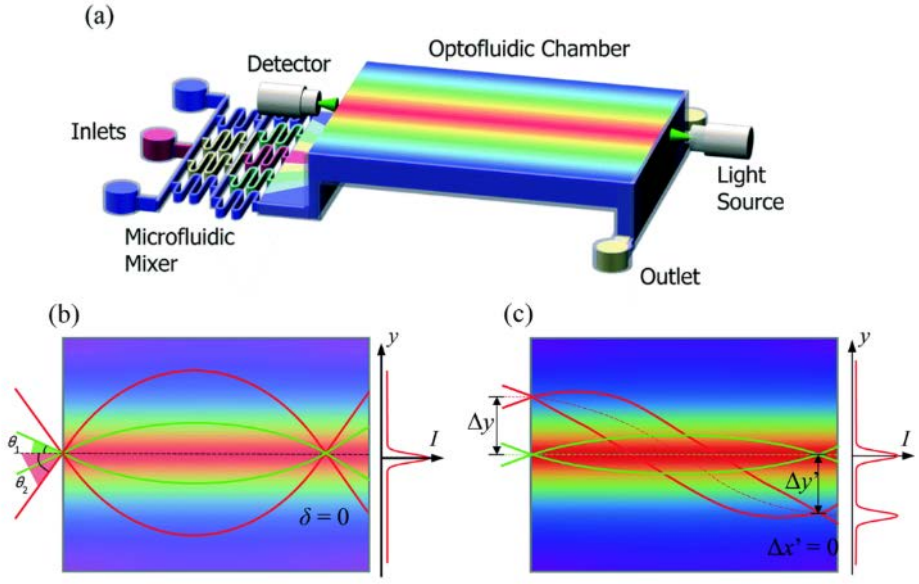

Fig. 2.14 Schematic and working principle of the optofluidic lens [51]. (a) Design of the optofluidic chip. (b) Spherical aberration. (c) Field curvature aberration.

Zhao et al. further improved the performance of the diffusion based optofluidic lens by upgrading the lens design [51], see Fig. 2.14a. By adding a fluidic mixer before the lens section, a HS RI profile can be achieved by precisely

controlling the flow rates of the mixer. Borrowed the idea from aberration-free Maxwell's fisheye lens, such a structure is demonstrated to have a lower spherical aberration (see Fig. 2.14b). It is able to focus the beams to different shifted positions on the same focal plane (Fig. 2.14c).

Temperature conduction is another effective way to form a graded RI profile for beam manipulation in microfluidics. According to the thermal lens effect, the RI decreases linearly while the temperature is increased. Therefore, the RI is lower at the hot region. The rays gradually bend while experiencing an inhomogeneous temperature field. As the magnitude of the thermal conduction coefficient is about two orders larger than that of the molecular diffusion coefficient, the thermal lens effect promises a faster response speed. But the thermo-optics coefficient is relative small, which has a value of $1\sim10 \times 10^{-4}$ K^{-1}. For instance, water has a thermo-optics coefficient of -1.2×10^{-4} K^{-1} at 0~80 °C. The thermal-induced RI is at the order of 0.01, which is much smaller as compared to that derived from the concentration gradient. Tang et al. proposed a thermal-induced optical waveguide by the streams at different temperatures [19]. It utilized two streams at higher temperature (the cladding) to sandwich another stream at lower temperature (the core) to form a temperature gradient across the channel. By simply changing the flow rate, the optical properties of the liquid waveguide can be modified. Yang Yi's group used the thermal gradient to form a GRIN lens for cell manipulation [17] (see subsection 2.5.5).

2.4.4 Others: birefringent lens and Fresnel zone plate lens

Apart from the above mentioned liquid lenses, there are other types of in-plane optofluidic lenses that can also be used for beam manipulation in microfluidic

networks.

In the conventional hydrodynamic liquid-liquid lens, isotropic liquids are used as the core and the cladding, which are polarization independent. However, a polarization-dependent device may find special applications in which the polarized light is preferred. A commonly used polarizable liquid is the LC that has a state between isotropic liquid and totally anisotropic solid crystal, resulting in a partially anisotropic fluid. One of the LC phases is nematic, which is usually uniaxial. It has a preferred long axis and a short axis. The nematic LCs have the fluidic properties similar to ordinary organic liquids, but they can be well aligned by a sufficiently strong electric field. Therefore, the nematic LCs have been widely used in electrically reconfigurable optical devices, such as liquid crystal display. Numerous LC lenses have also been demonstrated [53]. The incident light experiences different RIs according to its polarization. The effective RI can be expressed by

$$n_{eff} = n_o n_e \sqrt{\frac{1}{n_o^2 \cos^2\theta + n_e^2 \sin^2\theta}} \tag{2.5}$$

where θ is the angle between the LC rod and the polarization of the incident light, n_e and n_o are the extraordinary RI and the ordinary RI of the LC molecule, respectively. It is noted that n_{eff} varies from n_o to n_e according to the wave polarization.

Wee et al. demonstrated an in-plane optofluidic birefringent lens by manipulating the streams of a nematic LC and an isotropic liquid under an external electric field [37]. Fig. 2.15 shows the schematic design, in which the nematic LC and the isotropic liquid are used for the main stream and the surrounding sub-

streams, respectively. When an external electric field is applied in the direction perpendicular to the substrate, the LC molecules are reoriented along the electric field, resulting in the birefringent effect in the liquid layer. As ne and no have different values in the nematic LC, the RI difference (i.e., the RI contrast on two sides of the interface) is dependent on the polarization state of the incident light. For the p-polarized light, the effective index equals to no, which is smaller than ne. Therefore, the RI contrast ($\Delta n = n_{\text{eff}} - n_{\text{i}}$) of the p-mode is smaller than that of the s-mode. As a consequence, the s-mode has a smaller focal length (see Fig. 2.15b) than that of the p-mode (Fig. 2.15a). This new type of hydrodynamic optofluidic lens can be modulated by either the flow rate or the polarization of the incident light.

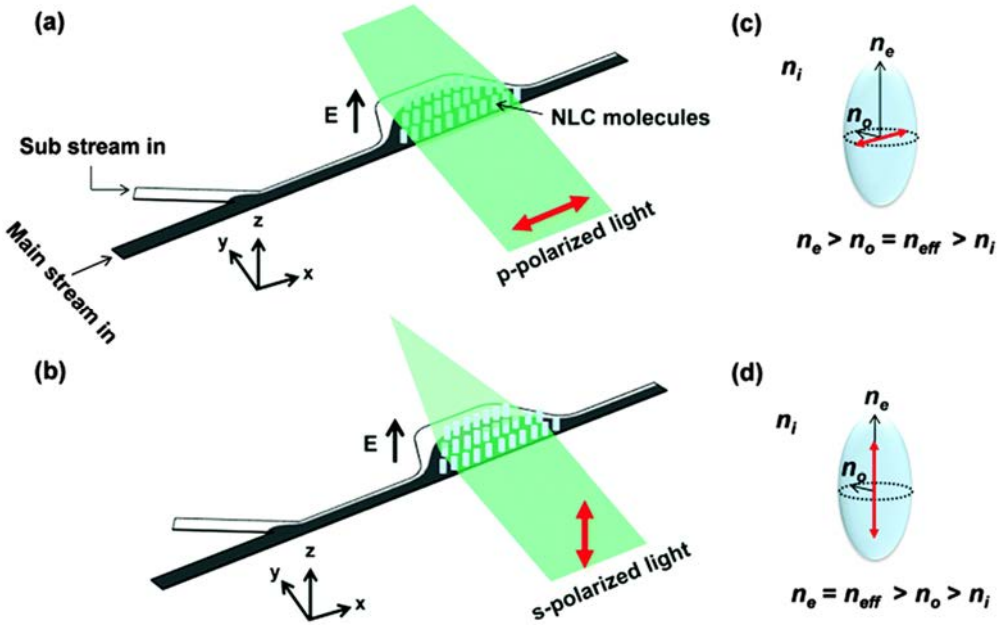

Fig. 2.15 Schematic of the birefringent optofluidic lens [37]: the focusing effect of (a) p-polarized and (b) s-polarized light. Index ellipsoids are used to describe the RI of (c) p-polarized and (d) s-polarized light. The red arrows indicate the direction of polarization.

The traditional lenses focus the light due to the reflection or refraction. While in a Fresnel zone plate (FZP), the light is focused by diffraction, which is

wavelength dependent. Inspired by this idea, Yang's group demonstrated an optofluidic FZP used a solid-liquid hybrid structure [38] (see Fig. 2.16). It utilizes a microfluidic mixer to prepare the liquid with a specific RI, which is delivered to fill the haft wave zone in the FZP. The radius R_m of the mth half-wave zone is described by

$$R_m = \sqrt{m\lambda f} \tag{2.6}$$

where λ and f are the wavelength and the focal length, respectively. When m is an integer, a constructive interference appears at the focus. By tuning the RI of the liquid, it demonstrated the real-time modulation of the optical properties, such as peak intensity, spot size and focal length. In addition, this diffractive device is wavelength sensitive, which can selectively focus the desired wavelength. It also enables the switching between focusing, defocusing and collimation by the flow-rate control.

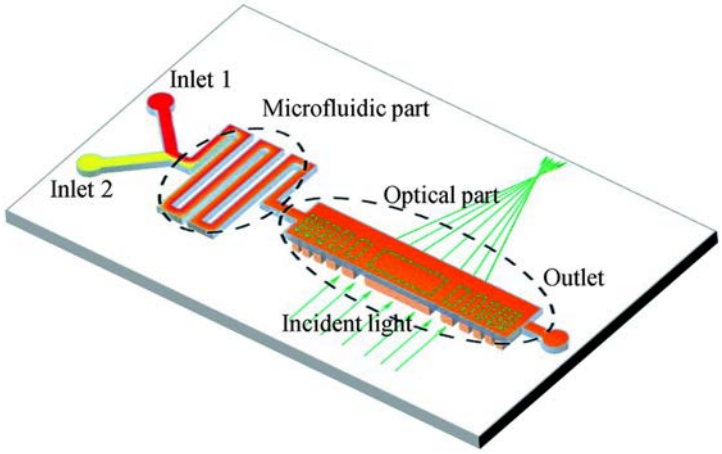

Fig. 2.16 Schematic of the optofluidic Fresnel zone plate (FZP) [38]: it consists of a microfluidic part and an optical part. The former is used to prepare the mixed solution and the latter acts as the tunable FZP.

2.4.5 Applications of in-plane optofluidic lenses

The in-plane optofluidic lenses can be used not only for beam manipulation, but also for some other applications in microfluidic networks, such as particle trapping. Optical tweezers utilize the tightly focused beam to trap particles in the microscale size, providing a noncontact and nondestructive way to manipulate microparticles. The beam is usually focused by an objective lens with large NA and short focal length. In the traditional optical tweezer, the optical alignment is complicated, making it difficult to integrate it into a miniature lab-on-a-chip system. The emergence of optofluidics makes it easy to manipulate the particle using optical tweezers. In addition, sorting and precise moving of particle in 2D area can be easy achieved in optofluidic networks, which are difficult in conventional optical tweezers.

Yang's group proposed a reconfigurable optofluidic thermal GRIN lens and used it for single cell manipulation in the optofluidic chip [17]. As shown Fig. 2.17, the system consists of two parts: the GRIN lens part and the cell trapping chamber. In the GRIN lens section, benzyl alcohol streams at different temperatures are pumped into the chamber to form a GRIN lens to focus the probe beam. And the living cell is contained in the cell trapping part. The cell is trapped and moved by the focused beam. By regulating the thermal lens, the trapping of the living cell can be modulated at a range of 280 μm. Recently, Aiqun Liu's group has demonstrated the manipulation of particles with sizes of several 10s nanometers using optical potential wells created by an in-plane focused beam and fluidic constraints in optofluidic chips [54,55]. The combination of the quasi-Bessel optical profile and the loosely overdamped potential wells enable the precise

manipulation of nanoparticles in the optofluidic channel. They revealed an unprecedentedly meaningful damping scenario that enriches our fundamental understanding of particle kinetics in intriguing optical systems and offered new opportunities for tumor targeting, intracellular imaging, and sorting small particles such as viruses and DNA [55]. The development in particle manipulation using the in-plane beams predicts perspective of the in-plane liquid lens.

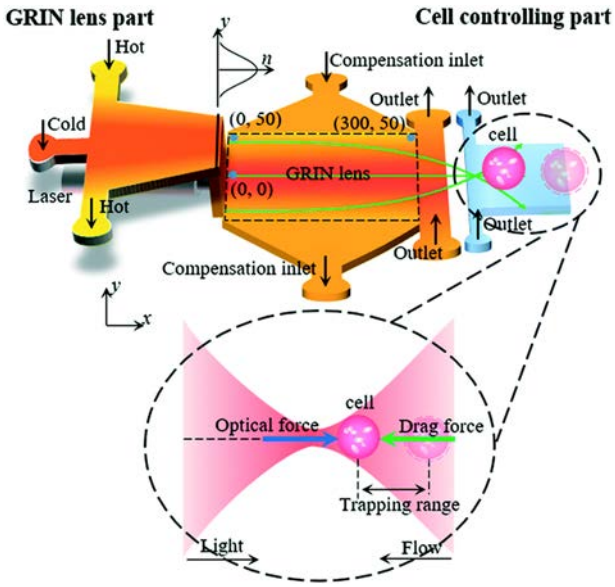

Fig. 2.17 The schematic design of fluidic thermal GRIN lens for cell manipulation [17]: The system includes a lens chamber and a cell trapping chamber. Five streams at different temperatures are injected into the microfluidic chip to form a gradient refractive index across the channel.

The in-plane liquid lens has also been used for particle detection. Flow cytometers have been widely used for particle analysis, sorting and counting. A conventional flow cytometer consists of four main parts, including flow control, light guiding, signal collection and subsequent processing. By the use of optofluidic techniques, the flow cytometer can be integrated into a microfluidic system, reducing the size of the system and making it more portable and durable. The integration allows the benefits of including new optical features on the devices,

such as built-in optical alignment, beam shaping, high optical sensitivity and high accuracy. Zhang et al. gave a comprehensive review about the development of optofluidics based flow cytometers [56]. As the detected particles (or cells) are focused to a narrow stream to ensure that they pass through the optical interrogation point one by one, the measured coefficient of variation (CV) of fluorescent beads is strongly dependent on the beam geometry and bead size. As the beam coming out of the waveguide becomes divergent while it strikes at the interrogation region, a 2D lens is used to reshape and focus the beam, enhancing the beam quality for interrogation. In the past, a micro solid lens was fabricated in between the waveguide and the microchannel to improve the performance of the flow cytometer [57]. The precise fabrication of the waveguide and the solid lens system is required to ensure a good focused spot. While a reconfigurable in-plane lens allows the flexible modulation of the beam after fabrication. In addition, the tuning of the spot size makes it possible to get a low CV while detecting particles with different sizes. Goldin et al. proposed an in-plane liquid-filled lens for flow cytometer [58]. Fig. 2.18 shows an optofluidic flow cytometer by Nguyen's group [59]. It utilized a liquid core/liquid cladding lens to focus the light into a microchannel, where the detected particles flow through. A detection fiber was placed at the opposite side of the sample channel to collect the optical signal for subsequent processing. This compact device incorporated the optical elements and flow control part into a single chip to form a flow cytometer, instead of using bulky optics. This optofluidic flow cytometer demonstrated high efficiency and accuracy on particle counting and sizing. The detection of particles with sizes of 5, 10 and 20 μm was demonstrated. A better focused beam can significantly enhance the performance of the flow cytometers. Recently, Yang et al. gave a detail review on

the development of the micro-optics for microfluidic analytical applications [60].

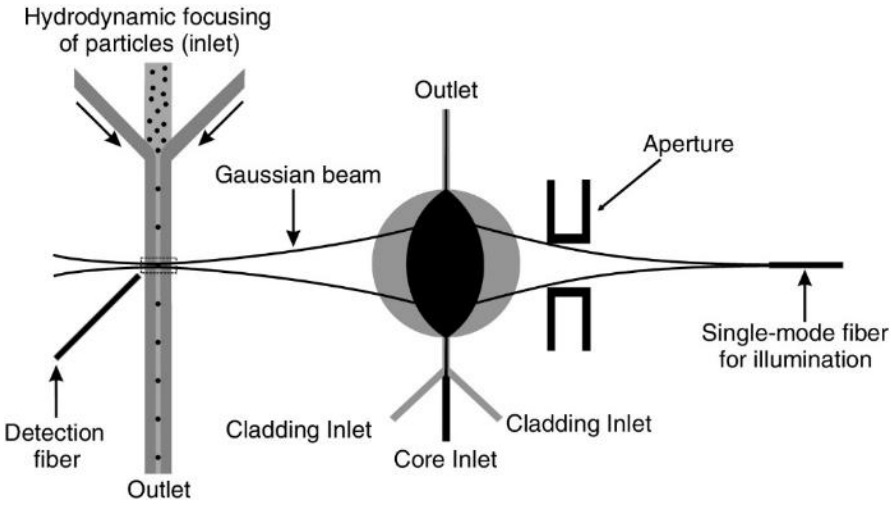

Fig. 2.18 Schematic design of a flow cytometer using optofluidic lens [59].

2.4.6 Discussion

Different types of in-plane optofluidic lenses have been demonstrated, providing numerous methods to manipulate the light in a microfluidic network. In the previous refractive lenses, the liquid-liquid (liquid-air) interfaces are spherical, which may lead to longitudinal spherical aberration (the marginal rays are focused closer to the lens than the paraxial rays). Therefore, the beam can not be well focused into the size close to the diffraction limit. The large focused spot size limits the practical applications. For instance, the CVs in the liquid-lens-based (beam waist 23 μm) cytometer [59] are not as good as those conventional cytometers. However, the aberration can be well-suppressed in the fluidic GRIN lenses. For example, the well-designed thermal lens (the spot size 4 μm) has been used to manipulate the living cells in a microfluidic network [17]. As the reflective liquid lens is modulated through pressure control or hydrodynamics, it promises better robustness. While the liquid GRIN lenses usually use the solution diffusion or the temperature gradient, which are susceptible to the ambient fluctuation. In terms of

response time, the interfacial deformation takes a few seconds to switch to a new balance state. In comparison, a thermal-induced liquid lens has a faster modulated speed. Another limitation is that most of previous in-plane liquid lenses require continuous supply of liquids, which consumes a lot of liquid and reduces the compatibility of the devices. Although there are still some drawbacks, the in-plane optofluidic lenses find useful applications in lab-on-a-chip systems. In addition, the LC-based and FZP-based liquid lenses enable the polarization and wavelength manipulation in a microfluidic chip. It is foreseeable that more liquid lenses will be incorporated into a chip to achieve versatile microsystems.

2.4.7 Perspective of in-plane liquid lens

Based on their working principles and operation methods, the in-plane optofluidic lenses are categorized into three types: refractive lens, gradient index lens and others. The first two cover most of the reported designs, and the last represents some new types, such as birefringent optofluidic lenses and Fresnel zone plate liquid lenses. The in-plane optofluidic lenses have wide tunability, provide a flexible way to manipulate the beam in microfluidic networks and can be easily integrated with lab-on-a-chip systems, making them suitable for transportation and detection of the particle at the same time. It is foreseeable that the in-plane liquid lenses will make the optofluidic networks a versatile platform for research and practical applications. For instance, combing the in-plane beam shaping and microfluidic techniques enables the manipulation and analysis of the particle or cells down to nanometer scale, which may broaden our fundamental understanding of particle kinetics and be useful for biological research. A tightly focused in-plane beam can be used for sample (particle/cell) trapping, transportation, separation and

detection, making it possible to construct a portable integrated system for biochemical applications.

Table 2.1 The summary of the previous in-plane liquid lenses.

Actaution method	*f* / mm	External pumping	Response speed	Power consumption	Aberration free
Pneumatically deform	10 ~ 2	√	2 s	High	×
Laminar flow	∞ ~ 2.75 ∞ ~ -1.21	√	Slow	High	×
Liquid GRIN lens	1 ~ 0.43	√	Slow	High	√
Liquid Crystal lens	6 ~ 3	√	Slow	High	×
Fresnel zone plate	5 ~ 2.5	×	Slow	High	×

2.5 Summary

This chapter reviews the development of optofluidics and some applications of optofluidic devices. Specifically, the reconfigurable optofluidic lenses are discussed in two groups: out-of-plane lens and in-plane lens. Due to the similarity with the conventional solid lens, the out-of-plane lens can be used to replace the solid one in imaging optics. While the in-plane liquid lens is compatible with other components in a microfluidic chip, where particle trapping, sensing can be achieved. The characteristic parameters of the previous in-plane liquid lenses have been summarized in table 2.1 for easy comparison. Although several in-plane optofluidic lenses have been demonstrated, there are still some limitations in the previous liquid lenses. For instance, the RI modulated lens need to be located at the entrance of the flow streams. The interfaces of the in-plane refractive lenses can only be modulated by flowing immiscible streams, which consumes much solution and constraints its compatibility. In addition, the fluidic interfaces have a

spherical shape, which has a positive longitudinal spherical aberration. This doctoral study will try to develop new in-plane optofluidic lenses to solve the above problems.

Chapter 3 Device Fabrication Techniques

The research project of this thesis focuses on primarily theoretical analysis and experimental measurements. To accomplish the experimental analysis of the designs, some specific microfluidic devices should be fabricated. This chapter describes the main procedures of the device fabrication, namely the microfabrication, including photolithography, sputtering and microfluidic chip bonding, etc. All the devices used in this doctoral study are fabricated in the University Research Facility in Materials Characterization and Device Fabrication (UMF) of the Hong Kong Polytechnic University.

3.1 Brief description of device fabrication

The optofluidic devices need to be fabricated using the micro technology due to their miniature dimensions and specific structures, such as the metal stripes and the microelectrodes, which require micro pattern and thin film deposition, namely the lift-off process [61]. They are fabricated in the cleanroom environment using conventional lithography procedures. For example, the two metal stripes made of Chromium (the thermal lens in Chapter 4) are fabricated used standard lift-off method, which includes lithography and thin film deposition. In the experiments, the metal strips are used to absorb the pump laser to heat up the liquid, forming a thermal gradient inside the microfluidic chip. While the channel of the microfluidic chip is fabricated by a customized pattern transfer technique, which includes PDMS pattern fabrication and capillary filling assisted bonding by NOA 68. Top and bottom of the chip are silica glasses, which are bonded together by the NOA68 adhesive in between of them. The DEP actuated liquid lenses are also

fabricated using the above methods. A brief description of the fabrication procedure of the microfluidic chip is as follows:

1. Lift-off film fabrication: Firstly, some patterns of AZ5214 photoresist are fabricated on the bottom by photolithography. Secondly, sputtering film deposition is used to deposit a thin film of chromium on the patterned glass. Lastly, the sample is immersed in acetone to remove the unwanted area, leaving the metal strips on the glass.

2. Microchip fabrication: Step one: A SU-8 50 photoresist mold is fabricated on the wafer, which will be used to construct the PDMS pattern later. Step two: the patterned PDMS is peeled off and attached to the glass bottom, forming an open channel for capillary filling of NOA 68. After the UV exposure, the PDMS pattern is taken away, leaving the partially cured NOA 68 on the glass. Step three: a glass cover is bonded onto the bottom by the NOA 68 spacer.

3.2 Lift-off fabrication of metal strip

The lift-off process is used to fabricate the film pattern on the substrate (e.g. glass) [61]. It is a very good supplement to the conventional structuring methods like etching. The size of the structure scales from nanometer up to centimeters, but it is mainly at the micrometer scale. Generally, it consists of two parts: lithography and film deposition.

3.2.1 Schematic process of lift-off fabrication

Fig. 3.1 describes the fabrication procedures of the lift-off process. At the beginning, the glass substrate is cleaned using ultrasonic by acetone for ten minutes. Then repeat the cleaning procedure using isopropyl alcohol (IPA),

ethanol and distilled water (DI water) in sequence, respectively. After that, the sample is dried by compressed nitrogen and put on the hotplate at 120℃ for twenty minutes. Then, an AZ5214 photoresist thin film (thickness = 2 μm) is coated on the substrate by spin coating, see Fig. 3.1a. In the coating process, a drop of photoresist is place on the sample, then the spin coater ramps up to 1000 revolution/minute in 2 seconds and hold for 5 second. After that, it goes up to 4000 revolution/minute and hold for 35 seconds. Before UV exposure, the sample is put on a hotplate and keep at 100℃ for three minutes to dry the photoresist. Then, the sample experiences 10 seconds UV exposure, which transfers the pattern of the mask to the photoresist layer (Fig. 3.1b). The UV exposure is conducted using the Suss MA6 mask aligner shown in Fig. 3.2. As AZ5214 is a positive photoresist, the UV exposure changes the chemical property of the photoresist and makes it soluble in the developer. To remove the unwanted section, the sample is put into AZ300K developer for 15 seconds and then flushed by DI water. The patterned sample is put on the hotplate at 120℃ again to get it dried. As shown in Fig. 3.1c, a layer of the AZ5214 photoresist pattern is left on the substrate. Therefore, only the patterned area is exposed to air, making the deposited material get direct contact to the substrate. Before the film deposition, the sample is cleaned by the Oxygen Plasma, which further remove the residual thin film of the photoresist in the exposure area. A chromium thin film (with a thickness of 1 μm) is deposited on the sample by sputtering (more details can be found in the following section), see Fig. 3.1d. In the lift-off process, the sample is put into the Acetone for 30 minutes, the sacrificial layer is dissolved by Acetone, removing target material in the unwanted area. Fig. 3.1f shows the result of the lift-off procedure: two Cr strips

are fabricated on the glass substrate.

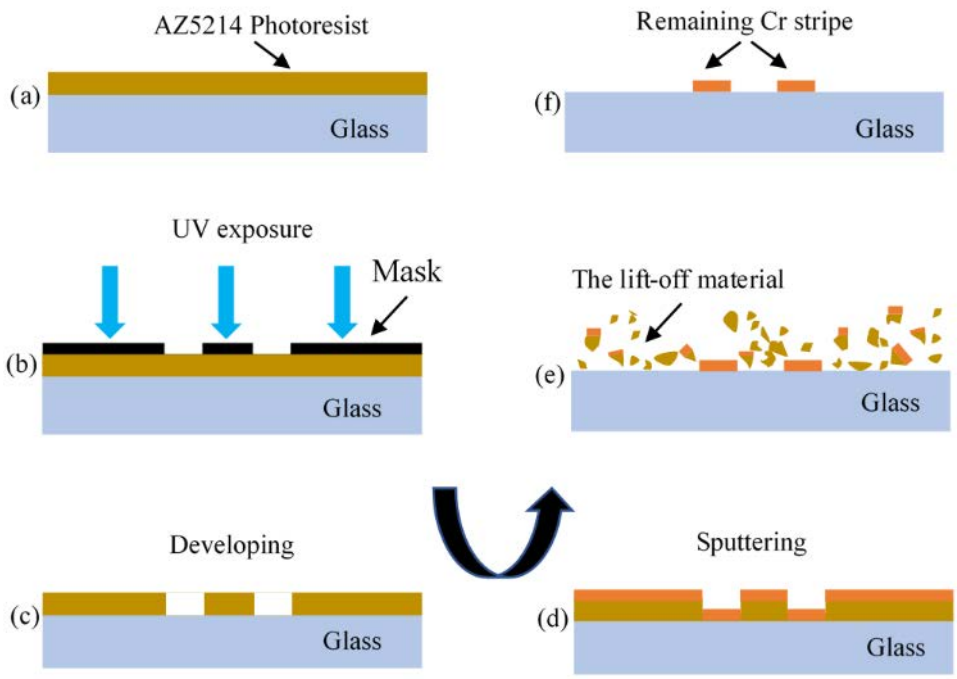

Fig. 3.1 Schematic of the lift-off fabrication process: (a) AZ5214 photoresist is coated on the glass substrate. (b) Pattern transfer using UV exposure. (c) A sacrificial layer of photoresist is fabricated on the substrate. (d) A thin film of Chromium is deposited on the sample by sputtering. (e) The unwanted area is removed by Acetone. (f) The cross-section view of the fabricated metal strips.

3.2.2 Experimental results of lift-off fabrication

The experimental result is shown in Fig. 3.3. At first, the AZ5214 photoresist pattern is coated on the substrate by photolithography, see Fig. 3.3a. Then two chromium strips are deposited on the substrate using DC sputtering. The lift-off result is shown in Fig. 3.3b.

Fig. 3.2 Suss MA6 Mask Aligner: Light source of 350 W UV light at 365 nm; Resolution < 0.8 μm; Alignment accuracy < ±0.5 μm; Substrate up to 4-inch round wafer.

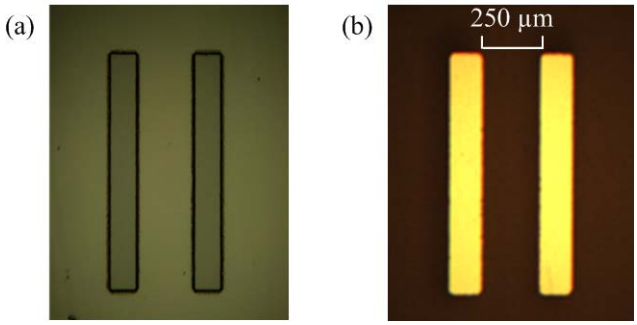

Fig. 3.3 The lift-off fabrication result of Chromium strips: (a) The photolithographic pattern of AZ5214 photoresist. (b) Two chromium strips are fabricated using the lift-off process, the with and length of the strips are 125 μm and 1 mm, respectively. And the side to side distance is 250 μm.

The magnetron sputtering film deposition is a physical process, in which a magnetically confined plasma is created near the surface of the target. Positively charged energetic ions from the plasma collide with the negatively charged target material. Atoms from the target are ejected or "sputtered", which then deposit on a substrate to form a film, see Fig. 3.4a. Magnetron sputtering uses a closed magnetic field to trap electrons, increasing the efficiency of the initial ionization process and creating plasma at lower pressures, reducing both background gas

incorporation in the growing film and energy losses in the sputtered atom through gas collisions. Magnetron sputtering is often used for deposition of metallic and insulating coatings that have specific optical or electrical properties. The appearance of the Denton Vacuum explorer is shown in Fig. 3.4b. In this study, the sputtering is utilized to deposit Chromium film and Indium Tin Oxide patterns. The sputtering parameters are shown in Table 3.1. As the AZ5214 can not withstand high temperature, the sputtering process is conducted at room temperature. To make the ITO film conductive, the ITO pattern is put into an oven at 300 ℃ for annealing [62].

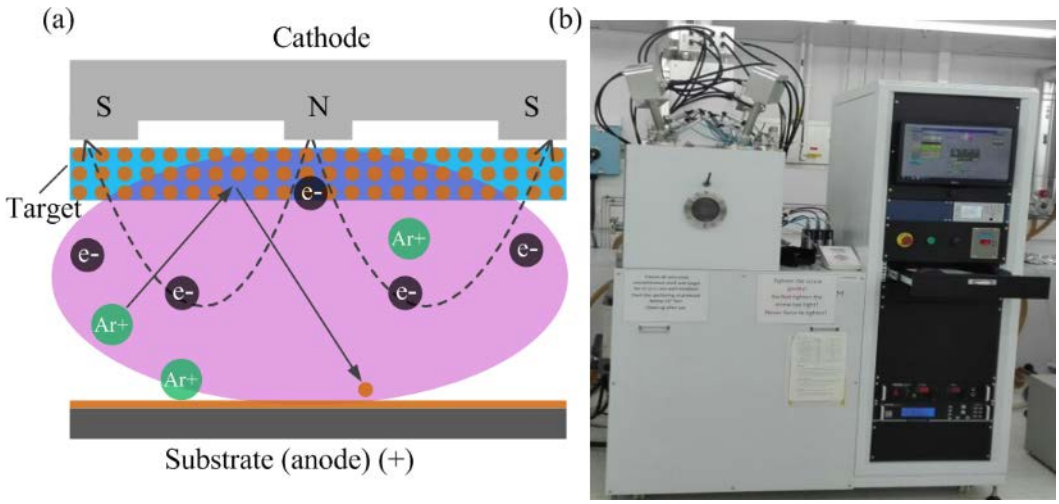

Fig. 3.4 Magnetron Sputtering: (a) The schematic of the sputtering process. (b) Appearance of the Sputtering system: Denton Vacuum explorer.

Table 3.1 The parameters of the sputtering process in this study. Two different materials: Chromium (Cr) and Indium Tin Oxide (ITO) are deposited using the DC sputtering. Here P_0: base pressure, P_1: working pressure, v_1: flow velocity of Argon, v_2: flow velocity of Oxygen, Power: DC power, T: time of deposition, Thickness: thickness of the film

Material	P_0 (mTor)	P_1 (mTor)	v_1 （sccm）	v_2 （sccm）	Power (W)	T (s)	Thickness (μm)
Cr	8×10^{-7}	3	30	0	160	650	1.07
ITO	8×10^{-7}	3	25	5	160	1200	0.103

3.3 Microchip fabrication by capillary filling assisted method

Most of the microfluidic chips are made of Polydimethylsiloxane (PDMS) due to its unique properties, such as biocompatible, optically transparent and easy to be molded into different shapes, etc. Because of its optical transparency and easily curable by UV exposure, UV adhesives (Norland Optical Adhesive series, NOA in short. Such as NOA81 and NOA68) have also been used in many microfluidic applications [63–66] . In comparison with PDMS, NOA 81 adhesive has many advantages in some specific applications. It shows a stronger chemical resistance to organic solvent than PDMS. The NOA provides adhesives with excellent combination of physical and optical properties. For example, the elastic modulus of the NOA products can be chosen from a large scale. A stronger elastic modulus promises a higher aspect ratio, which is limited in PDMS. In addition, it offers products with RI ranging from 1.3 to 1.7, which is crucial in optical applications. In contrast to PDMS, NOA 68 is impermeable to water and air, providing a better sealing performance. Similar to PDMS, the soft imprint structure of the UV curable adhesive can be down to submicrometer. Numerous easy and low-cost microfabrication methods have been demonstrated using UV curable adhesives, such as rolling assisted bonding [63], Stamp-and-Stick bonding [67], plasma bonding [66], etc.

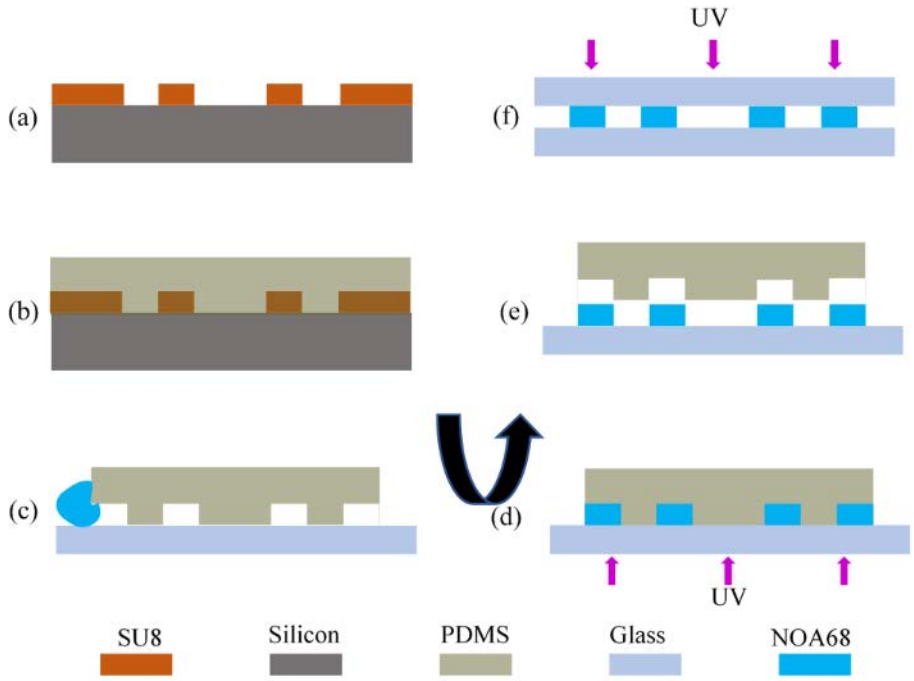

Fig. 3.5 Sketch of the capillary filling assisted microchip fabrication process. (a) SU-8 50 mold on Silicon wafer. (b) PDMS pattern replicated from the SU-8 50 master. (c) Put the PDMS into contact with a glass substrate and fill the gap with NOA68 by capillary flow. (d) Partially cure the NOA68 by UV exposure. (e) Peel the PDMS away and leave the NOA68 pattern on the substrate. (f) Cover it with top glass and glue them together by UV exposure.

3.3.1 Capillary filling assisted microfluidic chip fabrication

In this project, a PDMS assisted capillary filling method is used to fabricate the microfluidic chip. Fig. 3.5 shows the schematic process of the microchip fabrication using the NOA68 as the intermedia to glue two glasses together. The NOA68 is chosen as the spacer for the thermal lens project because of the RI matching between NOA68 (n_{NOA68} = 1.540) and Benzyl Alcohol (n_{BA} = 1.539). As shown in Fig. 3.5a, a SU-8 50 mold is fabricated on Silicon wafer using conventional photolithography technique (it will be described in detail in the following section). In step two, the SU-8 50 mold is used to construct a PDMS pattern, which will be used to transfer the pattern to NOA 68 adhesive later. Peel the patterned PDMS away from the Silicon wafer and put it into contact with glass

substrate, as shown in Fig. 3.5c. The PDMS is attached to the substrate, forming a micro channel for capillary flow. When a drop of NOA 68 adhesive is placed at the edge of the PDMS on the glass, the capillary fore drives the adhesive to fill the gap between the PDMS and glass (see Fig. 3.5d). Then, UV exposure (2 minutes) is applied to partially cure the NOA 68. As the PDMS is permeable to air and oxygen inhibits the free-radical polymerization of liquid NOA68, there will be a thin layer of uncured NOA 68 near the PDMS surface. After that, the PDMS is peeled away gently, leaving the NOA 68 pattern layer on the bottom, see Fig. 3.5e. At last, a glass cover is put on the NOA 68 pattern and press gently to get good contact. Subsequently, UV exposure (2 minutes) is used to cure the active NOA 68 and bond the two glasses together firmly (see Fig. 3.5f). By far, a microfluidic chip make of glasses has been fabricated.

3.3.2 SU-8 50 mold fabrication and PDMS pattern preparation

The capillary filling assisted method is used to fabricate the microfluidic chip of thermal lens for experimental measurement. Before the bonding process, a SU-8 50 mold is fabricated to prepare the PDMS pattern for capillary filling of NOA 68. The standard photolithography is used to fabricate the SU-8 50 mold on a 3-inch silicon wafer. First, the silicon wafer is cleaned by Acetone, Iso Propyl Alcohol (IPA), Ethanol and Distilled Water (DI water) using ultrasonic for 10 minutes, respectively. Then the wafer is dried by compressed Nitrogen and put on the hotplate at 150℃ for 30 minutes. To fully clean the wafer, 5-minute plasma cleaning is used to clean the surface of the sample. Then a SU-8 50 film is coated on the wafer using spin coater (800 revolution/minutes for 30s, and 2000 revolution /minute for 60s). Next, soft bake is used to evaporate the solvent and

densify the film. The sample is placed on the hotplate at 60℃ for 5 minutes. Then, the hotplate is set to be 65℃ for 6 minutes and 95 ℃ for 20 minutes. It is cooled down to 25℃ on the hotplate. After that, the sample is placed on the Suss MA6 Mask Aligner for UV exposure (350 W for 20 s), which transfers the pattern of the mask to the SU-8 50 film. The UV illuminated SU-8 50 photoresist becomes cross-linked in the post baking process. The sample is placed on the hotplate at 65℃ for 1 minute and 95℃ for 5 minutes. At last, the cross-linked sample is put into the developer for 5 minutes, removing the unwanted photoresist. The fabricated SU-8 50 mold of the thermal lens project is shown in Fig. 3.6a. It shows that a SU-8 50 pattern is left on the silicon wafer. The thickness of the film is about 45 μm.

Then the SU-8 50 mold is used to prepare a PDMS pattern for capillary filling. At first the precursor SYGARD^{TM} 184 Silicone Elastomer Base and the Elastomer Curing Agent are mixed with the weight ratio of 10:1. Then the mixer of the PDMS solution is poured onto the silicon wafer and stored at room temperature for 30 minutes to remove the air bubbles inside the solution. To fully cure the PDMS, the sample is put into an oven at 70 ℃ for two hours. After the curing process, a PDMS pattern can be peeled off the silicon wafer for capillary bonding. A PDMS pattern is shown in Fig. 3.6b. As the SU-8 50 photoresist is cross-linked on the silicon wafer, it can be reused for many times.

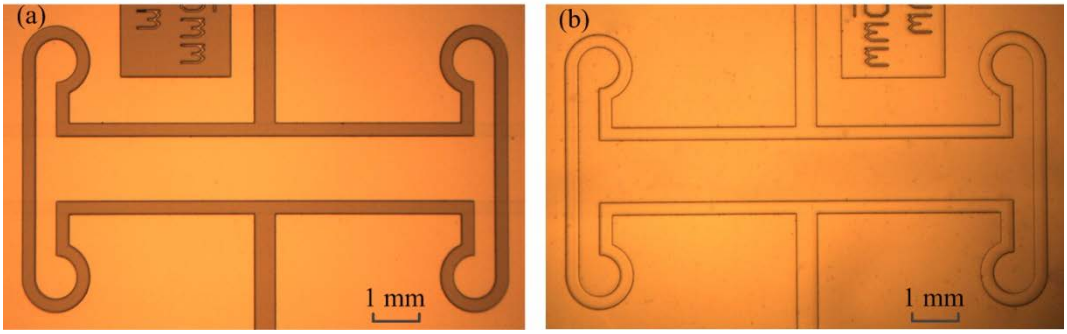

Fig. 3.6 The SU-8 50 mold and PDMS pattern of the thermal lens project. (a) The SU-8 50 mold fabricated on a 3-inch wafer by photolithography. (b) The peeled off PDMS pattern.

3.3.3 Capillary filling assisted bonding process

The bonding process is shown in Fig. 3.7. At first, the PDMS is peeled off from the SU-8 50 mold, which will be aligned and got into contact with the substrate using the 3D position stage. The PDMS pattern forms a microchannel on the substrate for the subsequent NOA 68 filling, see Fig. 3.7a. A bit of NOA 68 adhesive is placed at the inlet of the PDMS channel. The adhesive automatically flows into the channel due to capillary force, see Fig. 3.7b. The two red arrows indicate the flow directions of the fluidic adhesive. At 10 minutes, the filling state is shown in Fig. 3.7c. It takes about 21 minutes to fill all the channel path, as shown in Fig. 3.7d. A closed channel is filled with NOA 68 by far. Then the sample experiences a 2-minute UV exposure to partially cure the NOA 68. After that, the PDMS is peeled off from the substrate, leaving the partially cured NOA 68 pattern on the glass (Fig. 3.7e). The thickness of the NOA 68 pattern is 45 μm. On top of the NOA 68 pattern, there is a thin layer of active adhesive, which will be used to bond the cover to the substrate. A piece of silica glass with four punched holes is aligned and put into contact with the substrate. At last, 2-minute UV exposure is used to fully cured the NOA 68 spacer, as shown in Fig. 3.7f. Compared with the PDMS bonding microchannel, the UV bonding microfluidic chip can withstand a

higher pressure. A 24-hour aging at 80 ℃ can enhance the strength of the NOA 68 spacer. The fabricated device of the optofluidic tunable thermal lens is shown in Fig. 3.8. The size of the device is 2.5 cm × 2.5 cm × 0.3 cm (L×W×H). Four metal tubes are used to connect the chip to the microfluidic tubes.

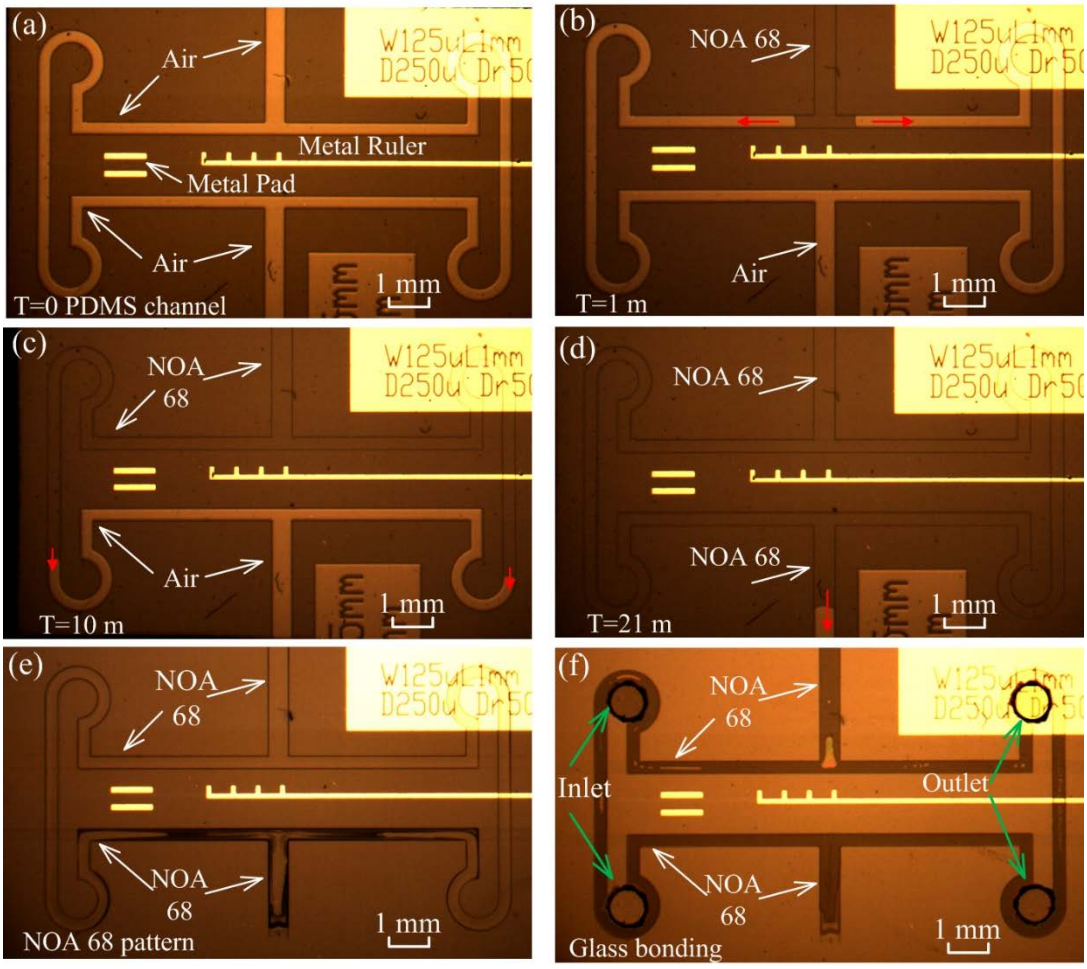

Fig. 3.7 Experimental bonding process of the Microfluidic chip (Thermal lens) using NOA 68. (a) The PDMS pattern get into contact with the glass substrate, forming a micro channel for capillary filling. (b) The NOA 68 automatically flows into the PDMS channel. (c) The filling state at T = 10 minutes. (d) At T = 21 minutes, the capillary filling is finished. (d) After 2 minutes UV exposure, the NOA 68 is cured. Peel the PDMS off, the NOA 68 pattern is left on the substrate for microfluidic chip bonding. (f) Align and put the cover into contact with the substrate, the bonding is achieved by UV exposure. Four punched holes in the cover are used as the inlets and outlets.

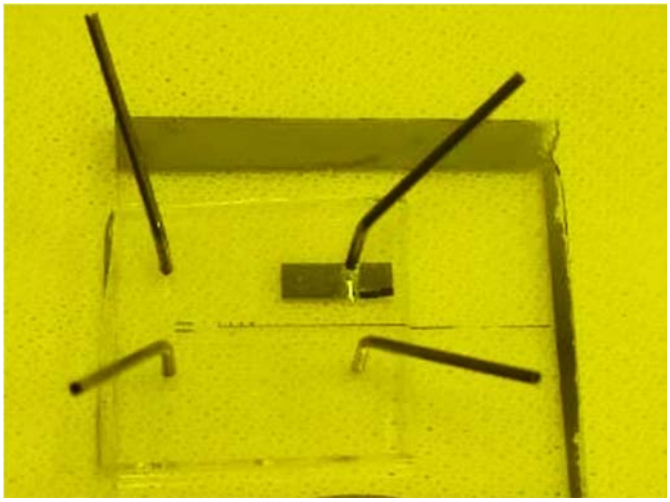

Fig. 3.8 Fabricated device of the optofluidic tunable thermal lens. Four metal tubes are chosen as the connector. The device has a dimension of about 2.5 cm × 2.5 cm × 0.3 cm.

By far, microfluidic chip fabrications: lift-off film deposition and capillary bonding technique have been introduced. The other two kinds of optofluidic lenses are fabricated used the similar methods except for the different thickness and the electrode material.

3.3.4 Fabrication of DEP lenses

Table 3.2 The parameters of the SU-8 50 molds fabrication. Here, rmp: revolution per minute.

Thickness (μm)	Spin speed (rpm)	Prebake @65℃ (minute)	Softbake @95℃ (minute)	UV exposure (second)	PEB 1 @65℃ (minute)	PEB 2 @95℃ (minute)	Develop minute
45	2000	6	20	20	1	5	5
55	1940	10	30	25	1	10	7
60	1900	10	30	25	1	10	8

The DEP lenses are fabricated using the above techniques.

(1) Fabrication of the DEP actuated lens with one liquid-air interface

To fabricate a microfluidic chip using the above capillary filling assisted bonding technique, a SU-8 50 mold should be prepared first. Table 3.2 shows the

parameters of the SU-8 50 mold fabrication process in this doctoral study. The fabrication process of the microfluidic chip is sketched in Fig. 3.9. A SU-8 50 mold with the thickness of about 55 μm is fabricated using photolithography, see Fig. 3.9a. Then the PDMS assisted pattern transformation is used to copy the mold to NOA 81 as shown in Fig. 3.9b. To form an open microfluidic chip, another glass with ITO layer is bonded onto the spacer using the thin layer of active NOA 81. Fig. 3.9c displays the bonded device, which has an open channel, an inlet at the left side, an electrode in the middle of the channel. The appearance of the whole device is shown in Fig. 3.9d.

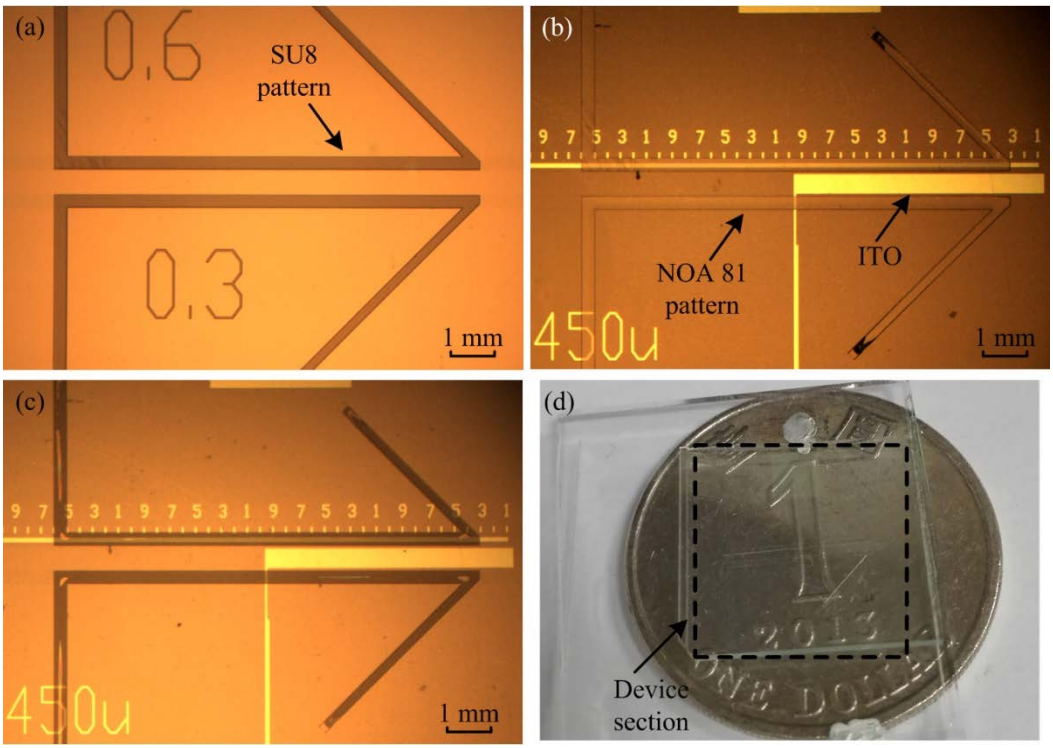

Fig. 3.9 Fabrication of the DEP lens with single liquid-air interface. (a) SU-8 50 pattern on the silicon wafer. (b) NOA 81 pattern on the glass. (c) Another ITO glass is bonded onto the NOA81 spacer to form the device. (d) Appearance of the fabricated device.

(2) Fabrication of the DEP actuated lens with two liquid-air interfaces

The fabrication of the DEP lens with two liquid-air interfaces is shown in Fig. 3.10. At first, a SU-8 50 mold with thickness of 60 μm is fabricated on a 3-inch silicon wafer, see Fig. 3.10a. Then the mold is used to transfer the pattern to a PDMS, which will be used for the capillary filling. The NOA81 spacer is fabricated on the MgF_2 glass, as shown in Fig. 3.10b. The glass is coated with ITO using the lift-off technique mentioned above. Next, an ITO glass is put into contacted with the NOA81 spacer. And the bonding is achieved by UV exposure, which fully cures the active layer of the NOA 81 adhesive. The bonded device is displayed in Fig. 3.10c. And the layout of the device is shown in Fig. 3.10d. It is noticed that the device has a separated raytracing chamber for experimental raytracing.

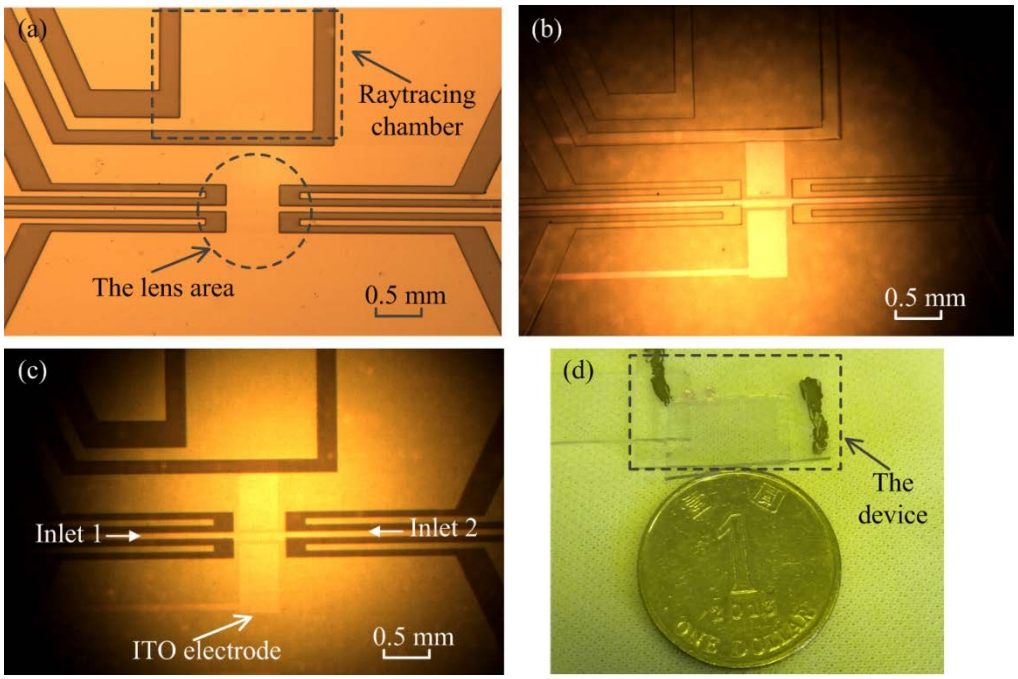

Fig. 3.10 The fabrication of the DEP actuated lens with two liquid-air interfaces. (a) SU-8 50 mold. (b) NOA 81 pattern fabricated by capillary filling and UV curing. (c) The bonding device. (d) The appearance of the device.

3.4 Summary

This chapter introduces the devices fabrication of this doctoral study. At first, the thin film pattern (Chromium or ITO) is deposited on the substrate using lift-off technique, which includes the photolithography and sputtering film deposition. To fabricate the microfluidic chip, a new bonding technique is developed. It is based on the capillary filling of NOA68 or NOA81 optical adhesives. The devices were successfully fabricated using the above methods.

Chapter 4 Optofluidic Tunable Lenses using Laser-induced Thermal Gradient

This work is reproduced in part from "Optofluidic tunable lenses using laser-induced thermal gradient" *Lab on a Chip*, 16(1), 104-111 (2016) by Q.M Chen, A.Q Jian, Z.H Li, & X.M Zhang, with the permission of The Royal Society of Chemistry.

Based on the fabrication processes in the previous chapter, this chapter will present the first design of tunable lens: a new optofluidic tunable lens using a laser-induced thermal gradient. It makes use of two straight chromium strips at the bottom of the microfluidic chamber to absorb the continuous pump laser to heat up the moving benzyl alcohol solution, creating a 2D RI gradient in the entrance part between the two hot strips. This design can be regarded as a cascade of a series of refractive lenses, which is distinctively different from the reported liquid lenses that mimic the refractive lens design and the 1D gradient index lens design. CFD simulation shows that a stable thermal lens can be built up within 200 ms. Experiments are conducted to demonstrate the continuous tuning of focal length from initially infinite to the minimum 1.3 mm, as well as the off-axis focusing by offsetting the pump laser spot. Data analyses show the empirical dependences of the focal length on the pump laser intensity and the flow velocity. Compared with previous studies, this tunable lens design enjoys many merits, such as fast tuning speed, aberration-free focusing, remote control, and enabling the use of homogeneous fluids for easy integration with other optofluidic systems.

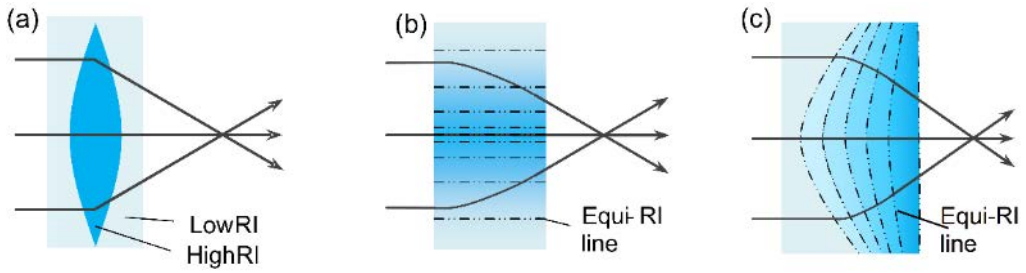

Fig. 4.1 Working principles of two typical designs and our new design of an optofluidic lens. (a) Refractive lens design, which mimics the concept of conventional solid curved-interface lenses and utilizes immiscible flows with different refractive indices to create curved interfaces. The focusing effect is obtained by the sharp bending of the rays at the curved interfaces of two homogeneous media. (b) 1D-GRIN lens design, which mimics the concept of conventional solid GRIN lenses, which have a parabolic distribution refractive index in the transverse direction and the equi-RI lines parallel to the central line. The continuous change of the RI is obtained by mixing miscible fluids of different RIs or by introducing a temperature gradient in a homogeneous fluid. The rays are bent inwards gradually. (c) New 2D-GRIN lens design, which has the gradient index changes in both the longitudinal and transverse directions. The equi-RI lines are curved, making it like the cascade of many refractive lenses along the optical axis. This design can be regarded as a combination of the refractive lens design and the GRIN-lens design

4.1 Brief introduction

Various optofluidic designs have been developed for in-plane focusing [13], and they can be broadly classified into two categories: refractive lens design and one-dimensional gradient index (1D-GRIN) lens design as shown in Fig. 4.1. The refractive lens design mimics the concept of conventional solid lenses with curved interfaces as illustrated in Fig. 4.1a. It typically creates curved interfaces using immiscible fluids of different RIs and has step change of RI across each interface. In contrast, the 1D-GRIN lens design mimics the concept of conventional solid GRIN lenses (see Fig. 4.1b), and commonly generates a continuous change of the RI by mixing miscible fluids of different RIs [31] or by introducing temperature gradient in a homogeneous fluid [19]. In the ideal case, the equi-RI lines are all

straight and parallel to the optical axis (see Fig. 4.1b).

In this chapter, we will propose another design of optofluidic tunable lens, which can be regarded as a combination of the previous two designs (see Fig. 4.1c) and is realized by using the laser-induced thermal gradient. It is able to overcome the existing constraints and brings in additional benefits. Detailed discussions on the working principle, the device design and the experimental results will be presented below, followed by some discussions.

4.2 Working principle

The conceptual design of the new type of optofluidic lens is shown in Fig. 4.1c. It has RI gradient changes in both the longitudinal and the transverse direction (called 2D-GRIN lens), thus the equi-RI lines are in curved shape. These features are distinctively different from the typical 1D-GRIN lens design that has the RI gradient only in the transverse direction and has the equi-RI lines in the straight shape. Compared with the typical refractive lens design, the 2D-GRIN lens design looks like the cascade of a series of refractive lenses along the optical axis. Simply speaking, the focusing effect of the 2D-GRIN lens design is obtained by gradually bending the rays to one point and can be tuned by varying the RI gradient profile.

In theory, one of the RI gradient profiles that can realize aberration-free focusing should follow the square-law parabolic function as given by

$$n(r) = n_c \sqrt{1 - A\left(\frac{r}{R}\right)^2} \tag{4.1a}$$

where $n(r)$ is the RI gradient along the transverse direction, n_c is the highest RI at the center, A *is* the parabolic parameter, r is the radial coordinate in the transverse

direction, and R is the constant. It is noted that Eq. (4.1a) is suitable for the 1D-GRIN lens. In our work, the RI gradient is 2D and thus the relationship is changed to

$$n(r,z) = n_{c,z}\sqrt{1 - A_z r^2} \tag{4.1b}$$

here $n(r, z)$ is the RI at point (r, z), z is the coordinate position along the flow direction, $n_{c,z}$ is the RI at the central position $(r = 0, z)$, A_z is the parabolic parameter.

In the 2D space, the ray trajectories inside an optical medium are determined by

$$\frac{d}{ds}\left[n(r,z)\frac{dr}{ds}\right] = \nabla n(r,z) \tag{4.2}$$

where s is the path length.

The tuning of RI can be obtained by varying the temperature. According to the thermo-optics effect, the RI of liquid is a function of the temperature as approximated by [70]

$$n(T) = n_0 + \frac{dn}{dT}(T - T_0) \tag{4.3}$$

here n_0 is the RI at the reference temperature T_0, and dn/dT is the thermo-optic coefficient of the solution, which is usually a negative value.

In this work, CFD (computational fluidic dynamics) and optical ray tracing simulations are conducted to find an optimized design of tunable liquid lens. First, a CFD programme is conducted to calculate the heat transfer by considering the microchip geometry and the flow parameters. Then, the temperature field is

converted into a temperature-induced RI gradient field. Finally, we simulate the ray tracing in the RI gradient field. In experiment, the temperature field is measured by filling the microchip with the rhodamine B fluorescence solution, whose fluorescence emission is strongly dependent on the temperature [71]. More details of the simulation and the temperature measurement can be found in the following section.

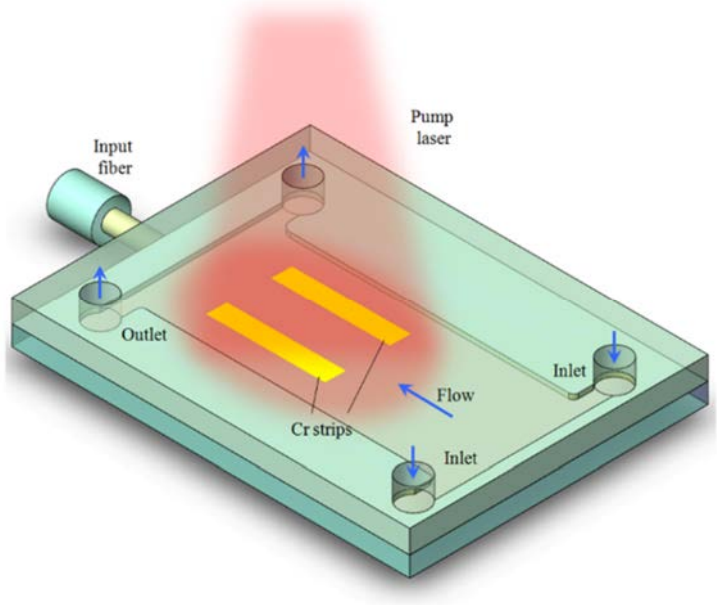

Fig. 4.2 Schematic diagram of the new optofluidic tunable lens device. It has two inlets at one end and two outlets at the other end. Two silica glasses are used as the top and bottom. An NOA68 layer sandwiched by the two glasses is the spacer and the structural layer, which defines a rectangle chamber inside the chip. Two chromium strips are coated on the bottom glass to absorb the pump laser for heat generation. The heat transfer from the strips to the liquid and the motion of liquid work together to create a temperature field and thus a refractive index gradient. Under proper conditions, the refractive index gradient can focus the probe light from a fiber laser to a tunable point.

4.3 Device design and fabrication

4.3.1 Device design

The schematic design of optofluidic tunable lens device is illustrated in Fig. 4.2.

It consists of three separate parts: a microchip, a pump laser and an optical fiber. The microchip is the core part for fluidic control and light focusing; the pump laser is mounted above the microfluidic chip for light irradiation; and the optical fiber is used to couple the probe light into the microchip for determination of the focusing effect. The microchip has three layers in the vertical direction: the top and the bottom are silica glass slides (n_{silica} = 1.46), and in between is the microfluidic structural layer for a rectangular microchamber. Two inlets and two outlets are arranged symmetrically to balance the input and output of liquid. The microchamber is 5 mm long, 1.5 mm wide and 45 μm high. The height is intentionally chosen very small so that the flow convection in the heating process is negligible. This helps sustain the state of laminar flow even when part of the liquid is heated. The microchamber is photolithographically patterned by NOA68 optical adhesive (n_{NOA68} = 1.540). Two chromium straight strips (width = 125 μm, length = 1 mm, thickness = 1 μm, center-to-center separation = 375 μm) are coated on the bottom glass by magnetron sputtering as the microheaters. For the pump laser, continuous laser from a semiconductor diode is guided through a multimode fiber (λ = 980 nm, NA = 0.22, D_{core} = 200 μm) to irradiate the metal strips, whose absorption heats up the liquid to establish a sustainable temperature gradient. The pump laser fiber is mounted over the microchip and controlled by an optical stage to precisely adjust the laser spot position on the microchip. Green light (λ = 532 nm) is coupled into the microchip through a pigtailed lensed fiber collimator. Benzyl alcohol is chosen as the liquid to fill the microchamber. This is because benzyl alcohol has very low absorptions at 520 nm and 980 nm, a high thermo-optic coefficient ($dn/dT = -5.1 \times 10^{-4}$ K^{-1}), a high boiling point 203 °C, a low heat transfer coefficient and a suitable viscosity. In addition, benzyl alcohol has a RI of

n = 1.5389 at 25 ºC, which closely matches the RI of NOA68 adhesive (n_{NOA68} = 1.540) for easy optical propagation in the horizontal plane, and it is higher than that of the top and bottom glass slides (n_{silica} = 1.46) for optical confinement in the vertical direction. For direct visualization, a CCD imaging system (not shown in Fig. 4.2) is introduced to capture pictures and videos from the top side for post-processing.

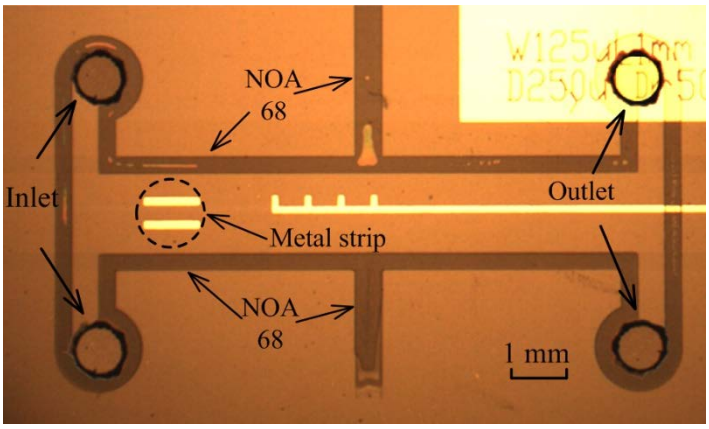

Fig. 4.3 Microscope image of the fabricated device: two metal strips are fabricated on the bottom, a glass with four holes is used as the top.

4.3.2 Device fabrication

The device fabrication part includes two sections: chromium strips (the microheater) fabrication and the microfluidic chip bonding. More details of the device fabrication can be found in Chapter 3. The fabricated device is shown in Fig. 4.3. In the microscope image, details of the microfluidic chip can be found: two metal strips work as the heater, a metal ruler for measurement, four holes on the top act as the inlets and outlets. Metal tubes will be used to connect the chip to the external pump.

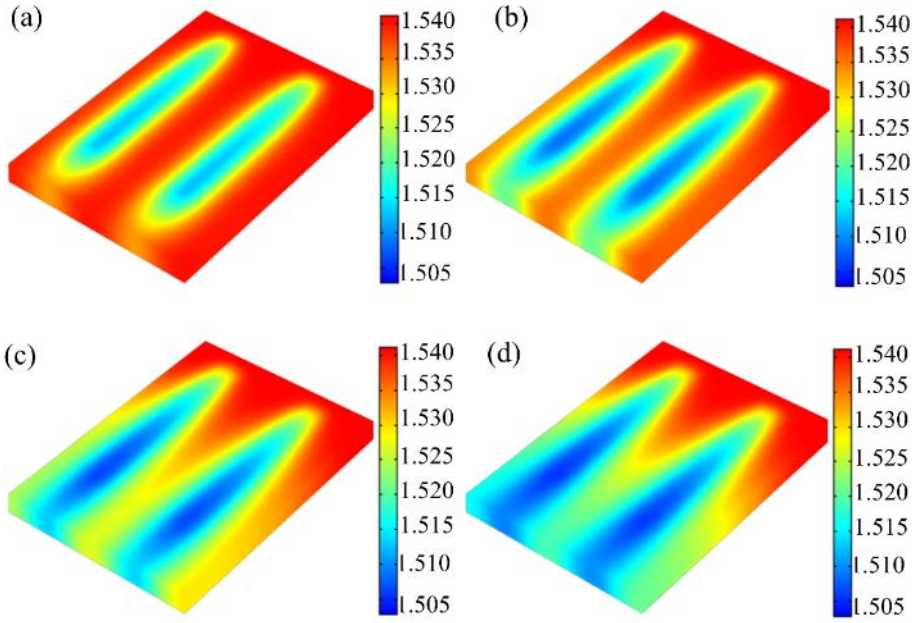

Fig. 4.4 Dynamic simulation of the evolution of the RI gradient inside the microchamber after the pump laser is turned on. The flow velocity is v = 6.17 mm/s and the net pump laser intensity is P_s= 0.31 W/mm^2. (a) At 25 ms, the flowing liquid close to the metal strips is heated up first. (b) After 50 ms, the RI along the vertical direction becomes uniform. (c) At 100 ms, a tongue-shaped RI profile is formed between the two strips. (d) At 200 ms, the RI profile becomes stable.

4.4 Simulated and experimental results

4.4.1 Simulated and measured RI gradients

(1) Comparison of the simulated and measured RI profile

The RI gradient profiles should be examined before considering the focusing effect. First, a three-dimensional (3D) computational fluidic dynamics (CFD) simulation is conducted to investigate the evolution of the RI profile inside the microchamber (see Fig. 4.4). In the simulation model, it takes the exact dimension of the design. And to simplify the calculation, the two metal strips are set as two heaters with a power of P_s. Then the calculated temperature profile is converted to

a refractive index gradient by using the thermo-optics coefficient of the liquid. It can be seen that it takes about 200 ms to establish a stable RI profile. More results of simulation and measurement are exemplified in Fig. 4.5. From the 2D RI profile in Fig. 4.5 a, it is seen that when the cool liquid flows through the hot strips, a RI gradient field is generated, especially at the entrance part between the two strips. The RI profile exhibits clearly curved equi-RI lines, as expected from Fig. 4.5c. The RI ranges from 1.50 to 1.54 ($\Delta n = 0.04$) when the temperature is changed from 25 ^{o}C to about 85 ^{o}C. In the 3D plot in Fig. 4.5b, it is seen that the RI has little change along the vertical direction. This suggests that the ray tracing simulation can be conducted in 2D, rather than 3D. Fig. 4.5(c) shows the RI profile measured by using the rhodamine B fluorescence. It looks very similar to the simulated field in Fig. 4.5(a). The RI distributions along three observation lines P1, P2 and P3 are plotted in Fig. 4.5(d). They all follow closely the square-law parabolic function.

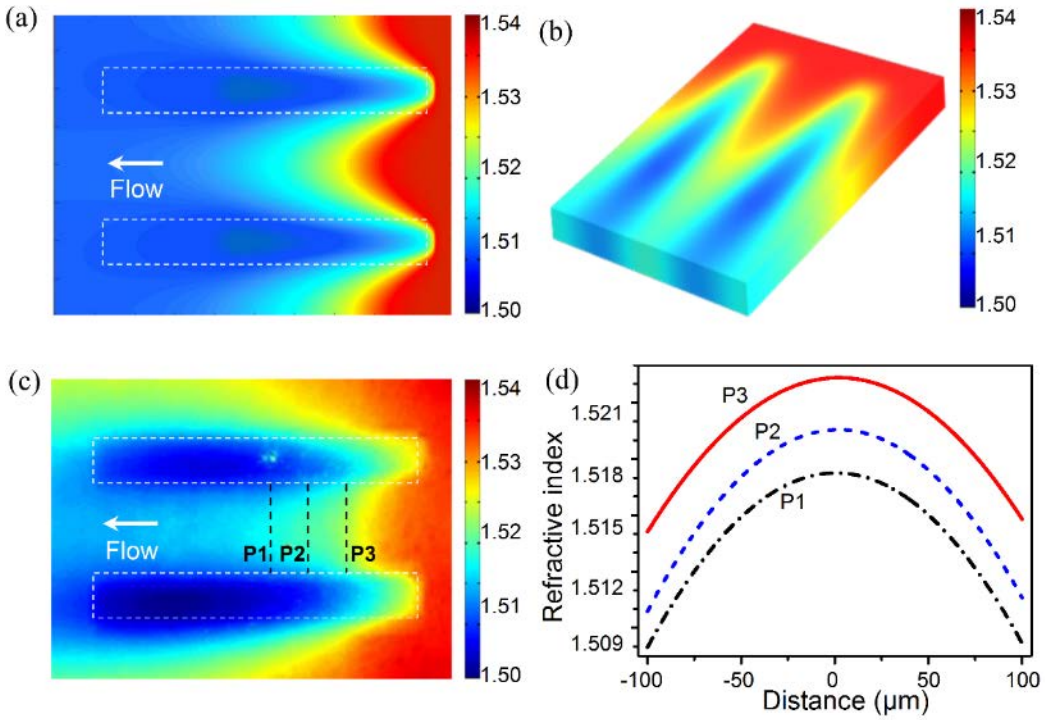

Fig. 4.5 Simulation and measurement of the RI profile at the flow velocity v = 6.17 mm/s. The simulated (a) two-dimensional and (b) three-dimensional RI profiles, the pump laser intensity in simulation P_s = 0.31 W/mm^2. (c) Measured RI profile as determined by the temperature dependency of rhodamine B fluorescence, the pump laser intensity in experiment P_i = 0.60 W/mm^2. (d) The RI distributions along three observation lines, which follow closely the square-law parabolic function. The white dashed rectangles in (a) and (c) represent the positions of the chromium strips. It is noted that the difference between P_i and P_s is due to the partial absorption of the laser energy by the metal strips, with an absorption efficiency of 51.7%.

(2) Temperature measurement inside the microchannel

Direct measurement of the temperature field in the microchamber is conducted by the use of the temperature dependency of rhodamine B fluorescence [71]. It includes two steps. The first step is to determine the empirical expression of the temperature as a function of the fluorescence intensity by polynomial fitting. In the second step, the unknown temperature is calculated using the obtained empirical expression once the fluorescence intensity is measured. More details are presented below.

In the first step, the fluorescence intensities at different temperatures are tested. Then, all the fluorescence intensities are normalized to that at 25°C. The measured relationship is plotted in Fig. 4.6. As can be seen that the fluorescence intensity decreases gradually with the increase of temperature. The dependency can be fitted by

$$T = 3.679I^3 - 11.84I^2 - 109.1I + 109.7 \quad (4.4)$$

where T is the temperature and I is the normalized fluorescence intensity.

In the second step, when the fluorescence intensity of the same rhodamine B solution is measured, it is normalized with respect to the fluorescence intensity at 25 °C, the obtained value is then substituted into Eq. (4.4) to get the temperature.

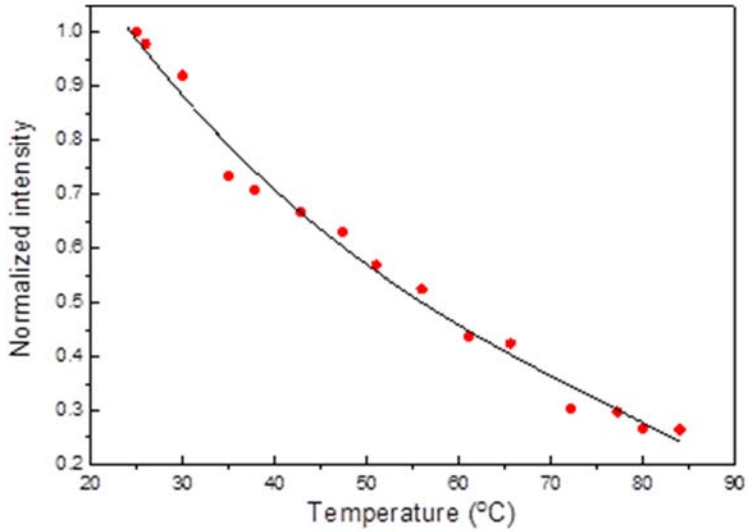

Fig. 4.6 Normalized fluorescence intensity of the rhodamine B solution versus temperature.

(3) Measurement of thermo-optic coefficient of benzyl alcohol

To determine the thermo-optic coefficient (TOC) of benzyl alcohol, we conducted another experiment using the Fresnel reflection method [72]. The working principle is illustrated in Fig. 4.7. A broadband light (central wavelength 1550 nm,

bandwidth 20 nm) from a light emitting diode (LED) enters port 1 of an optical circulator and goes out from port 2, which is connected to a single-mode optical fiber (Corning SMF-28e). The other end of the fiber is cleaved and immerged into the liquid sample, whose temperature is controlled by a water bath and is monitored by a thermometer. When the light hits the fiber/liquid interface (see the inset of Fig. 4.7), it undergoes a Fresnel reflection under normal incidence. The reflected light goes back to port 2 of the optical circulator and then passes to port 3, whose power is measured by an optical power meter.

The Fresnel reflection at the fiber/liquid interface is given by

$$R = \left(\frac{n_f - n_1}{n_f + n_1} \right)^2 \tag{4.5}$$

here n_f is the refractive index of optical fiber and n_1 is that of liquid sample.

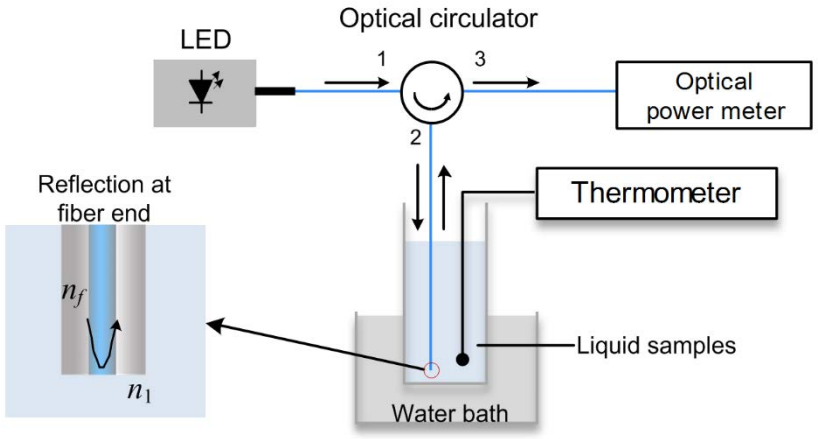

Fig. 4.7 Schematic of the Fresnel reflection method for refractive index measurement.

To offset the influence of fiber connection and temperature-dependence of fiber refractive index, we first used the air as the sample and measured the reflected power at different temperatures, and then used these data as the reference. The processed refractive index of benzyl alcohol is plotted in Fig. 4.8. Every data point

represents 5 measurements, and the error bars indicate the standard deviation of 5 measurements. The linear fitting of data points in Fig. 4.8 is

$$n(T) = -5.079\times10^{-4}(T-25)+1.5389 \qquad (4.6)$$

From the slope of linear fit, the thermal-optics coefficient of benzyl alcohol is $(-5.079 \pm 0.059) \times 10^{-4}\ ^{o}C^{-1}$

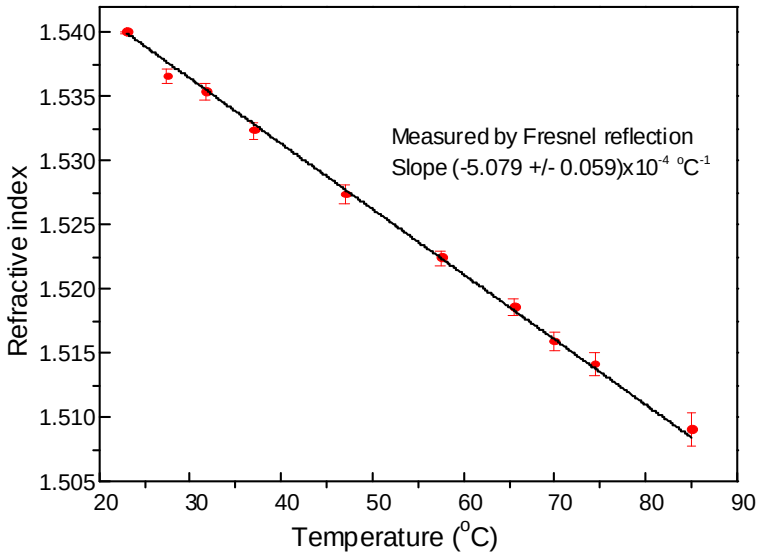

Fig. 4.8 Refractive index of benzyl alcohol versus temperature by the Fresnel reflection method

4.4.2 Experimental analysis of focusing performance

(1) Tuning of focusing states

Fig. 4.9 demonstrates different focusing states as observed in the experiment. To visualize the light path, the benzyl alcohol solution is added with a bit of rhodamine B dye, which absorbs 532 nm light and emits yellow fluorescence for the CCD imaging. In the initial state (i.e., the pump light is turned off), the probe

light is a parallel beam with the width of about 250 μm (see Fig. 4.9a1). After the pump laser is turned on, the parallel input probe light starts to be focused, and the focal spot is moved from right to left with the increase of the pump intensity (see Fig. 4.9(a2 – a4)). A minimum focal length of 1.3 mm is obtained under the conditions of the flow velocity v = 2.06 mm/s and the pump intensity P_i = 0.60 W/mm^2. Further increase of the pump intensity would cause an unstable flow and thus deteriorate the focusing effect. The focusing spots in Fig. 4.9(a2 – a4) are all on the optical axis as a result of symmetric irradiation of the two strips. However, when the pump spot is offset to create an asymmetric RI profile, the probe light beam can be deflected to form an off-axis focusing as shown in Fig. 4.9(a5).

The normalized intensity distributions along four observation lines L1 to L4 of Fig. 4.9(a4) are plotted in Fig. 4.9(b). They are fitted to the Gaussian function. It is seen that the peak intensity at the center is increased sharply and the curve shape is better fitted to the Gaussian function when the observation line moves closer to the focal spot.

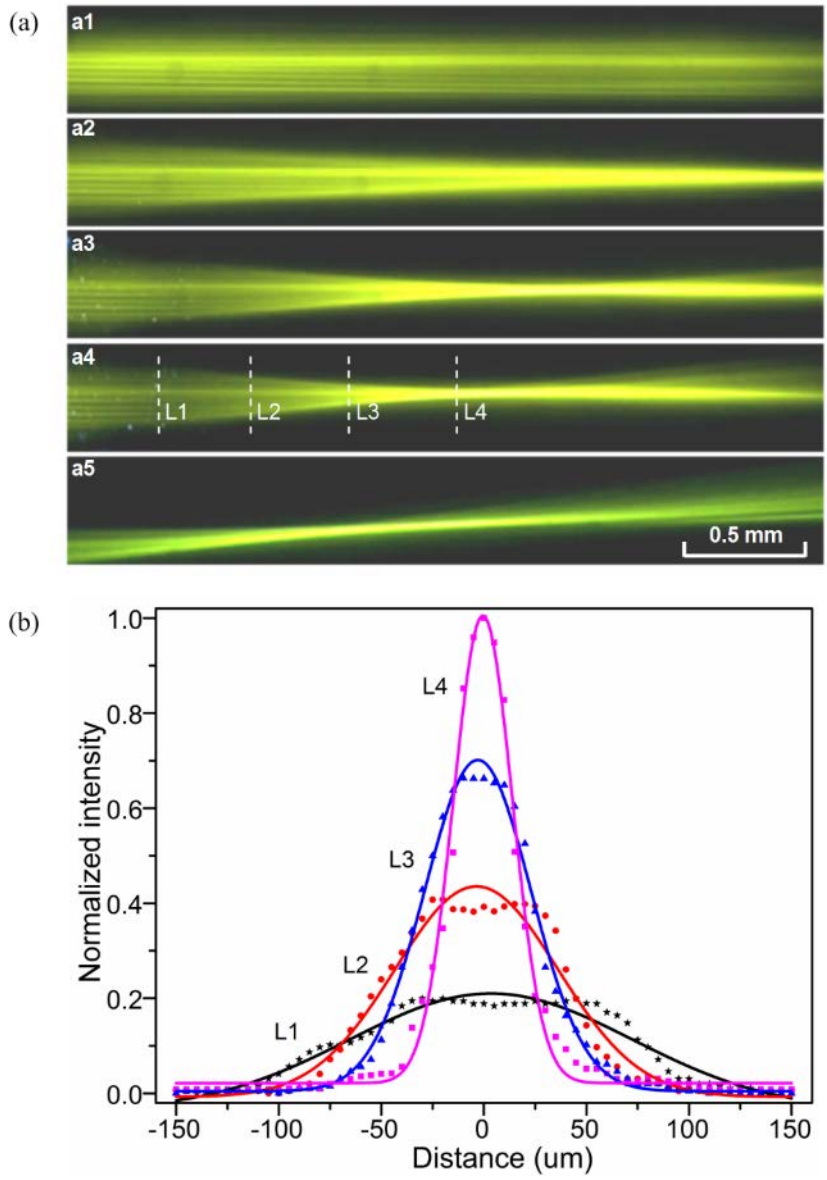

Fig. 4.9 Experiments of the tunable optofluidic lens. (a) Different focal states: (a1) the initial state when the pump laser is off; (a2) focusing under laser power of 0.3 W/mm^2; (a3) increased focusing under 0.5 W/mm^2; (a4) further increased focusing under 0.6 W/mm^2, obtaining the shortest focal length of 1.3 mm; (a5) deflection of the focused beam when the pump laser spot is moved away from the center to generate an asymmetric refractive index. (b) Normalized intensity distributions along the observation lines L1–L4. The solid curves are fitted to the Gaussian function. It is seen that the peak intensity goes higher and the curve shape approaches closer to the Gaussian function when the observation line is moved closer to the focal spot.

(2) Size of focused spot

To experimentally demonstrate the ray tracing, Rhodamine B dye is added into the solution. The dye absorbs green light and emits yellow fluorescence for visualization of the ray path. However, the fluorescence often causes an enlargement of the focal spot size due to the scattering, especially when the green probe laser is strong. For instance, the size of the focal spot is about 15.2 μm when the coupled probe laser is P_{probe} = 1.0 mW (see Fig. 4.10a), and it is reduced to 9.8 μm when the coupled laser is very weak to let only the focal spot visible (see Fig. 4.10b). The size of 9.8 μm is about two times of the theoretical limit 5.5 μm. Take the enlargement of fluorescence imaging into consideration, the above results are acceptable.

In simulation, the focusing properties are examined. First, a CFD (computational fluidic dynamics) programme is used to calculated the temperature profile and the corresponding refractive index profile. Then, a ray tracing simulaiton is conducted to analyze the focusing performance and the focal length. Fig. 4.11 shows the ray tracing results for two pump laser intensities P_s = 0.31 W/mm^2 and P_s = 0.12 W/mm^2, which produces the focal lengths f = 1.478 mm and f = 3.25 mm, respectively. From Fig. 4.11, it can be seen that both result in almost perfect focusing, or in the other words, aberration-free focusing. Further simulation shows that such an aberration-free focusing can be maintained during the whole tuning process of the focal lengths. This is because the refractive index distribution follows the square-law parabolic function in any cross section along the optical axis (see Eq. (4.1b).

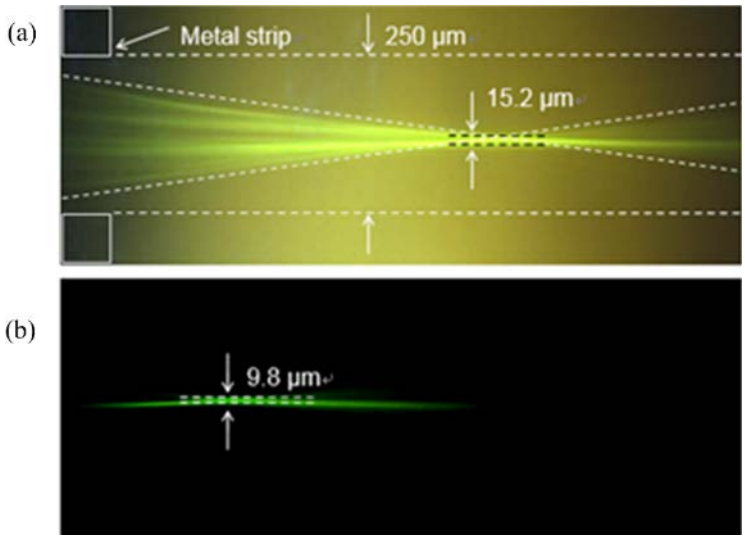

Fig. 4.10 Analysis of the focal spot size. (a) Ray tracing when the probe laser power P_{probe} = 1.0 mW, for which the focal spot size is 15.2 μm. (b) The focal spot is redueced to 9.8 μm when the probe laser power is tuned to very weak. Other condictions are v = 2.06 mm/s, P_i = 0.6 W/mm^2, f = 1.30 mm.

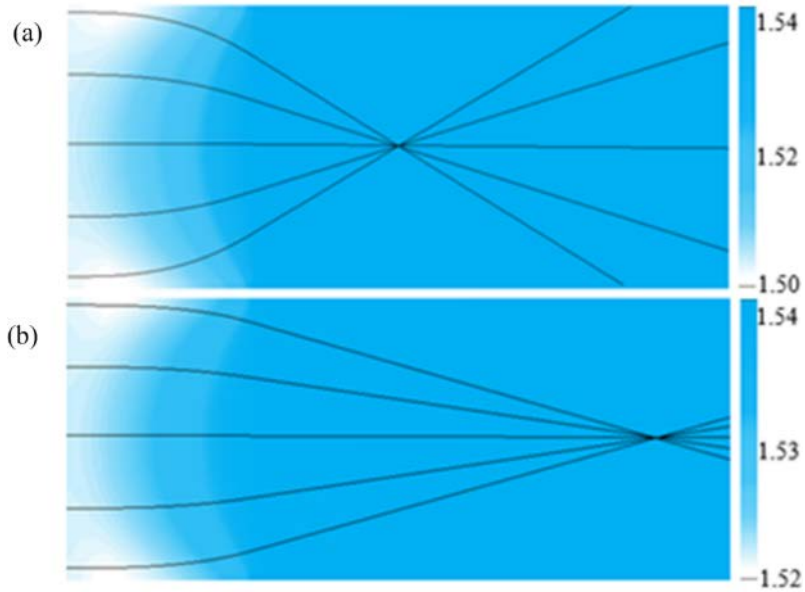

Fig. 4.11 Ray tracing simulation. (a) P_s = 0.31 W/mm^2, f = 1.478 mm. (b) P_s = 0.12 W/mm^2, f = 3.25 mm. Both exhibit almost perfect focusing. For simulation, the flow velocity is always v = 6.17 mm/s.

(3) Dependences of focal length on pump laser intensity and flow velocity

It is easy to understand that the focal length is dependent on two factors: the flow velocity and the pump laser intensity. To find out the empirical relationships, two sets of experiments are conducted.

Table 4.1 Dependences of the focal length on pump laser intensity with constant flow velocity. Pump laser intensity: P_i (W/mm^2); Flow velocity: v (mm/s); Focal length: f (mm).

P_i / v / f	0.394	0.427	0.453	0.475	0.495	0.520	0.542	0.554	0.562	0.570	0.582	0.591	0.599
6.170	3.299	2.860	2.476	2.309	2.129	1.968	1.819	1.744	1.693	1.630	1.563	1.498	1.477
2.060	2.899	2.442	2.243	2.047	1.855	1.767	1.624	1.531	1.503	1.466	1.412	1.359	1.330

Table 4.2 Dependence of the focal length on flow velocity under constant pump laser intensity. Pump laser intensity: P_i (W/mm^2); Flow velocity: v (mm/s); Focal length: f (mm).

v / P_i / f	2.058	6.172	10.288	12.345
0.520	1.764	1.895	2.159	2.553
0.600	1.311	1.475	1.786	2.117

First, the flow velocity is maintained at v_1 = 2.06 mm/s or v_2 = 6.17 mm/s, whereas the pump laser intensity is varied gradually from very low to the maximum 0.6 W/mm^2. Table 4.1 lists the experimental measurements. And the results with the error bars are plotted in Fig. 4.12(a). Each data point represents five measurements. When the pump laser intensity is increased from about 0.4 W/mm^2 to 0.6 W/mm^2, the focal lengths is decreased from about 2.9 mm to 1.3 mm for v_1 = 2.06 mm/s, and 3.3 mm to 1.5 mm for v_2 = 6.17 mm/s. It is found that the two curves can be well fitted by the second-order polynomial function $F(P_i) = a_0 + a_1 P_i + a_2 P_i^2$, where F is the focal length (in mm) and P_i is the pump

laser intensity (in W/mm^2). For the coefficients, there are a_0 = 10.479, a_1 =-27.368, and a_2 = 20.242 for the case of v_1 = 2.06 mm/s, and a_0 = 12.449, a_1 = -32.905 and a_2 = 24.390 for the case of v_2 = 6.17 mm/s.

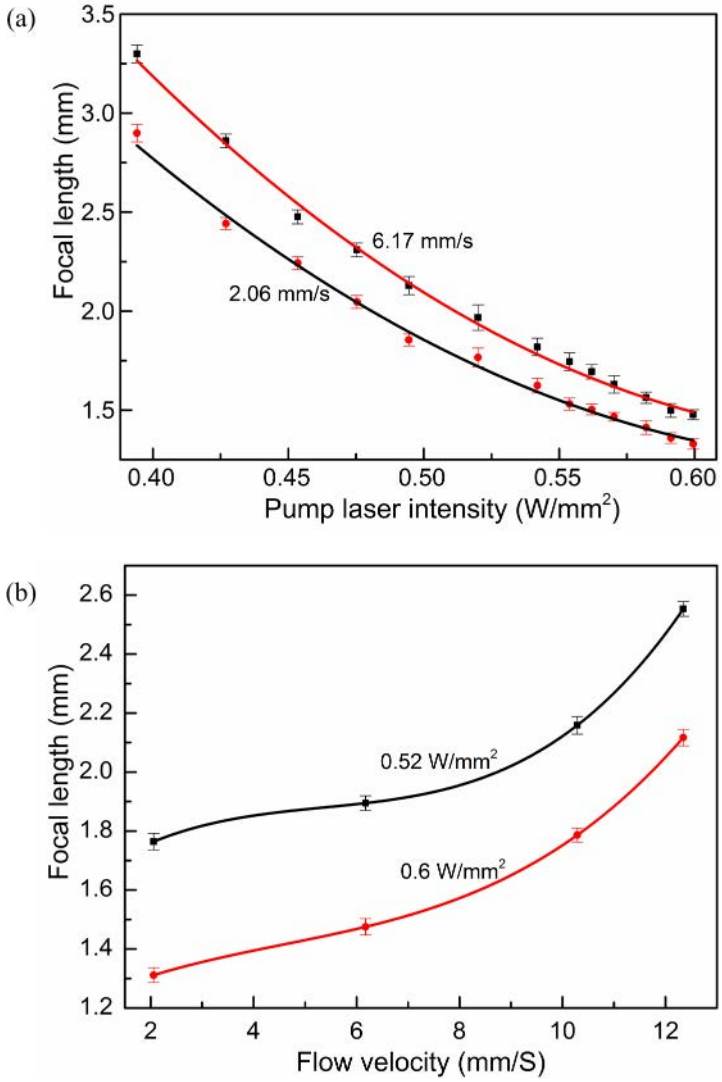

Fig. 4.12 Measured tunability of the optofluidic lens. (a) Focal length as a function of the pump laser power under two different flow velocities. The solid curves are the fitted second-order polynomial functions. (b) Focal length as a function of the flow velocity with two constant pump powers. The solid curves are the fitted third-order polynomial functions.

Similarly, the focal length as a function of the flow velocity is measured at the pump laser intensity of 0.52 W/mm^2 or 0.6 W/mm^2 as displayed in Table 4.2. And the results are plotted in Fig. 4.12(b). The focal length goes longer when the flow is moving faster, and it can be well fitted by the third-order polynomial

function $F(v) = b_0 + b_1 v + b_2 v^2 + b_3 v^3$ (F in mm and v in mm/s). The coefficients are b_0 = 1.535, b_1 = 0.1577, b_2 = -0.0262 and b_3 = 1.630×10^{-3} for the case of P_i = 0.5 W/mm^2, and b_0 = 1.165, b_1 = 0.09333, b_2 = -0.01263 and b_3 = 9.170×10^{-4} for the case of P_i = 0.6 W/mm^2. Although the experimental data are not sufficient to derive the two-variable empirical function $F(P_i, v)$, the empirical relationships make it feasible for the real-time tuning of the focal length.

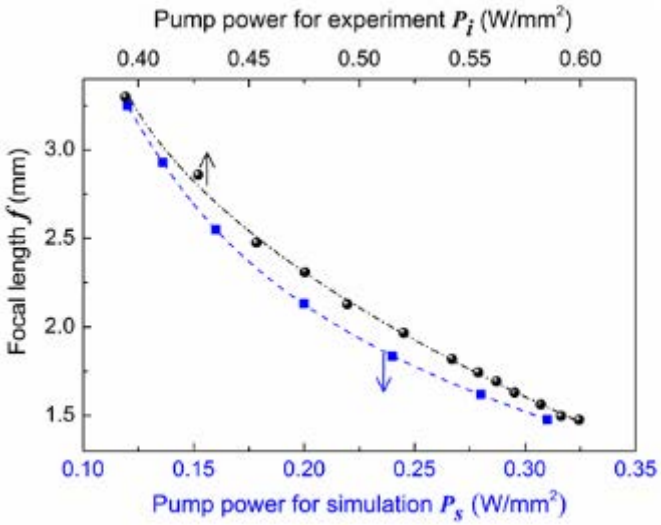

Fig. 4.13 Comparison between simulated and experimental results, v = 6.17 mm/s, the top and bottom x axes are the experimental and simulated pump power intensities, respectively. After a conversion using the absorption efficiency, the two curves match well with each other.

(4) Comparison of simulated and experimental results

To verify the empirical relationship, we further simulated the relationship between the pump laser intensity and the focal length and then compared with the experimental results. Fig. 4.13 displays both the simulated and experimental relationships between the focal length and the pump power intensity. Since only a portion of the laser energy is absorbed by the metal strips and converted into the heat energy, the pump power intensity P_i of the experiment is different from the net intensity P_s used in the simulation. Here the ratio between P_s/P_i is defined as

the efficiency of the laser-induced thermal lens. As only a portion of the laser power has been converted into thermal energy, the efficiency should be below 100%. For Example, the absorption efficiency is P_s/P_i = 51.7% for P_i = 0.60 W/mm^2. After the conversion of the absorption efficiency, the two curves in Fig. 4.13 match roughly with each other.

4.5 Discussions

4.5.1 Influence of device parameters

The choices of device parameters have influences on different aspects of the lens performance. (1) Metal strip width: the metal strips of the working device are chosen to be 125 μm wide. As the sources of heat energy, the metal strips should have the width of 0 μm in the ideal case. But narrow strips cause low absorption to the pump laser, whereas too wide strips would disturb the heat field. The width of 125 μm is found be to a suitable choice for our experiments. (2) Separation of metal strips: it is 250 μm in the working device. A larger separation leads to a longer time to stabilize the temperature profile and also causes a longer focal length as the refractive index gradient is weaken (since the maximum temperature difference is determined by the boiling point of the solution). But a smaller separation of the two strips leads to a smaller aperture size and thus a large focus spot since the focus spot size d is given by $d = 2\lambda f / D$, here f is the focal length, λ is the wavelength and D is the aperture diameter. The separation of 250 μm makes a good trade-off between the response time and the spot size.

4.5.2 Merits of thermal lens

This work is the first demonstration of the laser-induced thermal lens for in-plane optofluidic focusing. One of the special parts is the use of simple design of metal strips to generate the thermal lenses in a running fluid. From the study above, it can be summarized that this 2D-GRIN lens has intrinsic benefits as compared with the other reported optofluidic lenses [13]:

(1) **Fast tuning speed**: the thermal gradient can be generated as fast as 10 μs – 10 ms if the pump laser is a high-power pulsed laser. In this work, it takes 200 ms due to the use of low-power continuous pump laser. However, it is already one order of magnitude faster than the typically 1 s in the reported flow-reconfiguring methods [13].

(2) **Strong thermal/RI gradients**: a tightly focused pump laser can generate a large temperature difference in a microscale space (e.g., 3 K/μm [73]). As a result, it can generate a large RI gradient (e.g., 1.8 RIU/mm, RIU for refractive index unit).

(3) **Aberration-free focusing**: the ray tracing simulation shows that the rays can be focused to a singular point for laser-induced RI gradients. It is also reasonably verified by the focal spot size test, which measures the focal spot of 9.8 μm, about two times of the theoretical value 5.5. Considering the enlargement of the spot size by the fluorescence dye, it is reasonable to say that the measured focal spot size of 9.8 μm is close to the theoretical value of 5.5 μm. Or in the other words, the focusing effect of the thermal lens is almost aberration free. This is different from the usually strong aberration in the reported liquid lenses.

(4) **Use of homogeneous fluid**: The focusing effect can be generated in a homogeneous liquid, as long as it has large thermo-optic coefficient and low thermal conductivity [19]. This is different from many reported liquid lenses that make use of two (or more) types of liquids [13]. Therefore, the liquid can be reused or recirculated.

(5) **"Remote" control**: the pump laser device has no physical contact with microchip parts.

(6) **Easy relocation**: The thermal lens can be formed at and then relocated to any point of interest by changing the irradiation spot.

(7) **Low pump laser power**: the use of metal absorption significantly lowers the required pump power, especially when compared with the thermal lenses that relies on the absorption of fluid itself [74].

(8) **Easy integration**: The in-plane arrangement of device and the capability of in-plane beam focusing make it easy to integrate into many optofluidic systems.

4.5.3 Limitations of thermal lens

Nevertheless, the 2D-GRIN lens design has its own limitations.

(1) **Complexity**: the analysis and simulation are complicated as it has to consider the coupling effects of fluidic, thermal and optical properties. Although empirical functions can be determined under specific conditions (as stated in subsection 4.3), it is still difficult to get a closed-form analytical expression of the focal length on the pump laser intensity, the flow velocity and the microchip geometry.

(2) **Limited *f*-number**: here the *f*-number is the ratio between the focal length and

the aperture diameter. Since the edge-to-edge separation between the two chromium strips are 250 μm, the minimum focal length 1.3 mm corresponds to the minimum *f*-number of 5.2. Further reduction of the *f*-number requires ever stronger RI gradient and may need to find other liquid materials to replace benzyl alcohol. Although these limitations affect the device performance, this optofluidic tunable lens design is already suitable for many applications like optofluidic light sources, trapping and single particle detection.

4.6 Summary

This chapter has presented a new design of optofluidic tunable lens that has a two-dimensional gradient distribution of RI. This is accomplished by using a continuous pump laser to irradiate two metal strips to generate a thermal gradient in a thin liquid layer. For the theoretical verification, a CFD simulation has been conducted to analyze the evolution process of the RI profile upon heating. For experimental investigation, tuning of the in-plane focusing states has been demonstrated by varying the pump laser intensity and the flow velocity. Compared with the previously-reported tunable liquid lenses, the design of this work is distinctive and advantageous in many aspects such as tuning speed, aberration-free focusing, remote control and easy integration. In addition, this design utilizes only one type of liquid, which may be especially useful for some applications that can only use one liquid, or need to reuse the precious liquid. Nevertheless, this lens still requires a continuous flow of the liquid and thus the external pump, which may not be convenient to some applications. To avoid this problem, the next two chapters will present new DEP-actuated liquid lenses, which work at static flow (do not require the continuous external pumping).

Chapter 5 DEP-Actuated Optofluidic Lens Using Single Liquid-Air Interface

This work is reproduced in part from "Dielectrophoresis-actuated in-plane optofluidic lens with tunability of focal length from negative to positive" *Optics Express*, 26(6), 6532-6541 (2018) by Q.M Chen, T.H Li, Y.J Zhu, W.X Yu and X.M Zhang, with the permission of The Optical Society of America.

The tunable thermal lens in the previous chapter requires a moving flow and the external pump. This chapter will present a new type of lens that works at static flow. It is an in-plane optofluidic tunable lens actuated by dielectrophoresis (DEP), which drives the liquid with higher permittivity to the strong electric field. DEP has been widely used in fluidic actuation and particle manipulation in microfluidics. Here DEP force is utilized to continuously deform a liquid-air interface for light manipulation in a microfluidic chip. It demonstrates the divergence, collimation and focusing effect. The longitudinal spherical aberration (LSA) has also been effectively suppressed by the edge pinning effect. This chapter includes introduction, working principle, device design, simulation and experimental analysis.

5.1 Dielectrophoresis

When a charged particle is placed in an electric field, the particle bears a force, which is called electrostatic force. If the particle is neutral (dielectric) or charge balance, the net electrostatic force is zero. While such a dielectric is subjected to a nonuniform electric field, it will experience a force called dielectrophoretic force[36]. Dielectrophoresis (DEP) appears when a neutral particle is placed in an inhomogeneous electric field. In addition, DEP also happens in dielectric fluid,

where the DEP force drives the liquid with a higher permittivity to a stronger electric field area originally occupied by liquid with a lower permittivity. DEP has been widely used in microfluidic applications such as particle manipulation, transportation, separation and sorting. Another interested application of DEP is to modify the interfaces of liquid lenses [36]. This kind of adaptive lens has some inherited merits and finds applications in imaging optics, beam steeling and optical modulator, etc.

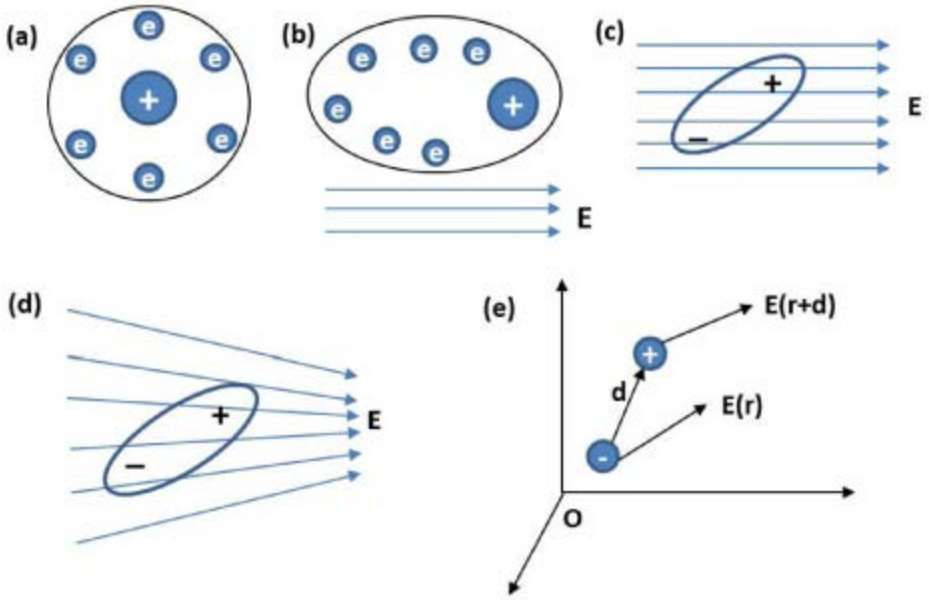

Fig. 5.1 Dielectrophoretic force [36]. (a) Inside structure of the neutral particle: the positive charged core is surrounded by negative charged electron cloud. (b) A dipole moment is induced by the external field. (c) A dielectric particle is polarized in an uniform electric field. (d) A dielectric particle is placed in an inhomogeneous electric field. (e) Cartesian coordinate is used to deduce the dielectrophoretic force.

5.1.1 Dielectrophoretic force on dielectric particle

The electrostatic force of a charged particle can be described by [36]

$$F_e = QE \tag{5.1}$$

where Q is net charge of the particle and E is the electric field. For a neutral

dielectric particle, Q is zero as well as the electrostatic force. In a neutral particle, the positive core is surrounded by a negative electron cloud, as shown in Fig. 5.1a. This particle is charged balance because its positive charge $+Q$ equals to negative charge $-Q$. If the particle is placed in a uniform electric filed, the necleus and the electrons will be separated and pushed away in two opposite directions, as shown in Fig. 5.1b. As a result, the particle is polarized and a dipole moment is induced. According to Eq (5.1), the electrostatic force of the positive charge and negative charge is equal but with opposite direction, resulting force balance in the particle. The induced dipole moment can be simplified into point-charge model as shown in Fig. 5.1c. The two point-charges is separated by a displacement of d. The induced dipole moment is [36]:

$$P = Qd \tag{5.2}$$

where d is the displacement vector pointing from $-Q$ to $+Q$. Because of the induced dipole moment, the particle will be realigned parallel to the external electric field. There are also some naturally polarized molecules such as water, in which the positive charges and the negative charges do not completely overlap, resulting in a permanent dipole moment. If the electric field is nonuniform, the balance state in Fig. 5.1c will be broken. Fig. 5.1d shows that a particle is placed in an inhomogeneous electric field, where the $+Q$ and $-Q$ see different electric field. As shown in Fig. 5.1e, a Cartesian coordinate is used to describe the electric force of the dipole moment. The net force of the dielectric particle can be expressed as [36]:

$$f_e = Q\left[E\left(r+d\right) - E\left(r\right)\right] \tag{5.3}$$

where $E(r+d)$ is not equal to $E(r)$, resulting in a net force on the dipole。It can be

rewritten by $P=dQ$ as following [36]

$$f_e = P \cdot \nabla E \tag{5.4}$$

where $\nabla E = [E(r+d) - E(d)]/d$ represents the gradient of the electric field. The above equation demonstrates that a nonuniform electric field exerts a net force on the dielectric particle. For a bulky object, the polarization force density is used to describe the force intensity. For example, in a homogeneous particle, the dipole density is Np. As a result, the dipole moment density is $P = N_p \cdot p$. Thus, the electric force density can be written as [36]:

$$F = P \cdot \nabla E \tag{5.5}$$

where F is called Kelvin polarization force density. For a liner dielectric material, the polarization density is [36]:

$$P = \varepsilon_0 \chi_e E = \varepsilon_0 (\varepsilon_r - 1) E \tag{5.6}$$

where χ_e is the susceptibility of the material; ε_0 and ε_r are the permittivity of free space and the dielectric material, respectively. When the dielectric material is placed in a medium with a dielectric constant of ε_m, the Kelvin polarization force can be rewritten as [36]:

$$F = \varepsilon_0 (\varepsilon_d - \varepsilon_m) E \cdot \nabla E \tag{5.7}$$

where $E \cdot \nabla E$ can be further simplified using $E \cdot \nabla E = (\nabla \times E) \times E + \frac{1}{2}\nabla(E \cdot E) = 0 \times E + \frac{1}{2}\nabla E^2$. Thus, the Kelvin polarization force becomes [36]:

$$F = \frac{1}{2}\varepsilon_0 (\varepsilon_d - \varepsilon_m)\nabla E^2 \tag{5.8}$$

the above equation describes the Kelvin force of a unit dielectric particle surrounding by a medium with a dielectric constant of ε_m. It is noticed that the force depends on the dielectric constant difference as well as the electric field gradient. In addition, the direction of the force is determined by whether the permittivity of the dielectric material is higher or smaller than that of the surrounding medium.

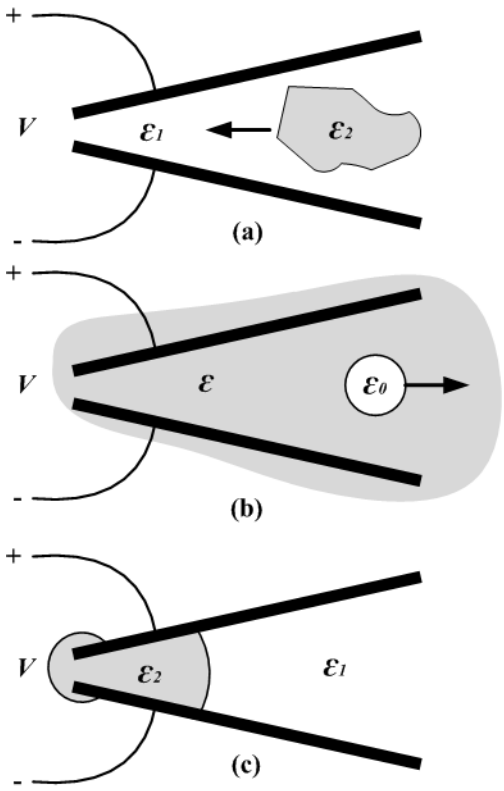

Fig. 5.2 Liquid dielectrophoresis phenomenology [79]: (a) Dielectric liquid drawn into strong electric field, $\varepsilon_2 > \varepsilon_1$. (b) Bubble repelled from strong electric field, $\varepsilon > \varepsilon_0$. (c) Control liquid profile with surface parallel to applied electric field, $\varepsilon_2 > \varepsilon_1$.

5.1.2 Dielectrophoretic force on dielectric liquid

DEP force has also been widely used in microfluidic manipulation. Through the electric field induced dielectrophoretic force and interfacial tension, the fluidic

interface can be dynamically manipulated, resulting in reconfigurable optofluidic devices [36]. Recently, a variety of dielectrophoresis actuated optofluidic devices, such as liquid lens [75], optical waveguide [76], beam steering [77] and grating [78] have been demonstrated.

The phenomenon of the liquid DEP is that: dielectric liquid (with higher permittivity) in a non-uniform electric field tends to collect in regions of high electric field intensity [79]. As shown in Fig. 5.2a, DEP force pulls the droplet to the strong electric field. It can also repel the bubble within the liquid from strong electric field due to the lower permittivity of the bubble, see Fig. 5.2b. It can also be used to change the shape of liquid due to the deformability of liquid. In a strong electric field, the free surfaces of the liquid are approximately parallel to the electric field, as shown in Fig. 5.2c.

DEP has also been widely used to manipulated droplets in microfluidic chip. S.K Fan's group has done a great job in the digital manipulation of droplets using DEP, including transporting, splitting and merging of droplets. For instance, two parallel plates with electrodes were used to apply an DC voltage to manipulate dielectric droplet by DEP [80]. As shown in Fig. 5.3a, the droplet is pumped into the strong electric field area by DEP force. The splitting, transporting and merging of dielectric droplet have been demonstrated by using digital electrodes, as shown in Fig. 5.3b & c. A reconfigurable liquid core/liquid cladding waveguide was also demonstrated using DEP [76]. The schematic deign is shown in Fig. 5.4. Two liquids with different RIs are sandwiched by two parallel plates, on which ITO electrodes are coated. By applying a voltage across the plates, the liquid core (with higher RI and higher permittivity) is pumped into the liquid cladding, forming an

optical waveguide. Both static and moving optical waveguides were demonstrated using this DEP platform.

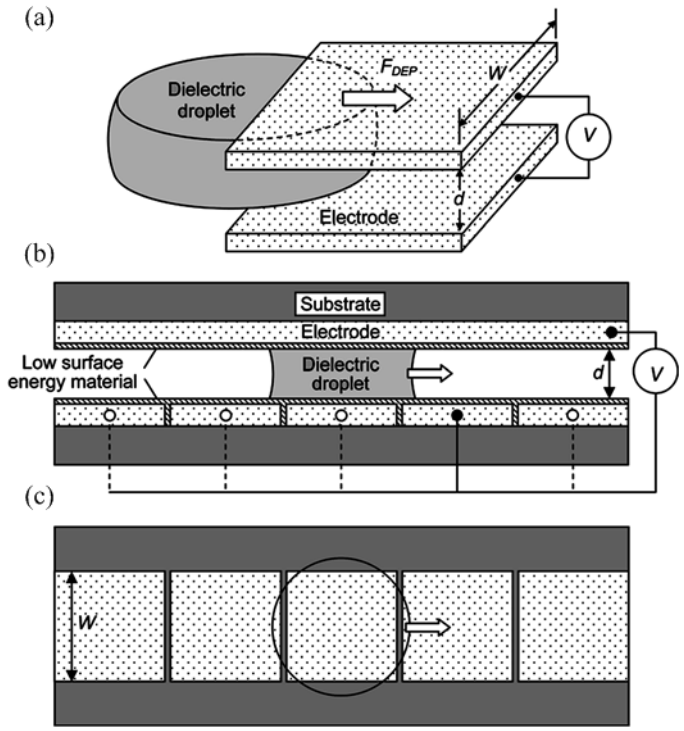

Fig. 5.3 DEP actuation of dielectric droplets [80]. (a) By applying voltage between parallel electrodes, a liquid dielectric droplet of a higher relative permittivity is pumped by DEP into the region of a lower relative permittivity. (b) Side view and (c) top view of the device.

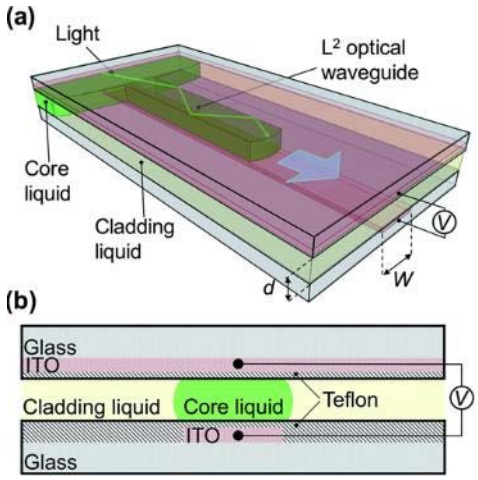

Fig. 5.4 L2 Optical waveguide based on a virtual microchannel constructed using DEP [76]. (a) Light guided in the core liquid with greater refractive index (n_{core} = 1.4341) and permittivity (ε_{core} = 39) activated between the plates by the DEP electric field into the region of cladding liquid with smaller refractive index ($n_{cladding}$ = 1.401) and permittivity ($\varepsilon_{cladding}$ = 2.5). (b) Cross section of the DEP-driven waveguide.

5.1.3 DEP-actuated in-plane optofluidic lens (single interface)

Two types of electrostatic force based optofluidic lenses have been demonstrated [75,81]. According to the working principle, they can be classified into electrowetting lens [81] and dielectrophoresis (DEP) lens [36]. In the electrowetting lens, an external voltage is applied to modify the contact angle between the liquid and the lateral sidewall of the liquid container, thereby changing the droplet curvature as well as the focal length. Real-time modulation of the focal length can be achieved by changing the applied voltage. DEP exerts a net force on the fluidic interface to drive the liquid of greater permittivity into the strong electric field region originally occupied by the medium of smaller permittivity [76]. Most of the previous electric liquid lenses are out-of-plane lens, like conventional solid lens, the beams are manipulated in the direction perpendicular to the microfluidic substrate [13]. They have been used to replace the conventional solid lenses in some specific circumstances. But the poor compatibility of the out-of-plane lenses limits their application in microfluidic networks.

This chapter presents a tunable in-plane optofluidic lens by continuously tuning a silicone oil-air interface from concave to convex using the DEP force. Two parallel glasses are bonded firmly on two sides by NOA 81 (Norland Optical Adhesive 81) spacers, forming an open microfluidic channel. An ITO (indium tin oxide) strip and another unpatterned ITO layer are deposited on two glasses as the top and bottom electrodes. Initially, a capillary concave liquid-air interface is formed at the end of the open channel. Then the DEP force is enabled to continuously deform the interface (lens) from concave to convex.

5.2 Working principle

5.2.1 Schematic design and device fabrication

The schematic design of the reconfigurable DEP liquid lens is shown in Fig. 5.5. Two MgF_2 glasses are used as the top and bottom, which are bonded firmly by two NOA 81 strips, forming an open channel (length 10 mm, width 0.6 mm, height 55 μm). Silicone oil (n = 1.405) is chosen as the optical medium, which can be easily filled into the open channel by the capillary force. The cross-section view in Fig. 5.5(b) shows that an ITO strip (width 400 μm, thickness 100 nm) is deposited on the top glass as the anode and an ITO thin layer (thickness 100 nm) on the bottom glass as the ground. In the initial state, a concave interface (indicated by the dashed line in Fig. 5.5(a)) is formed at the end of the channel, resulting in a divergent lens. When a DC voltage is applied to the device, an electric field is generated in between the two glasses. According to the liquid dielectrophoresis, the DEP force drives the silicone oil ($\varepsilon_{silicone}$ = 2.5) into the air region. As a result, the liquid-air interface is deformed into a convex shape (blue liquid in Fig. 5.5(a)). The curvature of the interface can be continuously tuned by changing the applied voltage. To visualize the lensing effect, a collimated probe beam (waist diameter 400 μm) is coupled into the liquid layer from left to right (i.e., from air to liquid in Fig. 5.5(a)) using a pigtailed aspheric fiber collimator (CFS2-532-FC, beam divergence 1.75 mrad, Thorlabs).

The device is fabricated using the methods descripted in Chapter 3. In the microscope image of Fig. 5.6, it can be found that the device has an open channel. Two ends of the channel work as lens section and inlet, respectively. An ITO electrode is located at the center of the channel.

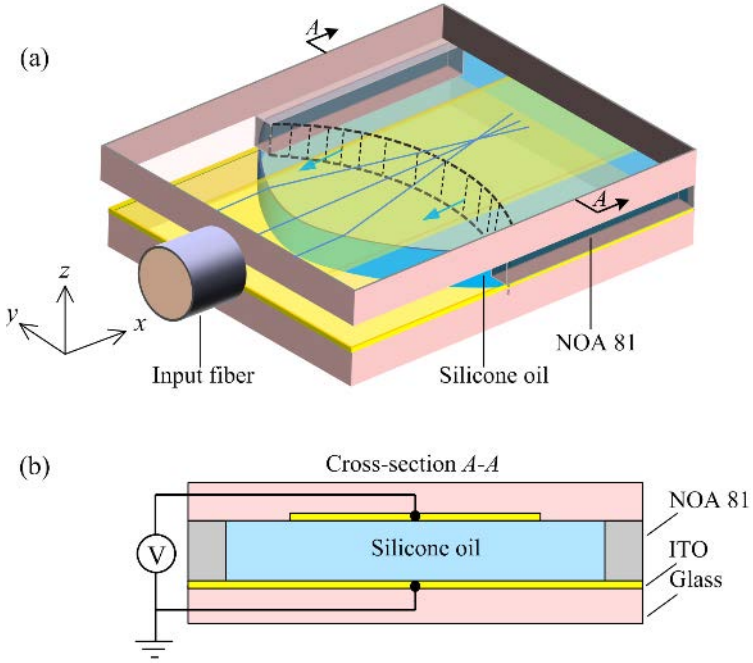

Fig. 5.5. Schematic design of the DEP lens. (a) 3D view, the DEP force drives the liquid-air interface from concave (dashed line: initial state) to convex. (b) Cross-sectional view of the lens, which has a top electrode (at the center of the channel) and a bottom electrode, the liquid layer is sandwiched by the two glasses bonded and spaced by two NOA 81 adhesive strips.

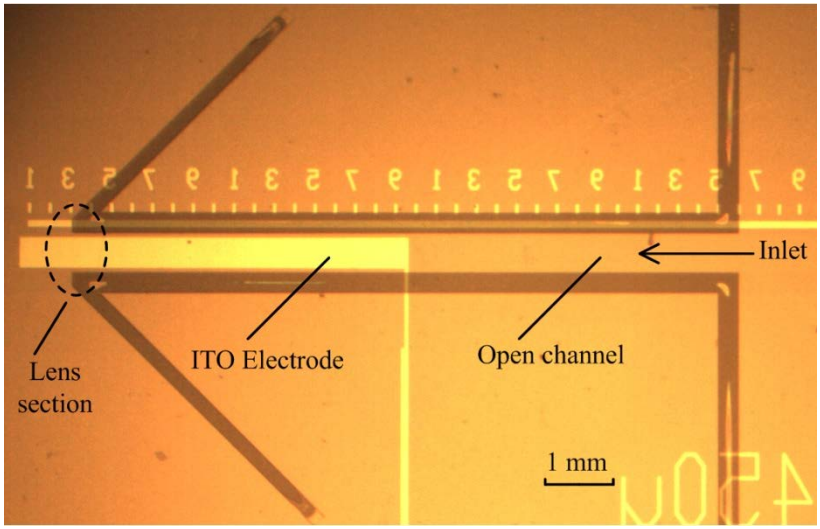

Fig. 5.6 Microscope image of the fabricated device: ITO electrode at the center of the channel, the left end of the channel is the lens section, and the right end of the channel is the inlet.

5.2.2 Theory of interface modulation

The DEP force exerted at the liquid-air interface between two parallel plates can be expressed as [76]

$$F_e = \frac{\varepsilon_0 (\varepsilon_L - 1) w}{2d} V^2 \tag{5.9}$$

where ε_0 is the permittivity of vacuum and ε_L is the relative permittivity of the liquid. And w is the width of the ITO strip and d is the gap between the two glasses. It is noted that the DEP force is dependent on the dielectric property of liquid and the applied voltage.

The pressure drop at the liquid-air interface can be described by the Laplace law [82]

$$\Delta P_0 = 2\gamma\kappa = \gamma\left(\frac{1}{R_{10}} + \frac{1}{R_{20}}\right) \tag{5.10}$$

here γ is the surface tension between silicone oil and air, and κ is the mean curvature of the liquid-air interface. R_{10} (in horizontal) and R_{20} (in vertical) are the principal curvature radii of a point at the interface. The liquid-air interface is assumed to be spherical, which will be validated by the experiment later. Initially, the capillary force in the microchip is balanced. When an external voltage is applied, it changes the curvature as well as the pressure difference. As the surface property of the top and bottom surfaces is constant, R_{20} keeps unchanged [82]. The pressure variation is

$$\Delta P_1 - \Delta P_0 = \gamma\left(\frac{1}{R_{11}} + \frac{1}{R_{20}}\right) - \gamma\left(\frac{1}{R_{10}} + \frac{1}{R_{20}}\right) = \gamma\left(\frac{1}{R_{11}} - \frac{1}{R_{10}}\right) \tag{5.11}$$

It implies that the pressure variation only depends on the horizontal curvature radius. Because the extra pressure difference is induced by the DEP force, they should be equivalent [79]. Thus

$$F = \left(\Delta P_1 - \Delta P_0\right) w_0 d_0 = F_e \tag{5.12}$$

where w_0 and d_0 are the width and height of the channel, respectively. Therefore, the curvature radius of the interface under new equilibrium can be calculated by Eqs. (5.9-5.12). In a spherical liquid-air interface, the focal length of the paraxial rays is described by

$$f = \frac{nR}{n-1} \tag{5.13}$$

here n is the refractive index of the liquid and R is the curvature radius of the interface. The light strikes on the interface from the air. In spherical lens, there is a longitudinal shift of focal length for the paraxial rays and the marginal rays. It is longitudinal spherical aberration (LSA) [83]. For example, in a convex lens, the marginal rays are focused closer to the lens, leading to a positive LSA value. In this paper, the edge pinning effect is used to suppress the LSA. More details will be presented below.

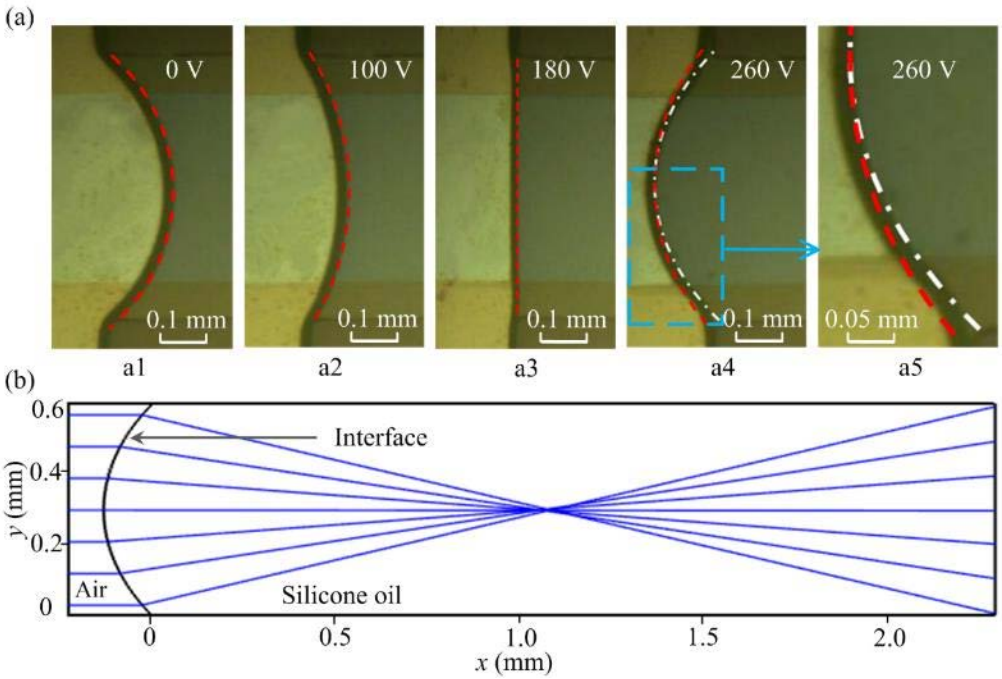

Fig. 5.7 Measurement and calculation of the liquid-air interfaces at different voltages. (a) Experimental measurements of the interface under 0 V (i.e. initial state), 100 V, 180 V and 260 V, respectively. The red dashed lines represent the ideal spherical interface. The white dashed-dotted line in a4 is the real interfacial curve derived from the captured image. And a5 is the enlarged view of the contact line of a4. (b) Ray tracing calculation of the measured liquid-air interface in a4.

5.3 Raytracing simulation and experimental results

5.3.1 Liquid-air interface measurement and ray tracing simulation

Experiments have been conducted to demonstrate the DEP-actuated liquid lens. The fabrication of the devices can be found in chapter 3. At first, a small amount of silicone oil is placed at the inlet of the open channel. Due to the capillary force, the liquid automatically flows into the channel and stops at the other end of the channel, resulting in a concave liquid-air interface (Fig. 5.7(a1)). The initial liquid-air interface matches closely a spherical curve (red dashed line) with a radius of -404 μm. Then, a voltage is applied to the ITO electrodes, generating an electric field between the two plates. With the increase of voltage, the DEP force deforms

the interface from initially concave to flat and then convex continuously. At 100 V, the magnitude of the interfacial radius becomes larger (see the dashed line in Fig. 5.7(a2), the calculated radius is -574 μm and the DEP force is $F_e = 4.83\times10^{-7}$ N,). A flat interface appears at 180 V ($F_e = 1.57\times10^{-6}$ N), see Fig. 5.7(a3). Further increase of the voltage results in a convex shape. Fig. 5.7 (a4) exemplifies the interface under 260 V ($F_e = 3.27\times10^{-6}$ N). It is noted that there is a deviation between the theoretical spherical curve (red dashed line) and the captured image (white dash-dot line) at the margin (see the enlarged view in Fig. 5.7(a5)). It is because of the edge pinning effect, which constrains the liquid-air interface at the lateral side, resulting in a smaller curvature at the margin of the interface. A ray tracing simulation is conducted to theoretically analyze the focusing performance of the convex lens (see Fig. 5.7(b)), showing that the parallel beams are well focused into a single point. This implies that the LSA is lower in the real liquid interface as compared to the ideal spherical interface. Detailed data will be presented below.

5.3.2 Experimental analysis of the focusing performance

(1) Experimental raytracing

To experimentally trace the light path inside the microfluidic chip, the silicone oil is added with fluorescent dye Nile Red, which absorbs green light and emits fluorescence for easy visualization using the CCD imaging. Fig. 5.8 presents the observed focusing states of the DEP-actuated liquid lens. A collimated probe beam (λ = 532 nm, waist diameter 400 μm, optical power 10 mW) is coupled into the chip and propagates from air to silicone oil (i.e., from left to right in Fig. 5.8).

Initially (i.e., at 0 V), the interface is concave by the balance of the surface tension, working effectively as a divergent lens (see Fig. 5.8(a)). Then, an external voltage is applied to the two parallel plates, generating an electric field in the liquid layer. The applied voltage is gradually increased from 0 V at a step of 5 V. At 180 V, a flat interface appears (see Fig. 5.8(b)). It has no focusing effect on the collimated probe beam. With further increase of the voltage, the DEP force deforms the liquid-air interface into a convex lens, converging the beam to a focal point (see Fig. 5.8(c)). By applying a voltage of 260 V, a minimum focal length of about 1 mm is obtained. Fig. 5.8(d) shows that the beam is well converged into a focal point, matching the ray tracing simulation in Fig. 5.7(b).

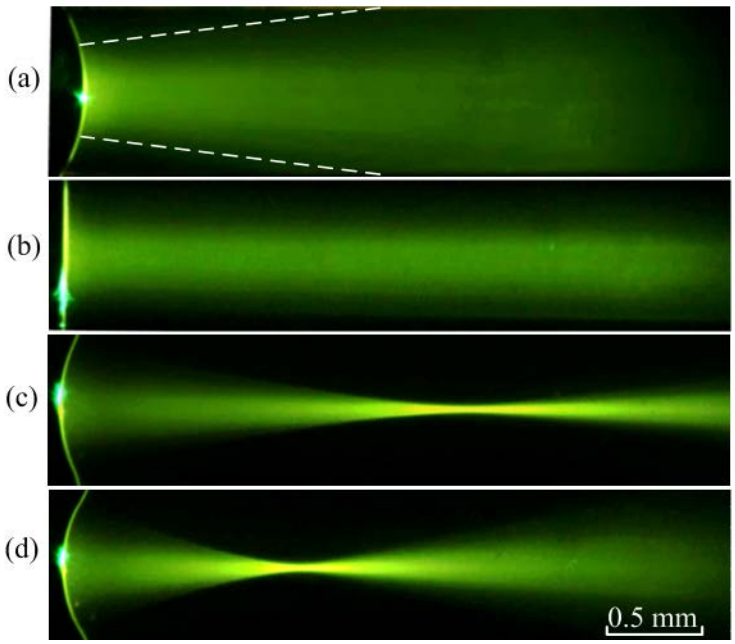

Fig. 5.8 Experimentally observed focusing states at different applied voltages. (a) Initial state: the parallel probe beam becomes divergent after passing through the liquid-air interface. (b) Flat interface at 180 V: the probe beam keeps parallel in the liquid medium. (c) Focusing state: the probe beam is converged with the further increase of the voltage. (d) A minimum focal length of about 1 mm is achieved at 260 V.

Table 5.1 The relationship between the focal length and the applied voltage of the divergent lens (from 0 to 170 V). The applied voltage: V (V); the calculated focal length: f_{cal} (mm); the experimental focal length: f_{exp} (mm) and the experimental error bar (standard deviation): Er. The experimental focal length is the average of five independent measurements.

V	0	20	40	60	80	100	110	120	130	135	140	145	150	155	160	165	170
f_{cal}	-1.27	-1.29	-1.35	-1.45	-1.63	-1.90	-2.11	-2.37	-2.74	-2.99	-3.28	-3.67	-4.15	-4.82	-5.73	-8.35	-9.60
f_{exp}	-1.06	-1.40	-1.50	-1.60	-1.50	-1.60	-1.70	-2.00	-2.60	-3.13	-3.25	-4.20	-4.42	-4.60	-5.70	-8.50	-10.40
Er	0.20	0.23	0.23	0.35	0.30	0.23	0.26	0.24	0.30	0.28	0.35	0.31	0.50	0.62	0.70	0.65	0.80

Table 5.2 The relationship between the focal length and the applied voltage of the convergent lens (from 190 to 260 V). The applied voltage: V (V); the calculated focal length: f_{cal} (mm); the experimental focal length: f_{exp} (mm) and the experimental error bar: Er (standard deviation). The experimental focal length is the average of five independent measurements.

V	190	195	200	205	210	215	220	225	230	235	240	245	250	255	260
f_{cal}	20.88	11.15	7.66	5.72	4.58	3.76	3.21	2.75	2.42	2.13	1.91	1.71	1.55	1.40	1.27
f_{exp}	14.20	10.00	6.80	6.00	5.07	4.21	3.54	3.10	2.48	2.02	1.75	1.50	1.27	1.16	1.04
Er	0.40	0.50	0.37	0.31	0.36	0.29	0.34	0.19	0.25	0.19	0.22	0.20	0.20	0.18	0.12

(2) Tunability of focal length

For quantitative analysis, the relationship between the focal length and the applied voltage is plotted in Fig. 5.9 (the numerical values are shown in Table 5.1 and Table 5.2). To put the data of the divergent state (blue circles and blue line) and convergent state (black circles and black line) in one figure, they are plotted using different axes, as indicated by the arrows. When the voltage increases from 0 V to 180 V, the focal length declines from -1 mm to infinite (top and right axes). When the voltage is further increased, it turns into a convex lens. The focal length gradually decreases from infinite to about 1 mm (at 260 V). In Fig. 5.9, the lines represent the calculated focal length (paraxial beam) and the data points are the experimental results. Each data point is an average of five independent measurements. The experimental result is in good agreement with the theoretical

predication. Therefore, the spherical approximation provides a reliable way to predict the focus performance of the DEP-actuated optofluidic lens.

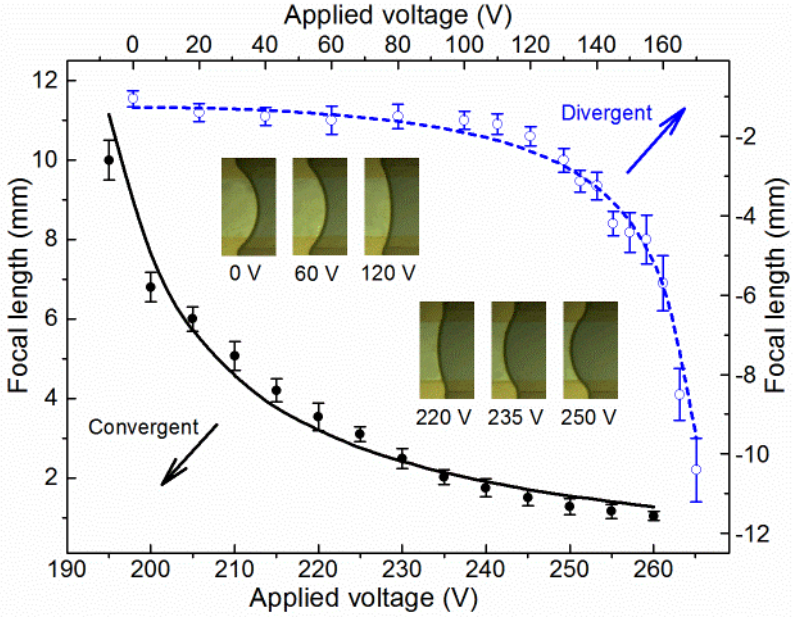

Fig. 5.9 The calculated (the curves) and the experimental (data points) focal lengths under different driving voltage. When the voltage is increased from 0 to 180 V, the focal length decreases from about -1 mm to infinite (top and right axes). While the voltage keeps increasing, the lens turns into a convex one and the focal length gradually decreases from infinite to about +1 mm (the bottom and left axes). The insets show the observed liquid-air interfaces under 0 V, 60 V, 120 V, 220 V, 235 V and 250 V for easy visualization

5.3.3 Suppressed longitudinal spherical aberration (LSA)

Due to the edge pinning effect, the contact line is partially pinned at the terminal of the open channel. This pinning effect reduces the marginal curvature (when it turns into convex), thereby suppressing the LSA. Fig. 5.10 displays the comparison between the LSAs of the ideal spherical lens and the experimental lens (the numerical comparison is shown in Table 5.3). Here LSA is represented by $\Delta f/f$, where f is the focal length of paraxial rays and Δf is the difference of focal lengths between the paraxial rays and the marginal rays. For the ideal spherical lens, the LSA is always positive and looks significant at short focal length (see

black squares and black line in Fig. 5.10). With the increase of focal length, the LSA drops monotonically. In contrast, the experimental interface has a negative LSA at short focal length and approaches the trend of the spherical lens for $f > 2.8$ mm. The color section in Fig. 5.10 indicates that the LSA of the experimental interface is limited to the range of -0.03 ~ +0.04 (maximum magnitude 0.04), while that of the spherical interface is over +0.01 ~ +0.135 (maximum magnitude 0.135). The experimental interface has much smaller magnitude of LSA than the spherical interface. This implies that the suppressed LSA is an intrinsic merit of the DEP-actuated liquid lens. The two insets in Fig. 5.10 illustrate the LSAs of the spherical and experimental interfaces, respectively. In the spherical interface, the marginal rays are focused closer to the interface, this is the reason for the positive value of LSA. In the DEP-actuated convex liquid-air interface, the marginal rays cross each other just behind the paraxial focal point, leading to a smaller but negative value of LSA.

Table 5.3 Comparison of the longitudinal spherical aberrations. The calculated focal length: f_{cal} (mm) and the calculated aberration: LSA_{cal}. The experimental focal length: f_{exp} and the experimental aberration: LSA_{exp}.

f_{cal}	1.313	1.472	1.640	1.849	2.078	2.372	2.711	3.168	3.732	4.557	5.697
LSA_{cal}	0.134	0.110	0.091	0.073	0.059	0.046	0.036	0.026	0.019	0.013	0.008
f_{exp}	1.230	1.295	1.362	1.550	1.850	2.283	2.885	3.250	4.000	4.685	5.490
LSA_{exp}	-0.028	-0.019	-0.008	0.019	0.040	0.040	0.029	0.031	0.020	0.016	0.015

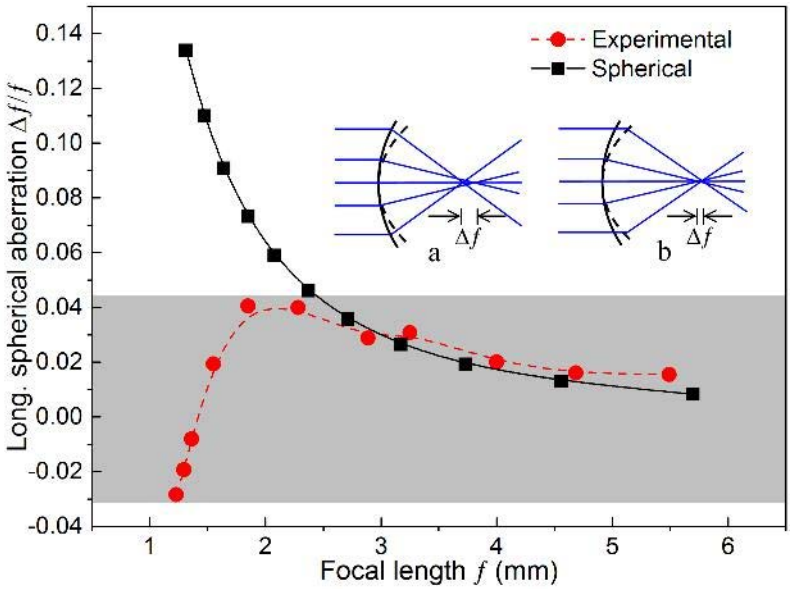

Fig. 5.10 Comparison of the longitudinal spherical aberrations $\Delta f/f$ of the experimental interface and the ideal spherical interface. The two insets show the ray tracing of the spherical (a) and the experimental interfaces (b), respectively. In the insets, the solid black line represents the spherical interface, and the black dashed line stands for the experimental interface.

5.4 Discussions

5.4.1 Merits of DEP-actuated lens

This is the first demonstration of in-plane liquid lens based on dielectrophoresis. By using DEP, the liquid/air interface can be continuously tuned from concave to convex, achieving wide tunable range of the focal length. The actuation is exerted though a simple electrode, which greatly simplify the structure of the device. The DEP actuated lens has some advantages over the previous reported liquid lenses [13].

(a) Low power consumption: The power consumption can be estimated by treating the device as a parallel-plate capacitor. The measured resistance of the

device is > 500 MΩ, showing its good insulation. The open channel has the dimensions 10 mm × 0.6 mm × 55 μm (L×W×H), and the silicone oil has the relative permittivity of 2.5, then the capacitance of the device is about 2.4 pF. In one charging process from 0 to 260 V, the consumed electrical energy is estimated to be 81 nJ per switching process, well showing the merit of low power consumption of this device.

(b) Great repeatability and durability: We also investigated the hysteresis and the durability of the device. It is observed that the interface shape can be well restored to its original state after the driving voltage is changed and then returned to the original value. Therefore, the device has very good repeatability and negligible hysteresis. It has also very good durability. Continuous operation for about one month has been demonstrated in the experiment, with little change of the focusing properties. This may be due to the low evaporation of the silicone oil in air.

(c) High scalability: As the actuation mechanism is simple and the continuous flow is not required, it has the potential to achieve a multiple lenses system or integrate with other microfluidic networks.

(d) Large tunable range: The DEP deforms the liquid-air interface from concave to convex, achieving the modulation from divergent to convergent. Using the liquid-air interface ensures large refractive index difference, leading to a small focal length at about 1 mm.

5.4.2 Limitations of DEP-actuated liquid lens

The only problem is the slow response. The response time depends on the

magnitude of the voltage variation. For instance, it takes about 4 s to switch from the initial concave state to the convex one with the shortest focal length and to then stabilize in the final state. And the response is continuous, i.e., it goes continuously from the initial state to the new balanced state when the voltage experiences a step change. The width of the channel has significantly influence on the "response time". This is because there are two forces (i.e., the DEP force and the surface tension from the lateral sides) that play important roles in the lens system. A broad channel leads to a slow response. Another factor is the viscosity of the liquid, which describes the resistance to the deformation of liquid. The liquid with higher viscosity moves slower.

5.5 Summary

In summary, this chapter has presented a DEP-actuated reconfigurable optofluidic lens for in-plane light manipulation. It utilizes the DEP force to continuously modify the fluidic lens from concave to convex. The proposed liquid lens has some intrinsic merits: low power consumption (～81 nJ per switching), easy fabrication, static liquid flow (low liquid consumption) and wide tunability of focal length from negative to positive. The low evaporation rate of the silicone oil makes the liquid lens stable and well repeatable. More importantly, the longitudinal spherical aberration of the convergent lens is effectively suppressed (the magnitude of measured LSA is below 0.04). There are also some limitations of the proposed lens. For example, it takes about 4 s to switch from the initial concave state to the convex one with the shortest focal length; and it needs to be located at the end of the channel. Nevertheless, the simple design and the flexible tuning method make it suitable for microfluidic network integration and potential applications in the

lab-on-chip systems. It is noted that the DEP-actuated lens design in this chapter utilizes only one liquid-air interface. In fact, two liquid-air interfaces can also be used to form the lens, which would yield a shorter focal length and more freedoms to tune the lens. This inspires another design of DEP-actuated lens to be presented in next chapter.

Chapter 6 DEP-Actuated Optofluidic Lens with Two Liquid-Air Interfaces

The DEP-actuated lens in the previous chapter make use of only one liquid-air interface. This chapter will present an advanced version—a DEP lens using two liquid-air interfaces. Initially, two droplets are guided by the DEP force to form a symmetric biconcave liquid-air (silicone oil-air) lens in a microfluidic chip. Then, the liquid-air interfaces are tuned from biconcave to biconvex by DEP force from two electrodes on top of the lens. By increasing the applied voltage from 0 to 250 V, the focal length can be tuned from about -0.5 mm to infinite and then to around +0.5 mm. It achieves an *f* number of 0.91 but consumes only 6.7 nJ per switching circle. This liquid-air lens has a larger refractive index (RI) difference, resulting in a smaller focal length. The static flow and the electrical actuation lead to better compatibilities. Therefore, it will find some potential applications in lab-on-a-chip systems.

6.1 Brief introduction

Some liquid GRIN lenses have been demonstrated using solution diffusion [31] or thermal gradient [17]. Nevertheless, most of the liquid lenses are based on the fluidic interfaces, which can be manipulated by several types of microfluidic methods, such as hydrodynamic flow [69], pressure control [86] or electrostatic force [27], etc. Among them, the hydrodynamic flow has been widely used to control the in-plane optofluidic lens. The optical smoothness of the fluidic interface makes it suitable for light manipulation in microfluidics. Generally, the liquid lens with two fluidic interfaces is formed by the immiscible flowing streams

with different RIs, where the liquid with higher RI acts as the core and the one with lower RI as the cladding. Its shape (or focal length) can be continuously tuned by changing the flow rate, providing a flexible way to manipulate light in microfluidic network. By injecting three flow streams into expansion chambers with rectangle or circular shapes, several reconfigurable lenses have been demonstrated. Seow et al. proposed a reconfigurable liquid lens by changing flow rates of three laminar streams in a rectangle expansion chamber [42]. Three working states: biconvex, planar convex, and concave convex lenses were demonstrated. To get a perfect curvature, a circular chamber was used in a liquid core / liquid cladding lens [43]. The shape can be tuned from the radius of the chamber itself to infinite via the flow rate control. Fang et al. reported another reconfigurable optofluidic lens, which was hydrodynamically tuned from biconvex to biconcave [39]. It utilized a rectangle chamber with two semicircular terminals that connected to two inlets and two outlets. By adjusting the flow rates of four streams, the light was continuously tuned from focusing to collimation and then to divergence. The above designs have demonstrated flexible tunability of the optofluidic lens, which can be used for lab-on-a-chip applications. But there are still some limitations in the previous liquid lenses. For instance, the requirement of the continuous liquid supply consumes large amount of solution and reduces the compatibility of the lens. The focal length is limited by the small RI difference between liquids. Thus, more practical designs of in-plane optofluidic lens are still in need.

Here we report an electrically reconfigurable liquid-air lens that can be tuned from biconcave to biconvex. The tunning is achieved by the DEP force from the

top and bottom electrodes. It not only has a flexible tunability, but also has a low longitudinal spherical aberration (LSA). In addition, it does not require a continuous liquid supply, making it highly scalable in the microfluidic networks. The large RI difference at the liquid-air interface leads to a wide tunable range of focal length from -0.5 mm to +0.5 mm. Both the theoretical calculations and the experimental results demonstrate the great performance of this optofluidic lens.

6.2 Working principle

6.2.1 Schematic design and device fabrication

The schematic design of the liquid lens is shown in Fig. 6.1. Two parallel MgF_2 glasses are utilized to form the microfluidic platform, where the NOA 81 (Norland Optical Adhesive 81) works as the spacer and defines two open channels (along the *x* direction). The two open channels meet each other at the center. The top glass is patterned with ITO film as the electrode. A uniform ITO layer is deposited on the bottom glass as the ground. The top electrode consists of two parts: an ITO line (along the *x* direction) on top of the two open channels and a pair of ITO patterns (*y* direction) on top of the lens section. The ITO line is used to apply a DEP force (voltage: V_0) to guide the droplets from the two open channels to merge at the center ($x = 0$, $y = 0$) of the intersection, resulting in a biconcave liquid-air lens (as shown in the inset of Fig. 6.1). And the ITO pair (V_1 & V_2) are used to exert the DEP force on the liquid and deform the lens shape (see the blue liquid). V_1 and V_2 pull the liquid-air interfaces in the -*y* and +*y* directions, respectively. It can be continuously tuned from biconcave to biconvex by DEP force. The lens section is 0.55 mm × 1.05 mm × 0.06 mm (L × W × H). To observe the

lensing effect, A collimated beam (λ = 532 nm, waist diameter = 400 μm) is coupled into the chip using a pigtailed aspheric fiber collimator (CFS2-532-FC, beam divergence 1.75 mrad, Thorlabs). And a chamber (not included in the schematic) is fabricated behind the lens section for experimental raytracing.

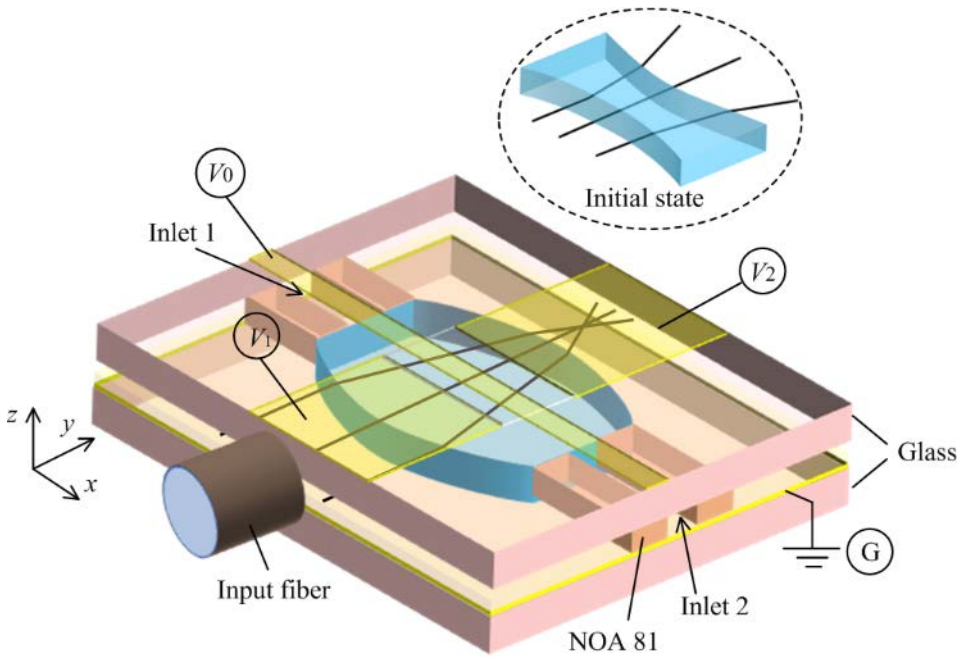

Fig. 6.1 Schematic design of the optofluidic lens. Two parallel glasses are firmly bonded by NOA 81 adhesive strips, forming two open microchannels. The channels have a disconnect port in the middle section, at which the fluidic lens (the blue liquid) locates. Two inlets at the ends of the chip are used for capillary flow to fill the channels. V_0 is used to drag the droplets from the two inlets to merge at the center, forming a biconcave liquid lens (see the inset). Then, V_1 and V_2 are utilized to deform the two liquid-air interfaces. A collimated beam is coupled into the chip by an input fiber.

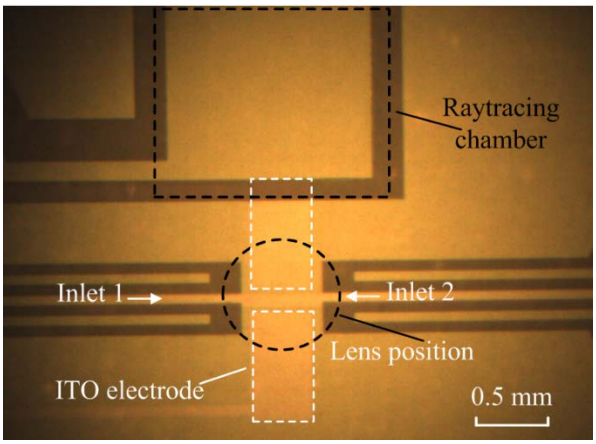

Fig. 6.2 Fabricated device of the DEP-actuated lens: the lens section is at the center, after that is the raytracing chamber.

The device is fabricated using the microfabrication techniques described in Chapter 3. The ITO electrodes are fabricated by the lift-off process. Then two glasses are bonded together by the capillary filling assisted method. A microscope image of the fabricated device shows the inside structures of the lens, see Fig. 6.2. The lens section is located in between two open channels (two inlets).

6.2.2 Theory of interface modulation

Initially, the shape of the liquid droplet is determined by surface tension. There is a pressure drop at the liquid-air interface, which can be described by Laplace law

$$\Delta P_0 = 2\gamma\kappa = \gamma\left(\frac{1}{R_{10}} + \frac{1}{R_{20}}\right) \tag{6.1}$$

where ΔP_0 is the pressure drop, γ ($\gamma_{\text{silicone oil}}$ = 20 mNm^{-1}) is the surface tension coefficient between the liquid and the air, and κ is the mean curvature. R_{10} and R_{20} are the curvature radii in the horizontal and vertical directions, respectively. As the device is symmetric along the x and y axes, the two liquid-air interfaces have the same physical states. When a voltage is applied to the ITO pair, it exerts a net force at the liquid-air interfaces to deform the shape of the droplet. The DEP force at one liquid-air interface can be described by [76]

$$F_e = \frac{\varepsilon_0 (\varepsilon_L - 1) w_1}{2 d_0} V^2 \tag{6.2}$$

where $\varepsilon_0 = 8.8542 \times 10^{-12}$ F/m is permittivity of vacuum and ε_L ($\varepsilon_{\text{silicone oil}} = 2.5$) is relative permittivity of the liquid, w_1 is width of the top electrode and d_0 is the height of the channel. V represents the applied voltage. The external force changes the balance state of the interface, resulting in a different pressure drop and curvature:

$$\Delta P_1 - \Delta P_0 = \gamma\left(\frac{1}{R_{11}} + \frac{1}{R_{20}}\right) - \gamma\left(\frac{1}{R_{10}} + \frac{1}{R_{20}}\right) = \gamma\left(\frac{1}{R_{11}} - \frac{1}{R_{10}}\right) \tag{6.3}$$

here R_{10} and R_{11} are the horizontal curvature radii of the initial and new states, respectively. And ΔP_1 is the pressure drop of the new balanced state. As the contact properties of the top and bottom glasses remain unchanged, the vertical curvature radius R_{20} is constant. And the DEP force is balanced by the surface tension:

$$F = (\Delta P_1 - \Delta P_0) w_0 d_0 = F_e \tag{4}$$

where w_0 is the distance between the terminals of the two channels. Thus $S = w_0 d_0$ is the y-direction projection of a liquid-air interface. The horizontal radii of the new interfaces are determined by Eqs· (6.1)-(6.4). If $V_1 = V_2$, the liquid lens is in symmetric state, which means that the two liquid-air interfaces have the same curvature radius in magnitude.

6.2.3 Optical model of thick lens

Since the width of the droplet is not negligible in comparison with the curvature radius, it can not be regarded as a thin lens. The optical properties of the liquid

lens can be described by the Snell law. And the lens can be considered as two separated liquid-air interfaces, where the rays bend according to the Snell law. The rays propagate along the straight line inside and outside of the liquid. Fig. 6.3 displays the optical model of the biconcave and biconvex liquid lenses in this paper.

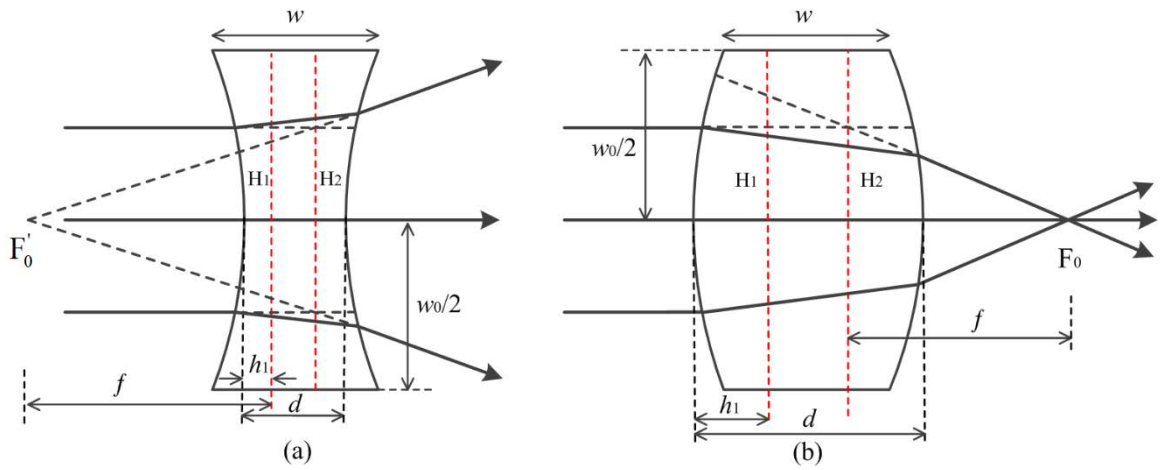

Fig. 6.3 Optical model of the DEP lens. w and w_0 are width and length of the open section, respectively. H_1 and H_2 are the first and second principal planes. The distance between the two liquid-air interfaces is d. (a) Defocusing of the biconcave liquid lens; (b) Focusing of the biconvex lens.

In Fig. 6.3a, the parallel rays diverge after the passing the biconcave lens, which seem to be from a back focal point F_0'. While in the biconvex lens, the parallel rays are focused into a point F_0, see Fig. 6.3b. The two red lines (H_1 & H_2) in Fig. 6.3 indicate the two principal planes of the lens. And the effective focal length f can be expressed as

$$\frac{1}{f}=(n-1)\left[\frac{1}{R_1}-\frac{1}{R_2}+\frac{(n-1)d}{nR_1R_2}\right] \tag{6.5}$$

where n is RI of the liquid, R_1 and R_2 are the radii of the first and second interfaces, respectively. And d is the thickness of the lens. The positions of the two principal planes are determined by:

$$h_1 = -\frac{f(n-1)d}{nR_2} \tag{6-6}$$

$$h_2 = -\frac{f(n-1)d}{nR_1} \tag{6-7}$$

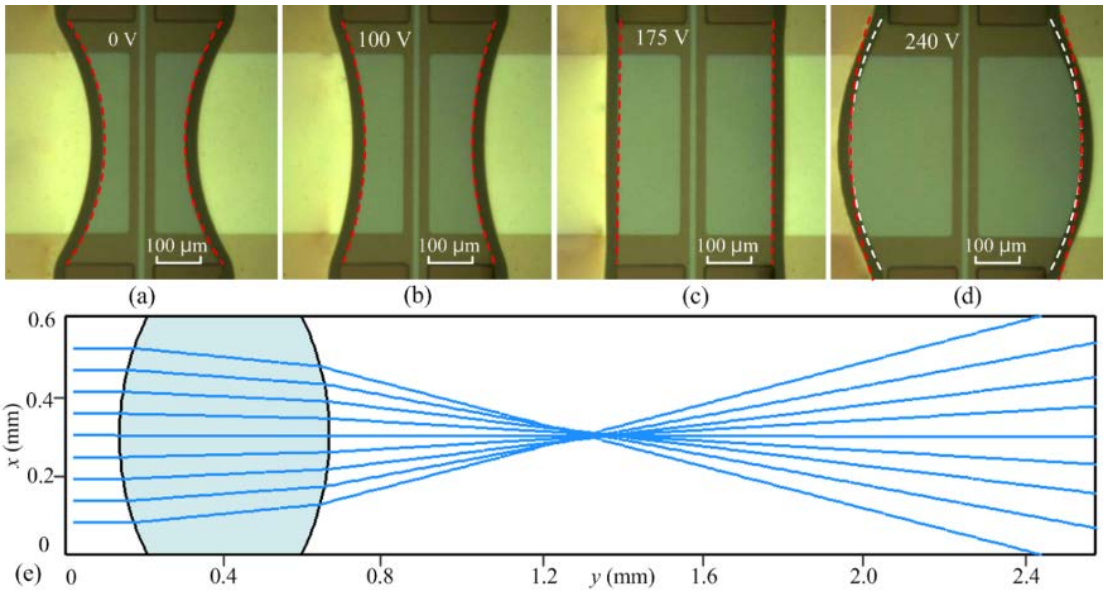

Fig. 6.4 (a)-(d): measured liquid-air interfaces under different applied voltages: (a) 0 V; (b) 100 V; (c) 175 V and (d) 240 V. The red dashed circle lines are the calculated results. And the white dashed lines in (d) represent the experimental curves. (e) Raytracing of the liquid lens in (d).

6.3 Raytracing simulation and experimental results

6.3.1 Liquid-air interface measurement and raytracing simulation

The lens will be demonstrated theoretically and experimentally. First, some theoretical calculations will be conducted to analyze the tunable liquid lens. Then some experiments will be carried out for verification.

At first, some experiments are conducted to measure the liquid-air interfaces under different voltages. Initially, a biconcave droplet is formed in the microfluidic chip, as shown in Fig. 6.4a. The two liquid-air interfaces have the same curvature because of the symmetric design. At first, the magnitude of the radius increases with higher voltage, see Fig. 6.4a and b. Then, the two liquid-air interfaces become flat at 175 V (Fig. 6.4c). With the further increase of the voltage, it turns into a biconvex shape, as shown in Fig. 6.4d. In the biconvex case, the radius magnitude reduces with higher voltage. For comparison, the calculated spherical curves (red dashed curves) are marked in the corresponding experimental results in Fig. 6.4a-d. It is noticed that the experimental interfaces closely match the theoretical curves. In addition, the edge pinning effect makes the curvature smaller at the marginal section when it is in the focusing state. Fig. 6.4d shows the comparison between theoretical (red) and the experimental curves (white). The edge pinning effect can be used to suppress the longitudinal spherical aberration (LSA), resulting in a better focusing performance. The raytracing simulation of Fig. 6.4(d) is shown in Fig. 6.4e, which demonstrates the focusing effect of the liquid lens.

6.3.2 Experimental analysis of lensing effect

(1) Experimental raytracing

In order to trace the beam, a chamber is fabricated behind the lens. It is filled with the mixer of NOA 81 and Rhodamine B for fluorescent imaging. At first, the liquid droplet has a biconcave shape resulted from the surface tension. The beam becomes divergent after passing the divergent lens, as shown in Fig. 6.5a. When the voltage increases gradually from 0 V, the droplet is deformed by the DEP force. At 175 V, it becomes a flat lens, which has no focusing effect. As shown in Fig.

6.5b, the parallel beam keeps almost unchanged. While the voltage keeps on increasing, the lens turns into a biconvex one. Then the focusing effect appears as shown in Fig. 6.5c. The focal length of about 0.6 mm is obtained at 245 V (see Fig. 6.5d). In Fig. 6.5d, the beam is well focused to a small spot because of the low LSA resulted from the edge pinning effect. To make it easy to measure the focal length, the focal length is defined as the distance from the lens to the focal point.

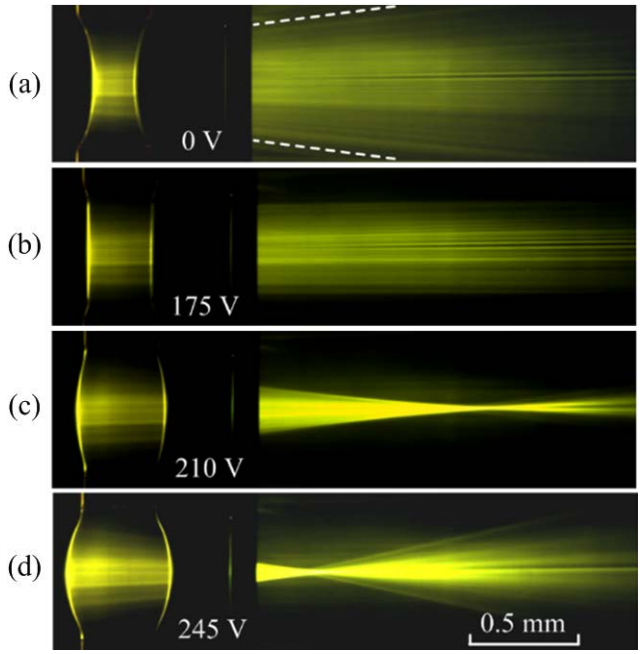

Fig. 6.5 Focusing states under different applied voltages. (a) The liquid-air interfaces work as a divergent lens when the applied voltage is off. (b) They form a plane lens at the voltage of 175 V. (c) Further increase of the voltage results in the focusing effect. (d) At 245 V, a focal length of about 0.6 mm is obtained. The experimental raytracing only shows the beams inside the tracing chamber, which means the focal length should consider the distance (0.4 mm) between the chamber and the lens.

Table 6.1 The relationship between the focal length and the applied voltage of the divergent lens. Voltage: the applied voltage on the device; f_{cal}: the calculated focal length; f_{exp}: the experimental focal length, which is the average of five independent measurements; Er_{exp}: the standard deviation of the experimental focal length.

Voltage (V)	0	15	30	45	60	75	90	105
f_{cal} (mm)	-0.633	-0.637	-0.652	-0.677	-0.717	-0.774	-0.857	-0.981
f_{exp} (mm)	-0.740	-0.809	-0.863	-0.898	-0.959	-1.027	-1.134	-1.201
Er_{exp}	0.115	0.078	0.099	0.107	0.128	0.164	0.155	0.185
Voltage (V)	120	135	145	155	160	165	168	170
f_{cal} (mm)	-1.178	-1.527	-1.954	-2.802	-3.639	-5.281	-7.327	-9.947
f_{exp} (mm)	-1.332	-1.493	-1.772	-2.636	-4.846	-6.548	-8.011	-9.174
Er_{exp}	0.184	0.158	0.185	0.328	0.483	0.569	0.435	0.547

Table 6.2 The relationship between the focal length and the applied voltage of the convergent lens. Voltage: the applied voltage on the device; f_{cal}: the calculated focal length; f_{exp}: the experimental focal length, which is the average of five independent measurements; Er_{exp}: the standard deviation of the experimental focal length.

Voltage (V)	180	181	183	185	188	190	195	200	205
f_{cal} (mm)	11.348	9.273	6.767	5.308	3.991	3.414	2.487	1.937	1.572
f_{exp} (mm)	10.358	8.429	6.757	5.583	4.846	3.862	2.297	1.970	1.808
Er_{exp}	0.508	0.476	0.515	0.486	0.587	0.530	0.376	0.421	0.426
Voltage (V)	210	215	220	225	230	235	240	245	250
f_{cal} (mm)	1.313	1.118	0.967	0.845	0.745	0.662	0.590	0.527	0.472
f_{exp} (mm)	1.573	1.335	1.209	1.047	0.911	0.798	0.725	0.633	0.579
Er_{exp}	0.423	0.385	0.355	0.239	0.235	0.171	0.164	0.135	0.115

(2) The tunability of the liquid lens

To analyze the tunability of the DEP lens, the relationship between the focal length and the applied voltage has been measured. The calculated and experimental results are listed in Table 6.1 and Table 6.2 and are plotted in Fig. 6.6. For direct comparison, the theoretical predictions are plotted in Fig. 6.6 as well (solid and dashed lines). As shown in Fig. 6.6, when the voltage increases from 0 to 175 V,

the focal length decreases from about -0.5 mm to infinite (see the top-right axes). Further increase the voltage, the lens turns into a biconvex shape. Its focal length decreases from infinite (around 175 V) to about +0.5 mm at 250 V. It is noticed that the experimental results closely match the theoretical curves, which means that the theoretical calculation offers a good prediction in the tunning of the lens. As shown in Fig. 6.6, there are four insets to illustrate the biconcave lenses (at 30 V and 120 V) and the biconvex lenses (at 200 V and 230 V).

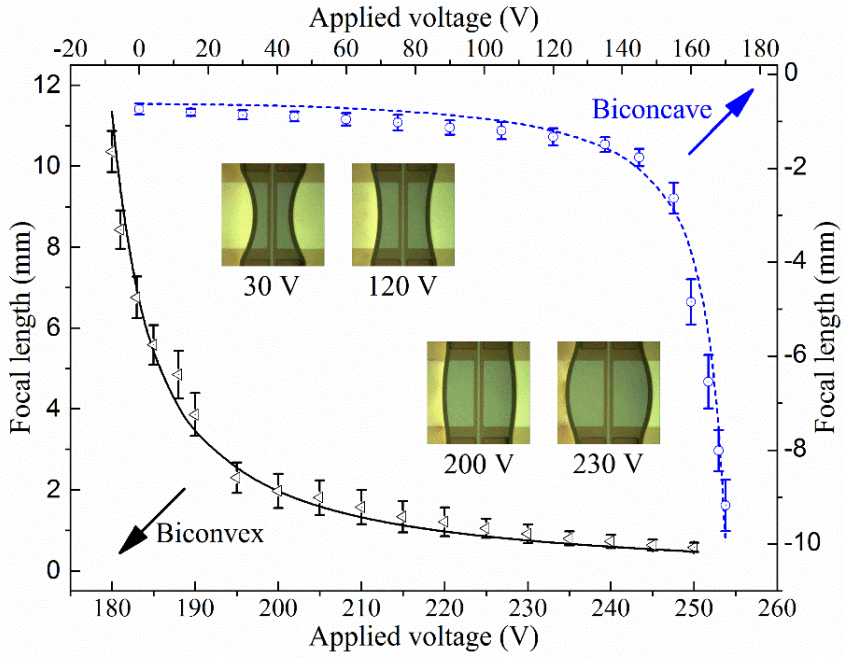

Fig. 6.6 Tunability of the focal length f. At first, when the voltage increses from 0 to 175 V, the focal length decreses from about -0.5 mm to infinite, see the blue line and the data points. Furhter increase of the voltage causes it to turn into a convergent lens. And the focal length can be tuned from infinite to around +0.5 mm, see the black line and the data points. Here the lines are the theoretical predictions and the data points are the experimental results . The insets exemplify the states of the lens at different voltages.

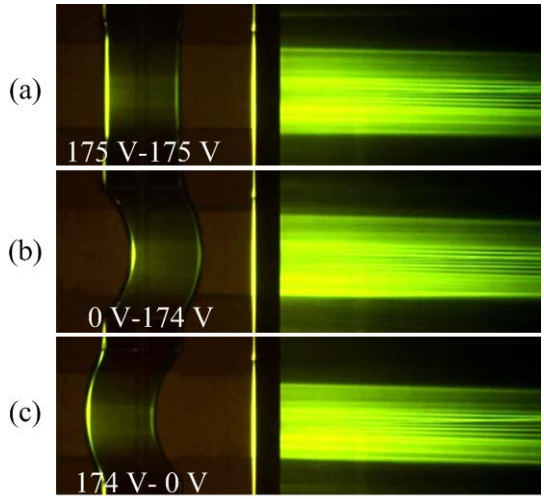

Fig.6.7 Asymmetric manipulation of the two liquid-air interfaces

(3) Asymmetric working states

The two liquid-air interfaces can also be control independently. As shown in Fig. 6.7a, when the two interfaces are under 175 V, a planar lens appear. Then only apply 174 V to one of the interfaces and keep one of them at 0 V, the lens is deformed to concave-convex or convex-concave shapes. The probe beam keeps collimated after passing both of the above asymmetric lenses.

6.4 Discussions

6.4.1 Power consumption, repeatability, *f* number and response time

Silicone oil is chosen as the optical medium because of its favorable properties, such as high transparence, low evaporation rate, low viscosity and high electrical insulation. The optically smooth interface and the low absorption of the liquid lead to a low optical loss. And the low evaporation rate of the liquid makes the lens well repeatable for the experimental operation over one month. Since the silicone oil layer has a very high electrical resistance (over 500 MΩ), the device can be regarded as a capacitor (0.55 mm × 1.05 mm × 0.06 mm). The energy

consumption is estimated to be as low as 6.7 nJ per switching circle. The propose liquid lens also has a large *f* number, which is define as f/D (the aperture is 0.55 mm). At 250 V, the smallest focal length is about 0.5 mm, resulting in an *f* number of 0.91. But the response speed of the lens is slow due to the large lens size and the edge pinning effect. The modulation is resulted from the DEP force and the edge pinning effect, which is related to the size of the device and the viscosity of the liquid. In experiment, it takes about 6 s to switch from -0.5 mm to +0.5 mm. The response speed can be improved by reducing the size of the lens or choosing a liquid with lower viscosity.

6.5 Summary

This chapter has presented an electrically reconfigurable liquid lens using two liquid-air interfaces. Combining the surface tension and the dielectrophoresis together, this in-palne optofluidic lens can be continuously tuned from biconcave to biconvex. As a result, the focal length varies from about -0.5 mm to infinite (175 V) and then from inifinite to around +0.5 mm (250 V). It can also work at asymmetric states. The proposed liquid lens has some advanteges over the previous in-plane lenses, such as low power consumption (6.7 nJ), no requirement of continuous liquid supply and large *f* number. The large RI difference at the liquid-air interface leads to smaller focal length. In addition, the easy fabrication and the electrical modulation make it easy to integrate multiple lenses inside a microfluidic network. Therefore, it will find some potential applications in the lab-on-a-chip systems.

Chapter 7 Conclusion and Future Work

7.1 Conclusion

In this doctoral study, three different in-plane optofluidic lenses have been demonstrated for in-plane light manipulation. The first one is based on the thermal lens effect and the last two are actuated by the DEP force. These optofluidic lenses provide new methods for light coupling, manipulation and other microfluidic applications. The capillary filling assisted bonding technique has been developed to fabricate microfluidic chips in between two parallel glasses. In some specific circumstances, this new bonding method provides a flexible way for micro device fabrication. Table 7.1 is a comparison of the previous reported devices and three designs developed in this study.

Table 7.1 Comparison between previous reported lenses and three lenses developed in this doctoral study

Design	Range of focal length	Tuning speed	Power consumption	Spherical aberration	Continuous liquid supply
Previous reported devices	∞ ~ 2.75 ∞ ~ -1.21	Slow	High	Aberration free	Yes
Laser-induced thermal lens	Only focusing state: ∞ →1.3 mm	200 ms	0.03 J/switching	Aberration free	Yes
DEP-actuated lens using single liquid-air interface	Concave to convex -1 mm→∞→+1 mm	4 s	81 nJ/switching	Well suppressed aberration	No (one liquid)
DEP-actuated lens using two liquid-air interfaces	Biconcave to biconvex -0.6 mm→∞→+0.6 mm	6 s	6.7 nJ/switching	Suppressed aberration	No (one liquid)

In the first part, we have proposed a new design of optofluidic tunable lens that has a two-dimensional gradient distribution of RI. This is accomplished by using a continuous pump laser to irradiate two metal strips to generate a thermal gradient in a liquid layer. For the theoretical verification, a CFD simulation has been conducted to analyze the evolution process of the RI profile upon heating. Then, the tuning of the in-plane focusing states has been experimentally demonstrated by varying the pump laser intensity and the flow velocity. Compared with the previously-reported tunable liquid lenses, the design of this work is distinctive and advantageous in many aspects such as tuning speed (200 ms), aberration-free focusing, remote control and easy integration. In addition, this design utilizes only one type of liquid, which may be especially useful for some applications that can only use one liquid, or need to reuse the precious liquid.

In the second part, A DEP-actuated liquid lens using one liquid-air interface has been demonstrated. This is the first demonstration of the DEP-actuated in-plane lens. By using the DEP force to deform the liquid-air interface from concave to convex, the focal length is tuned from -1 mm to +1 mm. Both the raytracing simulation and the experimental results have confirmed its superior performance. Compared with the previous liquid lenses, the DEP lens has many merits, such as low power consumption (~81 nJ per switching), wide tunable range (-1 mm → ∞ → +1 mm), static flow and high compatibility. The static flow and the easy fabrication make it flexible to integrate several elements in a microfluidic network. In addition, the longitudinal spherical aberration has been effectively suppressed by the edge pinning effect, resulting in better focusing than the previous spherical liquid lenses. It may find potential applications in lab on-chip systems.

In the third part, an in-plane lens using two liquid-air interfaces is demonstrated. This DEP actuated liquid lens (with two liquid-air interfaces) has some advantages over the previous double fluidic-interfaces lens formed by flowing immiscible streams. The large RI difference between the liquid-air interface leads to a large tunable range of the focal length: from -0.5 mm to +0.5 mm. No requirement of continuous flow makes it highly compatible and scalable. It achieves a larger f-number while consuming only 6.7 nJ per switching circle. This new liquid lens has great perspectives in lab-on-a-chip applications.

7.2 Future work

As limitations still exist in this thesis, there are tips with further development in the future. Some suggestions of the future work are listed below:

(1) In the optofluidic thermal lens, the thermal gradient in the vertical direction is neglected. The thermal conductivity of the microfluidic chamber also has influence on the thermal diffusion as well as the temperature profile in the liquid. To obtain a precise result, these two factors should be taken into account. Some other optofluidic elements, such as optofluidic waveguides and optical switches can also be achieved using the thermal lens effect.

(2) In the DEP-actuated liquid lens, the stability of the device is determined by the interfacial tension, which makes it sensitive to the ambient vibration. An enclosed chip or a hydrophobic treatment may improve the performance of the device. Multiple lenses could also be achieved to realize complex optofluidic network. Another limitation of the DEP-actuated lens is the slow response, which takes a few seconds to switch from the initial state to the focusing state.

The response speed can be improved by choosing a liquid with lower viscosity or reducing the size of the device.

(3) Another recommendation of the future work is to develop practical applications of the proposed liquid lenses. For example, the laser-induced thermal lens can be used for particle manipulation or detection. In addition, a laser-induced thermal gradient can also be developed as a reconfigurable optical waveguide, whose location can be freely relocated. As for the DEP lenses, it is possible to integrate several independent lenses in a microfluidic chip to construct an on-chip imaging system. For example, Fig. 7.1 shows the schematic design of a imaging system using two DEP-actuated liquid lenses.

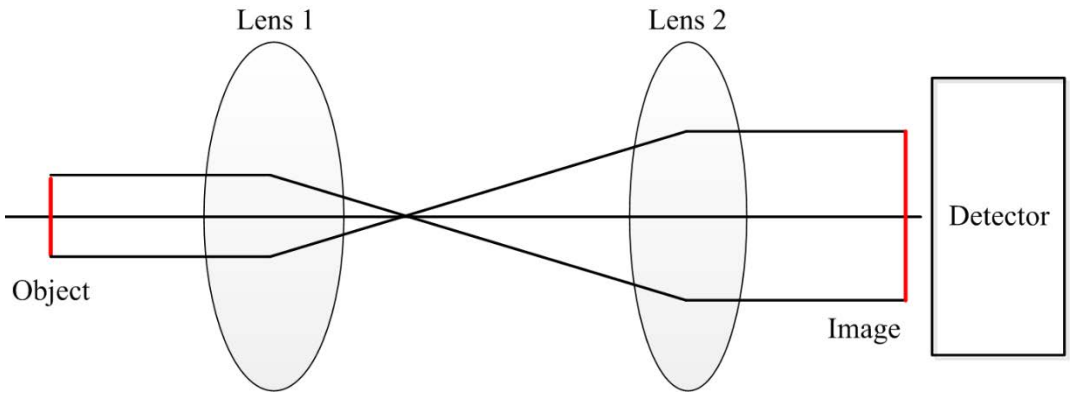

Fig.7.1 Micro imaging system using DEP-actuated lenses.

Reference

[1] Ho, C. M., & Tai, Y. C. (1998). Micro-electro-mechanical-systems (MEMS) and fluid flows. Annual Review of Fluid Mechanics, 30(1), 579-612.

[2] Miller, R. A., Nazarov, E. G., Eiceman, G. A., & King, A. T. (2001). A MEMS radio-frequency ion mobility spectrometer for chemical vapor detection. Sensors and Actuators A: Physical, 91(3), 301-312.

[3] Han, J., Cheng, P., Wang, H., Zhang, C., Zhang, J., Wang, Y., ... & Ding, G. (2014). MEMS-based Pt film temperature sensor on an alumina substrate. Materials Letters, 125(6), 224-226.

[4] Abeysinghe, D. C., Dasgupta, S., Boyd, J. T., & Jackson, H. E. (2001). A novel MEMS pressure sensor fabricated on an optical fiber. IEEE Photonics Technology Letters, 13(9), 993-995.

[5] Herrera-May, A. L., Aguilera-Cortés, L. A., García-Ramírez, P. J., & Manjarrez, E. (2009). Resonant magnetic field sensors based on MEMS technology. Sensors, 9(10), 7785-7813.

[6] Shaeffer, D. K. (2013). MEMS inertial sensors: A tutorial overview. IEEE Communications Magazine, 51(4), 100-109.

[7] Chu, P. B., Lee, S. S., & Park, S. (2002). MEMS: The path to large optical crossconnects. IEEE Communications magazine, 40(3), 80-87.

[8] Whitesides, G. M. (2006). The origins and the future of microfluidics. Nature, 442(7101), 368.

[9] Wang, Y., Lin, W. Y., Liu, K., Lin, R. J., Selke, M., Kolb, H. C. & Faull, K. F. (2009). An integrated microfluidic device for large-scale in situ click chemistry screening. Lab on a Chip, 9(16), 2281-2285.

[10] Monat, C., Domachuk, P., & Eggleton, B. J. (2007). Integrated optofluidics: A new river of light. Nature photonics, 1(2), 106.

[11] Lee, W., Li, H., Suter, J. D., Reddy, K., Sun, Y., & Fan, X. (2011). Tunable single mode lasing from an on-chip optofluidic ring resonator laser. Applied Physics Letters, 98(6), 061103.

[12] Yang, Y., Liu, A. Q., Chin, L. K., Zhang, X. M., Tsai, D. P., Lin, C. L., ... & Zheludev, N. I. (2012). Optofluidic waveguide as a transformation optics device for lightwave bending and manipulation. Nature communications, 3(651).

[13] Nguyen, N. T. (2010). Micro-optofluidic Lenses: A review. Biomicrofluidics, 4(3), 031501.

[14] Mandal, S., & Erickson, D. (2008). Nanoscale optofluidic sensor arrays. Optics Express, 16(3), 1623-1631.

[15] Xiong, S., Liu, A. Q., Chin, L. K., & Yang, Y. (2011). An optofluidic prism tuned by two laminar flows. Lab on a Chip, 11(11), 1864-1869.

[16] Fan, S. K., Chiu, C. P., Hsu, C. H., Chen, S. C., Huang, L. L., Lin, Y. H., ... & Yang, J. T. (2012). Particle chain display–an optofluidic electronic paper. Lab on a Chip, 12(22), 4870-4876.

[17] Liu, H. L., Shi, Y., Liang, L., Li, L., Guo, S. S., Yin, L., & Yang, Y. (2017).

A liquid thermal gradient refractive index lens and using it to trap single living cell in flowing environments. Lab on a Chip, 17(7), 1280-1286.

[18] Hongbin, Y., Guangya, Z., Siong, C. F., & Feiwen, L. (2008). Optofluidic variable aperture. Optics letters, 33(6), 548-550.

[19] Tang, S. K., Mayers, B. T., Vezenov, D. V., & Whitesides, G. M. (2006). Optical waveguiding using thermal gradients across homogeneous liquids in microfluidic channels. Applied physics letters, 88(6), 061112.

[20] Fan, X., & White, I. M. (2011). Optofluidic microsystems for chemical and biological analysis. Nature photonics, 5(10), 591.

[21] Zhu, H., White, I. M., Suter, J. D., Dale, P. S., & Fan, X. (2007). Analysis of biomolecule detection with optofluidic ring resonator sensors. Optics Express, 15(15), 9139-9146.

[22] Kühn, S., Phillips, B. S., Lunt, E. J., Hawkins, A. R., & Schmidt, H. (2010). Ultralow power trapping and fluorescence detection of single particles on an optofluidic chip. Lab on a Chip, 10(2), 189-194.

[23] Galas, J. C., Peroz, C., Kou, Q., & Chen, Y. (2006). Microfluidic dye laser intracavity absorption. Applied physics letters, 89(22), 224101.

[24] Lu, X., Samuelson, D. R., Xu, Y., Zhang, H., Wang, S., Rasco, B. A., ... & Konkel, M. E. (2013). Detecting and tracking nosocomial methicillin-resistant Staphylococcus aureus using a microfluidic SERS biosensor. Analytical chemistry, 85(4), 2320-2327.

[25] Zhang, W., Huang, L., Santschi, C., & Martin, O. J. (2010). Trapping and

sensing 10 nm metal nanoparticles using plasmonic dipole antennas. Nano letters, 10(3), 1006-1011.

[26] Zhang, W., Huang, L., Santschi, C., & Martin, O. J. (2010). Trapping and sensing 10 nm metal nanoparticles using plasmonic dipole antennas. Nano letters, 10(3), 1006-1011.

[27] Kuiper, S., & Hendriks, B. H. W. (2004). Variable-focus liquid lens for miniature cameras. Applied physics letters, 85(7), 1128-1130.

[28] Ren, H., & Wu, S. T. (2008). Tunable-focus liquid microlens array using dielectrophoretic effect. Optics Express, 16(4), 2646-2652.

[29] Shi, J., Stratton, Z., Lin, S. C. S., Huang, H., & Huang, T. J. (2010). Tunable optofluidic microlens through active pressure control of an air–liquid interface. Microfluidics and Nanofluidics, 9(2-3), 313-318.

[30] Mao, X., Waldeisen, J. R., Juluri, B. K., & Huang, T. J. (2007). Hydrodynamically tunable optofluidic cylindrical microlens. Lab on a Chip, 7(10), 1303-1308.

[31] Mao, X., Lin, S. C. S., Lapsley, M. I., Shi, J., Juluri, B. K., & Huang, T. J. (2009). Tunable Liquid Gradient Refractive Index (L-GRIN) lens with two degrees of freedom. Lab on a Chip, 9(14), 2050-2058.

[32] Agarwal, M., Gunasekaran, R. A., Coane, P., & Varahramyan, K. (2004). Polymer-based variable focal length microlens system. Journal of Micromechanics and Microengineering, 14(12), 1665.

[33] Ren, H., Fox, D., Anderson, P. A., Wu, B., & Wu, S. T. (2006). Tunable-

focus liquid lens controlled using a servo motor. Optics express, 14(18), 8031-8036.

[34] Cheng, C. C., & Yeh, J. A. (2007). Dielectrically actuated liquid lens. Optics Express, 15(12), 7140-7145.

[35] Cheng, C. C., Chang, C. A., & Yeh, J. A. (2006). Variable focus dielectric liquid droplet lens. Optics Express, 14(9), 4101-4106.

[36] Xu, S., Ren, H., & Wu, S. T. (2013). Dielectrophoretically tunable optofluidic devices. Journal of Physics D: Applied Physics, 46(48), 483001.

[37] Wee, D., Hwang, S. H., Song, Y. S., & Youn, J. R. (2016). Tunable optofluidic birefringent lens. Soft matter, 12(17), 3868-3876.

[38] Shi, Y., Zhu, X. Q., Liang, L., & Yang, Y. (2016). Tunable focusing properties using optofluidic Fresnel zone plates. Lab on a Chip, 16(23), 4554-4559.

[39] Fang, C., Dai, B., Xu, Q., Zhuo, R., Wang, Q., Wang, X., & Zhang, D. (2017). Hydrodynamically reconfigurable optofluidic microlens with continuous shape tuning from biconvex to biconcave. Optics Express, 25(2), 888-897.

[40] Dong, L., & Jiang, H. (2008). Selective formation and removal of liquid microlenses at predetermined locations within microfluidics through pneumatic control. Journal of Microelectromechanical Systems, 17(2), 381-392.

[41] Hsiung, S. K., Lee, C. H., & Lee, G. B. (2008). Microcapillary electrophoresis chips utilizing controllable micro-lens structures and buried

optical fibers for on-line optical detection. Electrophoresis, 29(9), 1866-1873.

[42] Seow, Y. C., Liu, A. Q., Chin, L. K., Li, X. C., Huang, H. J., Cheng, T. H., & Zhou, X. Q. (2008). Different curvatures of tunable liquid microlens via the control of laminar flow rate. Applied Physics Letters, 93(8), 084101.

[43] Song, C., Nguyen, N. T., Tan, S. H., & Asundi, A. K. (2009). Modelling and optimization of micro optofluidic lenses. Lab on a Chip, 9(9), 1178-1184.

[44] Li, H., Song, C., Luong, T. D., Nguyen, N. T., & Wong, T. N. (2012). An electrokinetically tunable optofluidic bi-concave lens. Lab on a Chip, 12(19), 3680-3687.

[45] Chao, K. S., Lin, M. S., & Yang, R. J. (2013). An in-plane optofluidic microchip for focal point control. Lab on a Chip, 13(19), 3886-3892.

[46] Seow, Y. C., Lim, S. P., & Lee, H. P. (2012). Optofluidic variable-focus lenses for light manipulation. Lab on a Chip, 12(19), 3810-3815.

[47] Yang, Y., Chin, L. K., Tsai, J. M., Tsai, D. P., Zheludev, N. I., & Liu, A. Q. (2012). Transformation optofluidics for large-angle light bending and tuning. Lab on a Chip, 12(19), 3785-3790.

[48] Chiu, C. P., Chiang, T. J., Chen, J. K., Chang, F. C., Ko, F. H., Chu, C. W., ... & Fan, S. K. (2012). Liquid lenses and driving mechanisms: a review. Journal of Adhesion Science and Technology, 26(12-17), 1773-1788.

[49] Shi, Y., Liang, L., Zhu, X. Q., Zhang, X. M., & Yang, Y. (2015). Tunable self-imaging effect using hybrid optofluidic waveguides. Lab on a Chip, 15(23), 4398-4403.

[50] Liu, H. L., Zhu, X. Q., Liang, L., Zhang, X. M., & Yang, Y. (2017). Tunable transformation optical waveguide bends in liquid. Optica, 4(8), 839-846.

[51] Zhao, H. T., Yang, Y., Chin, L. K., Chen, H. F., Zhu, W. M., Zhang, J. B., ... & Ser, W. (2016). Optofluidic lens with low spherical and low field curvature aberrations. Lab on a Chip, 16(9), 1617-1624.

[52] Wolfe, D. B., Vezenov, D. V., Mayers, B. T., Whitesides, G. M., Conroy, R. S., & Prentiss, M. G. (2005). Diffusion-controlled optical elements for optofluidics. Applied physics letters, 87(18), 181105.

[53] Lin, H. C., Chen, M. S., & Lin, Y. H. (2011). A review of electrically tunable focusing liquid crystal lenses. Transactions on Electrical and Electronic Materials, 12(6), 234-240.

[54] Shi, Y. Z., Xiong, S., Chin, L. K., Yang, Y., Zhang, J. B., Ser, W., ... & Liedberg, B. (2017). High-resolution and multi-range particle separation by microscopic vibration in an optofluidic chip. Lab on a Chip, 17(14), 2443-2450.

[55] Shi, Y., Xiong, S., Chin, L. K., Zhang, J., Ser, W., Wu, J., ... & Yap, P. H. (2018). Nanometer-precision linear sorting with synchronized optofluidic dual barriers. Science advances, 4(1), eaao0773.

[56] Zhang, Y., Watts, B. R., Guo, T., Zhang, Z., Xu, C., & Fang, Q. (2016). Optofluidic device based microflow cytometers for particle/cell detection: a review. Micromachines, 7(4), 70.

[57] Watts, B. R., Zhang, Z., Xu, C. Q., Cao, X., & Lin, M. (2014). Scattering

detection using a photonic-microfluidic integrated device with on-chip collection capabilities. Electrophoresis, 35(2-3), 271-281.

[58] Godin, J., Lien, V., & Lo, Y. H. (2006). Demonstration of two-dimensional fluidic lens for integration into microfluidic flow cytometers. Applied Physics Letters, 89(6), 061106.

[59] Song, C., Luong, T. D., Kong, T. F., Nguyen, N. T., & Asundi, A. K. (2011). Disposable flow cytometer with high efficiency in particle counting and sizing using an optofluidic lens. Optics letters, 36(5), 657-659.

[60] Yang, H., & Gijs, M. A. (2018). Micro-optics for microfluidic analytical applications. Chemical Society Reviews, 47(1), 1391-1458.

[61] Lee, H. S., & Yoon, J. B. (2005). A simple and effective lift-off with positive photoresist. Journal of Micromechanics and Microengineering, 15(11), 2136.

[62] Guillén, C., & Herrero, J. (2006). Influence of oxygen in the deposition and annealing atmosphere on the characteristics of ITO thin films prepared by sputtering at room temperature. Vacuum, 80(6), 615-620.

[63] Arayanarakool, R., Le Gac, S., & van den Berg, A. (2010). Low-temperature, simple and fast integration technique of microfluidic chips by using a UV-curable adhesive. Lab on a Chip, 10(16), 2115-2121.

[64] Wägli, P., Guélat, B. Y., Homsy, A., & De Rooij, N. F. (2010). Microfluidic devices made of UV-curable glue (NOA81) for fluorescence detection based applications. In Proc. Micro Total Analysis Systems, 1937-1939.

[65] Bartolo, D., Degré, G., Nghe, P., & Studer, V. (2008). Microfluidic stickers.

Lab on a Chip, 8(2), 274-279.

[66] Dupont, E. P., Luisier, R., & Gijs, M. A. (2010). NOA 63 as a UV-curable material for fabrication of microfluidic channels with native hydrophilicity. Microelectronic engineering, 87(5-8), 1253-1255.

[67] Satyanarayana, S., Karnik, R. N., & Majumdar, A. (2005). Stamp-and-stick room-temperature bonding technique for microdevices. Journal of Microelectromechanical Systems, 14(2), 392-399.

[68] Erickson, D., Sinton, D., & Psaltis, D. (2011). Optofluidics for energy applications. Nature Photonics, 5(10), 583.

[69] Tang, S. K., Stan, C. A., & Whitesides, G. M. (2008). Dynamically reconfigurable liquid-core liquid-cladding lens in a microfluidic channel. Lab on a Chip, 8(3), 395-401.

[70] Sheldon, S. J., Knight, L. V., & Thorne, J. M. (1982). Laser-induced thermal lens effect: a new theoretical model. Applied optics, 21(9), 1663-1669.

[71] Ross, D., Gaitan, M., & Locascio, L. E. (2001). Temperature measurement in microfluidic systems using a temperature-dependent fluorescent dye. Analytical chemistry, 73(17), 4117-4123.

[72] Su, H., & Huang, X. G. (2007). Fresnel-reflection-based fiber sensor for on-line measurement of solute concentration in solutions. Sensors and Actuators B: Chemical, 126(2), 579-582.

[73] Jiang, H. R., & Sano, M. (2007). Stretching single molecular DNA by temperature gradient. Applied Physics Letters, 91(15), 154104.

[74] Snook, R. D., & Lowe, R. D. (1995). Thermal lens spectrometry. A review. Analyst, 120(8), 2051-2068.

[75] Ren, H., Xianyu, H., Xu, S., & Wu, S. T. (2008). Adaptive dielectric liquid lens. Optics express, 16(19), 14954-14960..

[76] Fan, S. K., Lee, H. P., Chien, C. C., Lu, Y. W., Chiu, Y., & Lin, F. Y. (2016). Reconfigurable liquid-core/liquid-cladding optical waveguides with dielectrophoresis-driven virtual microchannels on an electromicrofluidic platform. Lab on a Chip, 16(5), 847-854.

[77] Lin, Y. J., Chen, K. M., & Wu, S. T. (2009). Broadband and polarization-independent beam steering using dielectrophoresis-tilted prism. Optics express, 17(10), 8651-8656.

[78] Brown, C. V., Wells, G. G., Newton, M. I., & McHale, G. (2009). Voltage-programmable liquid optical interface. Nature Photonics, 3(7), 403.

[79] Jones, T. B. (2001). Liquid dielectrophoresis on the microscale. Journal of Electrostatics, 51-52(5), 290-299.

[80] Fan, S. K., Hsieh, T. H., & Lin, D. Y. (2009). General digital microfluidic platform manipulating dielectric and conductive droplets by dielectrophoresis and electrowetting. Lab on a Chip, 9(9), 1236-1242.

[81] Krogmann, F., Monch, W., & Zappe, H. (2008). Electrowetting for tunable microoptics. Journal of Microelectromechanical Systems, 17(6), 1501-1512.

[82] Hu, L., Wu, M., Chen, W., Xie, H., & Fu, X. (2017). Discontinuous pinning effect by a hole row to the gas-liquid interface in a parallel gap. Experimental

Thermal and Fluid Science, 87(10), 50-59.

[83] Mishra, K., Murade, C., Carreel, B., Roghair, I., Oh, J. M., Manukyan, G., ... & Mugele, F. (2014). Optofluidic lens with tunable focal length and asphericity. Scientific reports, 4(6378), 1-4.